אוניברסיטת תל – אביב

הפקולטה למדעים מדויקים

ע"ש ריימונד ובברלי סאקלר

המרות תדר אדיאבטיות יעילות לפולסים אולטרה-קצרים

חיבור זה הוגש כחלק מהדרישות לקבלת התואר

"מוסמך אוניברסיטה" - M.Sc. באוניברסיטת תל - אביב

ביה"ס לפיזיקה, החוג לחומר מעובה

על ידי

אסף דהן

מרץ 2018

העבודה הוכנה בהדרכתו של ד"ר חיים סוכובסקי

Tel Aviv University
Raymond & Beverly Sackler
Faculty of Exact Sciences

Efficient adiabatic frequency conversions for ultrashort

pulses

In partial fulfillment to the requirements for the degree of

Master of Science at Tel Aviv University

School of Physics & Astronomy,

Department of Condensed Matter Physics

By

Asaf Dahan

March 2018

Under the supervision of Dr. Haim Suchowski

Efficient adiabatic frequency conversions for ultrashort pulses

By

Asaf Dahan

Submitted to the department of Condensed Matter physics, School of Physics & Astronomy,

in partial fulfillment of the requirements for the degree of Master of Science in Physics

Abstract

Sensing ultrafast phenomena's demands ultrafast sources in diverse spectral regimes. Such inherently broadband source can among others be generated using frequency conversion of an ultrafast pulse. In this thesis, we developed a framework for nonlinear optical generation of ultrashort pulses through adiabatic frequency conversions evolution, incorporating both numerical evaluations and experimental validations. These include generalization of the frequency conversion process to the ultrashort regime, developing the numerical simulation for the nonlinear processes, and obtaining a robust general scheme for the design of adiabatic varying phase mismatch crystals also applicable to high-order QPM techniques. With the latter we design and investigate a novel SHG crystal with unmatched robustness under both environmental conditions and characteristics of the incoming pulse, demonstrate pulse shaping using spectral phase manipulations done before the nonlinear crystal, and obtain a design of an efficient robust optical scheme for a DFG pulse compression, with the incorporation of two photon absorption, a parasitic effect that has been lacking in all previous research on adiabatic frequency conversion, and which was found to be of great importance. Finally, we present the concept of adiabatic Four Wave Mixing frequency conversion. We present a general propagation equation for four-wave mixing derived from Maxwell's equations, capturing the full frequency and time domain nonlinear pulse propagation effects for wave-guided interactions. Last, we present that the obtained equations can be simplified to reveal the SU(2) symmetry in FWM, which leads to an analogy with rapid adiabatic passage in other two-level atomic systems.

Contents

1. Introduction

Frequency generation processes has been a subject for a vast research in the field of nonlinear optics. The ability to alter the frequency of an input electromagnetic irradiance has been in the focus of diverse research areas since the first demonstration of frequency doubling right after introducing the laser [1]. It revolutionized the field of light matter interaction, allowing new ways for exploring atomic, molecular and condensed matter systems. Among those research areas one can name nonlinear spectroscopy, metallurgy, photoinduced dynamics, condensed matter dynamics, noninvasive background free diagnostics, and the generation of new color sources [2] [3] [4] [5].

It is, however, generally difficult to obtain efficient and robust frequency conversion from a pump pulse to its harmonics for a broad range of colors in a single nonlinear crystal. This is mainly due the lack of phase mismatch (lack of momentum conservation) between the interacting waves, which conventionally can be compensated only for a narrow band of frequencies. Though, in the past, several methods were suggested to deal with the conversion of a broadband source, such as short birefringent crystals, multi-periodic modulation, chirp patterns [6] [7] [8] [9], temperature gradient manipulations [10] [11] or random oriented crystal [12]. Those indeed achieved very broadband conversion, but at the expense of limited conversion efficiencies.

In recent years, a new direction in frequency conversion has emerged - adiabatic frequency conversion - a method that is based on adiabatic evolution of the nonlinear optics dynamics. The suggested method enables to overcome the tradeoff between conversion efficiency and bandwidth [13] [14]. Though it was first considered theoretically for SHG by Baranova [15], the initial extensive experimental research was performed in sum/difference frequency conversion (SFG/DFG) in the undepleted pump approximation, offering the use of SU(2) dynamical symmetry with the analogous mechanism of Landau- Zener transition [16].

In the past few years, the fully nonlinear regime received a special attention. Research on adiabatic interactions with nonlinear dynamics as adiabatic OPA and OPO was conducted by Phillips et al. [17] [18], Heese et al. [19] [20] [21] and Yaacobi [22]. In parallel, adiabatic DFG allowed an efficient conversion of near-IR few cycle pulses to an octave-spanning mid-IR pulses [23] [24].

A general, physical model of adiabatic frequency conversion in the fully nonlinear dynamics regime, was presented recently by Porat and Arie [25], later validated by Leshem et. al. [26] for the case of adiabatic SHG in the nano-second regime.

The adiabacity condition obtained in Ref. [25] is suitable for the CW regime or to a narrow-band pulses and cannot be used when analyzing ultrashort pulses with bandwidth not negligible compared to their central frequency. Yet, adiabatic evolution theory for ultra-short pulses is still absent, thus further research as well as numerical simulations are required.

In my master work, we develop the equations dictating nonlinear frequency conversion of any Three Waves Mixing (TWM) interactions in the ultrashort regime, suitable to wideband pulses where the pulse spectral width (FWHM) is not negligible compared to the pulse central frequency. It is later demonstrated, in section (3.2.1) that the obtained set of equations is a generalization of a recently published Eq. set [27], suitable to narrowband pulses. In section (3.5) it is presented, that the equations obtained fulfill the conservation of energy.

We develop the simulation procedure for the obtained set of equations in two manners: time domain manner (section 3.2), and spectral domain manner (section 3.1). Comparison between the obtained simulations performance demonstrated the supremacy of the time domain method in simulating the ultrafast nonlinear frequency generation process of broadband TWM interactions (section 3.4).

A robust general scheme for the design of adiabatic varying phase mismatch crystals was develop for any TWM interactions, with the simulation presented herein used in an iterative manner (section 4.1). When manufacturing limitations impose a limit on the maximal phase to be provided by the crystal, we modify the obtained design using high order quasi phase matching (QPM) method. The modification used in the case of high order QPM designs is presented in section (4.2), and simulation results demonstrate the supremacy of the adiabatic crystals over periodically poled crystals in terms of sensitivity to the QPM order.

It was exhibited in the research presented in section (5) that two photon absorption (TPA), an aspect that has been lacking in all previous research on adiabatic frequency conversion, plays a significant rule in the nonlinear dynamics, also highlighting the ease in which parasitic effects can be incorporated into the simulation.

The ultrafast frequency generation simulation therefore fully enable us to extend the continually expanding vast research on adiabatic frequency conversions: we used the simulation developed herein to design a novel SHG crystal, and experimentally investigated its performance under variation of the incoming pulse energy, pulse spectral and temporal width, and under temperature variation. High conversion efficiencies and great robustness of the adiabatic SHG design were both numerically predicted and experimentally validated in section (5). The broadband operation of the adiabatic SHG

crystal presented in section ([5](#)) enables to efficiently double broadband pulses, thus allowing us to shape and control the generated SHG pulse using phase manipulations done before the nonlinear crystal. By assigning a spectral phase of absolute value and π - step to the incoming pump pulse, we achieved a wavelength tunable intense pump-probe and amplitude modulation of the broadband SHG output. The experiment details and the comparison between the experimental results to the numerical evaluations is presented in section ([6](#)). Furthermore, we used the simulation to design an efficient robust optical scheme for DFG pulse compression (section [7](#)).

Finally, we present the concept of adiabatic Four Wave Mixing (FWM) frequency conversion. As adiabatic TWM was found to be advantageous over traditional frequency conversions, it is expected that FWM frequency conversion may also benefit from the adiabatic evolution. First, we present a general propagation equation for four-wave mixing derived from Maxwell's equations, capturing the full frequency and time domain nonlinear pulse propagation effects for wave-guided interactions (section [8.1](#)). Last, we present that the obtained equations can be simplified in several conditions to reveal the SU(2) symmetry in FWM, which leads to an analogy with rapid adiabatic passage in two-level atomic systems (section [8.2](#)).

Such achievement can be useful in the design of extremely stable frequency conversion optical elements, aimed to perform at harsh environmental conditions as adverse temperatures, shocks, tensile stress and external pressure, as well in fundamental research in imaging microscopy and plasmonic nanostructures. Thus, appealing for a wide range of applications in medical procedures, avionics, satellites, and field-deployable communications systems.

2. Theoretical background – Frequency conversions

When electromagnetic waves propagate through matter, the matter polarizes, as electromagnetic force exerted on the matter charged particles generates a dipole moment.
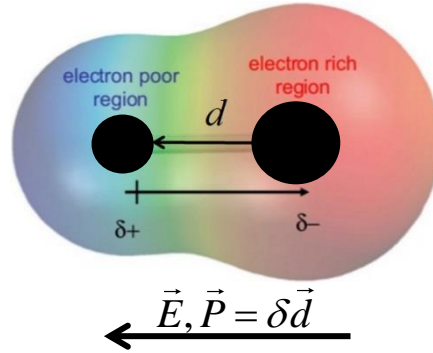
Figure 1. Schematic presentation of the generated dipole moment. The electric field acts on the molecule electrons cloud, creating an electron density gradient resulting is an electric dipole. d is the separation between the poor and rich electron regimes, and δ is the regime charge.

The oscillating electromagnetic field generates an oscillating polarization radiating itself. The total generated electromagnetic field is governed by Maxwell equations [28]:

$$(2.1)\, \nabla \times \vec{E} = -\mu \frac{\partial \vec{H}}{\partial t}$$

$$(2.2)\, \nabla \times \vec{H} = \varepsilon_0 \frac{\partial \vec{E}}{\partial t} + \frac{\partial \vec{P}}{\partial t}$$

A simple model for the generated polarization is the Lorentz model, where the interaction between the electron poor and rich regimes is assumed to be harmonic:

$$(2.3)\, U_{\text{int}}(d) = \frac{1}{2}kd^2$$

where d is the displacement between the poor and rich electron regimes, and k comes from the Coulombic interaction between the two. In that case, the force exerted on the molecule $\vec{F} = \delta \vec{E}$, is proportional to the displacement d via Hooke-law $F = kd$. As the generated polarization $\vec{p} = \delta \vec{d}$ is proportional to $\vec{d}$, the generated polarization is linear to the electric field, hence denoted $\vec{P}_{Linear}$:

$$(2.4)\, \vec{P}_{Linear} = \varepsilon_0 \chi_1 \vec{E}$$

where ε_0 is the vacuum permittivity [F/m] and χ_1 is the electric field first order susceptibility. As the obtained polarization will oscillate in the same frequency as the incident field, insertion of $\vec{P}_{Linear}$ into equations (2.1)-(2.2) results in total electromagnetic field with the same frequencies as the incident field.
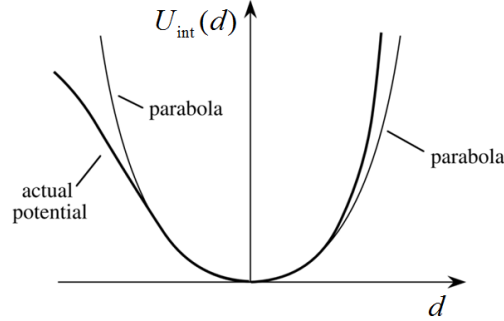
Figure 2. Nonlinear polarization terms roots in the an-harmonic behavior of the interaction hamiltonian.

Deviation between the actual interaction potential to a harmonic potential will result in polarization terms, denoted $\vec{P}_{Non\,linear}$ that are not proportional to the incident electric field. The polarization, as a general function of the electric field, can be therefore expressed in terms of its powers:

$$(2.5)\ P = \varepsilon_0\chi_1 E + \underbrace{\varepsilon_0\chi_2 E^2 + \varepsilon_0\chi_3 E^3 + \cdots}_{P_{Non\,linear}}$$
$$\underbrace{}_{P_{Linear}}$$

where χ_j is the j-order electrical susceptibility $\left[\dfrac{m}{V}\right]^{j-1}$. New frequencies are generated by the nonlinear polarization terms, as multiplication of periodic functions changes their periodicity. Up to third order nonlinear electrical susceptibility, the insertion of frequencies ω_1, ω_2, as an example, may results (depends on the material electrical susceptibilities characteristics) in the generation of the following frequencies terms, differ in the polarization term responsible to them.

Polarization term	Generated frequencies
Linear term - first order susceptibility χ_1	ω_1, ω_2
Second order susceptibility χ_2	$2\omega_1, 2\omega_2, \omega_1+\omega_2, \lvert\omega_1-\omega_2\rvert$
Third order susceptibility χ_3	$3\omega_1, 3\omega_2, 2\omega_1+\omega_2, \omega_1+2\omega_2, \lvert 2\omega_1-\omega_2\rvert, \lvert 2\omega_2-\omega_1\rvert$

The generation of third frequency $\omega_3 = \omega_1 + \omega_2$ through second order electrical susceptibility χ_2 between ω_1 and ω_2, results in the following set of coupled equations [28]:

$$(2.6)\ \frac{dA_1(z)}{dz} = i\frac{\chi_2\omega_1^2}{k_1 c^2}A_3(z)A_2^*(z)e^{-i\Delta k \cdot z}$$

$$\frac{dA_2(z)}{dz} = i\frac{\chi_2\omega_2^2}{k_2 c^2}A_3(z)A_1^*(z)e^{-i\Delta k \cdot z}$$

$$\frac{dA_3(z)}{dz} = i\frac{\chi_2\omega_3^2}{k_3 c^2}A_1(z)A_2(z)e^{i\Delta k \cdot z}$$

where the electric field is given by $E(z,t) = \frac{1}{2}\sum_{j=1}^{3}A_j(z)e^{i(\omega_j t - k_j z)} + c.c,$ k_j is the electric field wave

number, given by $k_j = \frac{\omega_j}{c}n(\omega_j)$ and $\Delta k = (k_3 - k_2 - k_1)$ is the phase mismatch between the

interacting waves. The generation of third frequency through TWM can be done in three schemes:
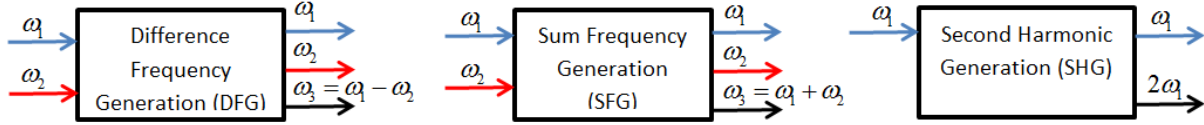
Figure 3. TWM schemes: DFG, SFG and SHG configurations

2.1 SHG Scheme

The equations dictating SHG are [28]:

$$(2.7)\ \frac{dA_\omega(z)}{dz} = i\frac{\chi_2\omega}{n_\omega c}A_{2\omega}(z)A_\omega^*(z)e^{-i\Delta k \cdot z}$$

$$\frac{dA_{2\omega}(z)}{dz} = i\frac{\chi_2\omega}{n_{2\omega}c}A_\omega^2(z)e^{-i\Delta k \cdot z}$$

In the undepleted pump approximation, we assume that the pump intensity merely changes due to the interaction between its second harmonic. In that case, the process conversion efficiency can be easily deduced:

$$(2.8)\ I_{2\omega}(z) = \frac{2\chi_2^2\omega^2\eta_0}{n_{2\omega}n_\omega^2 c^2}I_\omega^2 z^2 \, \mathrm{sinc}^2\left(\frac{\Delta k}{2}z\right)$$

11
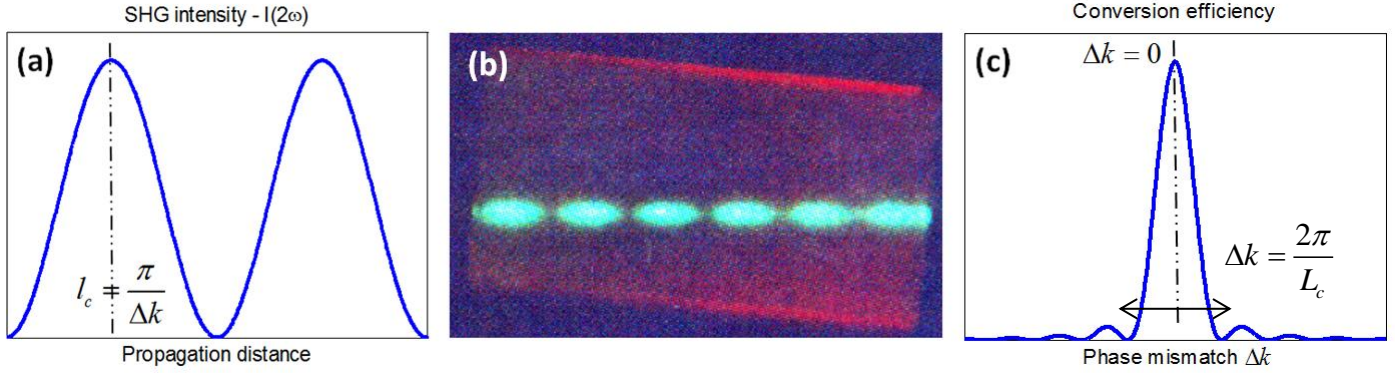
Figure 4. SHG dependence with the optical axis and the phase mismatch. (a) Second Harmonic dependence with the optical axis. Conversion and back-conversion of the second harmonic is observed. (b) Experimental demonstration of inset a. (c) Conversion efficiency dependence with phase mismatch. Two sided main lobe width is given by $\Delta k = 2\pi / L_c$ **, where** L_c **is the crystal length.**

It is presented that the second harmonic intensity constructively interferes up to a coherence length denoted $l_c = \dfrac{\pi}{\Delta k}$, afterwards destructively interferes up to $2l_c$ and vice-versa. The phase mismatch Δk therefore imposes a limit on the generated second harmonic, as longer crystals do not exhibit better conversion efficiencies. In Fig. 4 inset (c) it is presented that the conversion process impose a tradeoff between the conversion efficiency and the phase mismatch of the interacting waves. For example, a 2mm standard BBO type I crystal designed to double 800nm, has a main lobe 2 sided width equivalent to deviation of 3nm from each side of its operational wavelength: 797nm-803nm. For further impression, we present the conversion efficiency dependence with wavelength and temperature of 1mm periodically poled SLT crystal, designated to double 800nm:
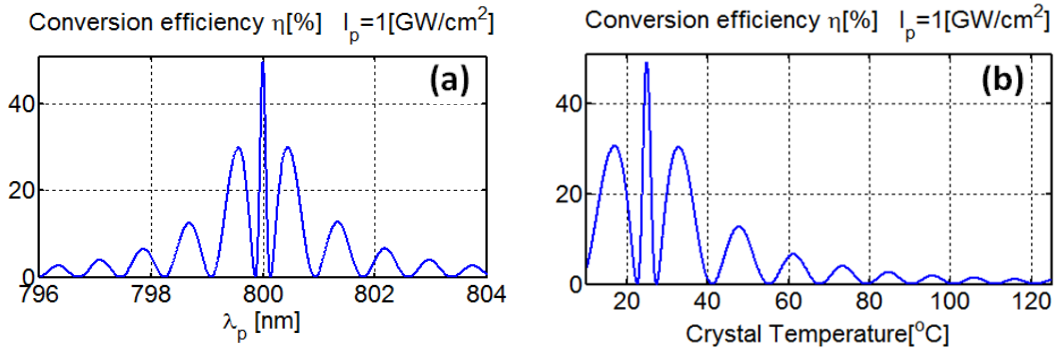
Figure 5. Periodically poled SLT conversion efficiency sensitivity. (a) Conversion efficiency dependence with wavelength. (b) Conversion efficiency dependence with temperature.

The operational wavelength FWHM is $\Delta\lambda = 0.1nm$ and the operational temperature FWHM is $\Delta T = 2[^oC]$. It is possible to work around the second lobe of the presented design (centered around 800.3nm) with increased robustness in wavelength and temperature, but at the expense of lower conversion efficiency. It is seen that conversion efficiency for such simple designs is not robust to large

deviation in wavelength nor in temperature, and the tradeoff between high conversion efficiency and robustness is observed.

2.2 DFG/SFG Schemes

We investigate the generation of third frequency ω_3 through DFG between ω_1 and ω_2 in the un-depleted pump approximation, where the intensity of ω_2 merely changes due to the interaction between the waves, i.e $I(\omega_2) \gg I(\omega_1), I(\omega_3)$. The undepleted amplitude A_2 is termed pump, and the amplitudes A_1, A_3 are termed signal and idler respectively. The following set of equations is obtained:

$$(2.9) \quad \frac{dA_1(z)}{dz} = i \frac{\chi_2 \omega_1}{n_1 c} A^*_2 A_3(z) e^{-i\Delta k \cdot z}$$

$$\frac{dA_3(z)}{dz} = i \frac{\chi_2 \omega_3}{n_3 c} A_2 A_1(z) e^{i\Delta k \cdot z}$$

The solution for the above set of equations for constant nonlinear electrical second order susceptibility, where the initial conditions are $I_1(z = 0) = I_1(0)$ and $I_3(z = 0) = 0$ is given by:

$$(2.10) \quad I_1(z) = I_1(0) \frac{\left(\kappa^2 \cos^2\left(\frac{\sqrt{\kappa^2 + \Delta k^2}}{2} z \right) + \Delta k^2 \right)}{\kappa^2 + \Delta k^2}, \quad I_3(z) = I_1(0) \frac{\omega_3}{\omega_1} \frac{\left(\kappa^2 \sin^2\left(\frac{\sqrt{\kappa^2 + \Delta k^2}}{2} z \right) \right)}{\kappa^2 + \Delta k^2}$$

where $\kappa = \frac{2\chi_2 \sqrt{k_1 k_3}}{n_1 n_3} A_2 \, [m^{-1}]$ is the coupling coefficient and n is the material refractive index. We see that in the presence of constant phase mismatch Δk between the interacting waves, conversion and back conversion of the generated idler occurs.
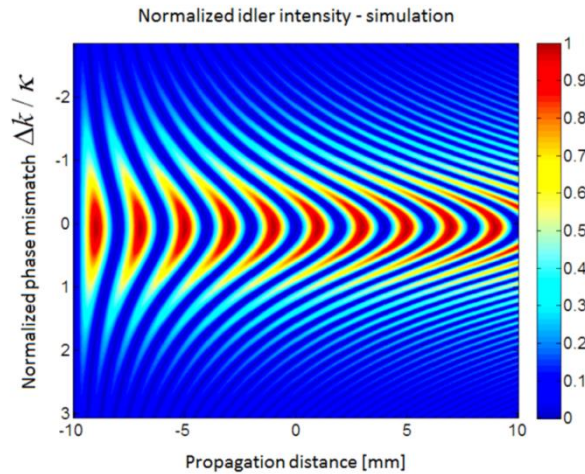
Figure 6. Normalized idler intensity as function of the propagation distance for various phase mismatches. It is demonstrated that conversion efficiency is decreased in a sinc-wise manner, having its maximal value for $\Delta k = 0$.

The same tradeoff between conversion efficiency and phase mismatch discussed in section ([2.1](#)) for the SHG scheme also exist here, as conversion efficiency descends with ascending $|\Delta k|$, hence sensitive to small variations in the idler/signal wavelengths, as well as variations in environmental conditions as temperature. Using Eq. set (2.9), one can deduce that in the undepleted pump regime, the photon flux of both the idler and the signal waves remain constant:

$$(2.11) \quad \frac{dN_1}{dz} + \frac{dN_3}{dz} = 0$$

where $N_1 = \dfrac{I_1(z)}{\hbar \omega_1}$ and $N_3 = \dfrac{I_3(z)}{\hbar \omega_3}$. The above equation, also known as the **photon number conversion rule**, **or Manley-Rowe relations** [28] implies that the annihilation of photon (resp. creation) at ω_3 is automatically associated with the creation (resp. annihilation) of one photon at ω_1. It is therefore informative to define the frequency generation conversion efficiency to be the ratio between the photon flux of the generated idler and the incoming signal photon flux:

$$(2.12) \quad \eta(z) = \frac{N_3(z)}{N_1(z_{in})}$$

which implies that the conversion efficiency in the undepleted pump regime is given by:

$$(2.13) \quad \eta(z) = \frac{\sin^2\left(\dfrac{\sqrt{\kappa^2 + \Delta k^2}}{2} z \right)}{\left(1 + \left(\dfrac{\Delta k}{\kappa} \right)^2 \right)}$$

2.3 Phase Matching

In the absence of phase mismatch mechanism, significant generation of high-order harmonics is lacking, as waves generated at locations distanced by l_c destructively interfere. Phase matching techniques are therefore critical when high conversion efficiency is desired, all designated to maintain the energy flow direction towards the high order harmonics. Several methods exist in order to effectively diminish the phase mismatch between the interacting waves, such as type I and type II phase compensation in birefringent crystals and QPM techniques. Using birefringent crystals, the phase mismatch can be zeroed if the waves polarization relative to the crystal primary axes are carefully chosen. In the case of phase matching type I, the phase mismatch for SHG process

$$\Delta k = 2k(\omega) - k(2\omega) = \frac{2\omega}{c}\big(n(\omega) - n(2\omega)\big), \text{can} \qquad \text{be}$$

diminished using different polarizations for the pump and its second harmonic. As the k-vector projection on the extra-ordinary defines the extraordinary index of refraction according to the index ellipsoid $n_e^{-2}(\theta) = \cos^2(\theta)n_0^{-2} + \sin^2(\theta)n_e^{-2}$, θ can be chosen such that $n_e^{2\omega}(\theta) = n_o^{\omega}$ for negative uniaxial crystal, and $n_e^{\omega}(\theta) = n_o^{2\omega}$ for a positive uniaxial crystal. In the case of phase matching type II, the pump electric field contains both the ordinary and extraordinary polarizations, changing the required cutting angle θ such that $k_e^{2\omega}(\theta) = k_o^{\omega} + k_e^{\omega}(\theta)$.

The problem with the presented methods is that the photon flux of the extraordinary polarization differs from its k-vector, therefore creating a spatial walk-off between the ordinary and the extraordinary beams, hence limiting the maximal possible conversion efficiency.

Figure 7. The k-vector direction projection on the primary axis defines the propagation refractive indexes.

Another method is the QPM method, where in a process known as poling [28], strong electric field applied on ferroelectric crystal allows the modification of the nonlinear electrical susceptibility sign $\pm\chi_2$, therefore enables us to design the second order susceptibility dependence with the optical axis: $\chi_2(z) = \chi_2 \, \text{sign}\big(\cos(K_g(z)z)\big)$. $K_g(z)$, the grating momenta, is the z dependent spatial frequency in which $\chi_2(z)$ fluctuates between $+\chi_2$ to $-\chi_2$. It is possible to maintain the direction of the energy flow if the sign of χ_2 flips with each domain width equal to l_c, in other words when the crystal is periodically poled with $K_g = \Delta k$. In that manner, waves generated at locations distanced by l_c are added an extra π - phase and interfere instructively. To understand how this modulation facilitates phase-matching

15

let's consider periodic modulation with period Λ: $\chi_2(z) = \chi_2 sign\left(\cos\left(\dfrac{2\pi z}{\Lambda}\right)\right)$. Expanding $\chi_2(z)$ using Fourier series results in the following:

$$(2.14) \quad \chi_2(z) = \chi_2 \sum_{m=-\infty}^{+\infty} \left(\frac{2}{m\pi}\sin\left(\frac{m\pi}{2}\right)\right)\exp\left(i\frac{2\pi m}{\Lambda}z\right)$$

Ignoring the cumulative effect of higher orders than $m = 1$, and substituting Eq. (2.14) into Eq. set (2.9) yields:

$$(2.15) \quad \frac{dA_1(z)}{dz} = i\frac{2\chi_2\omega_1^2}{\pi k_1 c^2}A_3(z)A_2^*(z)\exp\left(-i\left(\Delta k - \frac{2\pi}{\Lambda}\right)\cdot z\right)$$

$$\frac{dA_2(z)}{dz} = i\frac{2\chi_2\omega_2^2}{\pi k_2 c^2}A_3(z)A_1^*(z)\exp\left(-i\left(\Delta k - \frac{2\pi}{\Lambda}\right)\cdot z\right)$$

$$\frac{dA_3(z)}{dz} = i\frac{2\chi_2\omega_3^2}{\pi k_3 c^2}A_1(z)A_2(z)\exp\left(+i\left(\Delta k - \frac{2\pi}{\Lambda}\right)\cdot z\right)$$

As seen, the phase mismatch parameter is added the nonlinear susceptibility spatial frequencies. By choosing $K_g = \dfrac{2\pi}{\Lambda} = |\Delta k|$, it is possible to compensate the phase mismatch between the interacting waves. Designing the susceptibility modulation period Λ to zero the phase mismatch term in equations (2.15) using the first Fourier coefficient ($m = 1$) is termed QPM.
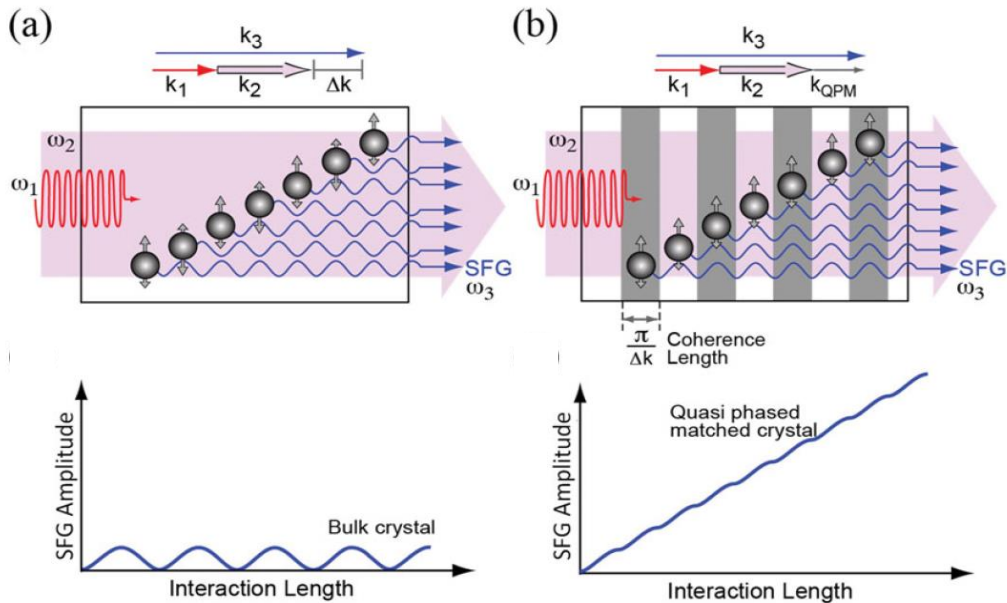
Figure 8. SFG scheme (a) Phase mismatched SFG. The generated sum frequency is converted and back-converted, as waves generated at locations distanced by coherence length destructively interfere. (b). Quasi phase matched SFG. The generated sum frequency instructively interfere all over the optical axis. Graph is taken with permission from Ref. [13].

Zeroing the phase mismatch using Fourier term of order m is called QPM of order m, namely $m\left(\dfrac{2\pi}{\Lambda}\right) = |\Delta k|$. In other words, In the case of periodic poling, the grating momenta required for QPM of order N_{QPM}, can be expressed using the first order QPM grating momenta:

$$(2.16)\ K_g^{\,N_{QPM}} = \frac{1}{N_{QPM}} K_g^{\,N_{QPM}=1}$$

which modifies in the case of arbitrary phase mismatch designs in section ([4.2](#)):

$$(2.17)\ K_g^{\,N_{QPM}}(z) = \frac{K_g^{\,N_{QPM}=1}(z)}{N_{QPM}}$$

where $K_g(z)_{L_c}^{\,N_{QPM}}$ is the QPM grating design of order N_{QPM} designated to a crystal length L_c.

2.4 Adiabatic Frequency Conversions

Following the notation $\tilde{A}_1 = \dfrac{\sqrt{k_1}}{\omega_1 A_2} A_1$, $\tilde{A}_3 = \dfrac{\sqrt{k_3}}{\omega_3 A_2} A_3$, Eq. set (2.7) becomes:

$$(2.18)\ \frac{d\tilde{A}_1}{dz} = i\frac{\kappa}{2}\tilde{A}_3 e^{-i\Delta kz}$$

$$\frac{d\tilde{A}_3}{dz} = i\frac{\kappa^*}{2}\tilde{A}_1 e^{+i\Delta kz}$$

where κ is given by $\kappa = \dfrac{2\chi_2\sqrt{k_1 k_3}}{n_1 n_3} A_2$. As noticed by Suchowski et al. [14], the above system possess a SU(2) symmetry with complete analogy to other two states systems, such as nuclear magnetic resonance (NMR), polarization optics and the interaction of coherent light with a two-level atom, given as an example:
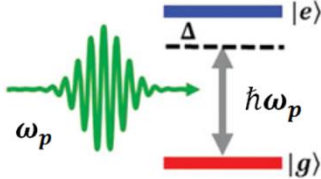
$$(2.19)\ \frac{da_g}{dt} = i\frac{\Omega_0}{2} a_e e^{-i\Delta(t-t_0)}$$

$$\frac{da_e}{dt} = i\frac{\Omega_0^*}{2} a_g e^{+i\Delta(t-t_0)}$$

Figure 9. The interaction between two level atom and coherent light. A photon centered around ω_p interacts with an atom having energy gap $\dfrac{\Delta E}{\hbar} = \left(\omega_p + \Delta\right)$. The interaction strength is determined by Rabi frequency $\Omega_0 = \dfrac{\mu\varepsilon_p}{\hbar}$, where μ is the dipole moment and ε_p is the pump electric field.

The electric field amplitudes $\tilde{A}_1, \tilde{A}_3$ are analogous to the ground and excited amplitudes a_g and a_e dictating the wave function $|\psi\rangle = a_e|e\rangle + a_g|g\rangle$. The interaction strength κ is analogous to Rabi-frequency Ω_0 and the phase mismatch Δk is proportional to the detuning Δ.

It is therefore feasible to adopt the vast research that has been conducted in the field of coherent quantum control to the field of frequency conversions, allowing us to find new ways to efficiently convert broadband sources. We define the adiabatic basis, which is the basis of the system's eigenvectors:

$$
(2.20) \quad \begin{pmatrix} B_1 \\ B_3 \end{pmatrix} = \begin{pmatrix} \cos\left(\dfrac{\theta}{2}\right) & \sin\left(\dfrac{\theta}{2}\right) \\ -\sin\left(\dfrac{\theta}{2}\right) & \cos\left(\dfrac{\theta}{2}\right) \end{pmatrix} \begin{pmatrix} C_1 \\ C_3 \end{pmatrix}
$$

where $C_1 = \tilde{A}_1 e^{i\frac{\Delta k}{2}z}, C_3 = \tilde{A}_3 e^{-i\frac{\Delta k}{2}z}$ are the unperturbed system eigenvectors. The dynamics of the adiabatic states can be derived:

$$
(2.21) \quad \frac{d}{dz}\begin{pmatrix} B_1 \\ B_3 \end{pmatrix} = \frac{1}{2}\begin{pmatrix} i\varepsilon(z) & \dot{\theta} \\ -\dot{\theta} & i\varepsilon(z) \end{pmatrix}\begin{pmatrix} B_1 \\ B_3 \end{pmatrix}
$$

where $\varepsilon(z) = \sqrt{\Delta k^2 + \kappa^2}$ and the mixing angle θ obey $\sin(\theta) = \dfrac{\kappa(z)}{\varepsilon(z)}, \cos(\theta) = \dfrac{\Delta k(z)}{\varepsilon(z)}$ and $\tan(\theta) = \dfrac{\kappa(z)}{\Delta k(z)}$. In adiabatic process, the system stays in one of its eigenvectors throughout the entire interaction. The condition for adiabatic frequency condition is therefore given by $|i\varepsilon(z)| \ll \dot{\theta}$. In the case of constant κ, the adiabatic criterion is manifested in the following form:

$$
(2.22) \quad \left|\frac{d\Delta k}{dz}\right| \ll \frac{\left(\Delta k^2 + \kappa^2\right)^{3/2}}{\kappa}
$$

The condition puts a limit on how fast the phase mismatch parameter can vary along the optical axis in order to get good conversion. It is also clear that the conversion process is more adiabatic when the pump power is increased (increasing κ). To understand how the variation of the phase mismatch parameter $\Delta k(z)$ facilitates frequency conversion, let's assume that $\dfrac{\Delta k(z_{in})}{\kappa(z_{in})} \ll 0$ and $\dfrac{\Delta k(z_{out})}{\kappa(z_{out})} \gg 0$, where z_{in}, z_{out} are the crystal input and output facets locations respectively. In that case, the mixing angle θ varies between π to 0 as the adiabatic states in Eq. (2.20) tends to different unperturbed states:

$$C_3 \xleftarrow[\theta=\pi]{z_{in}} B_1 = \cos\left(\frac{\theta}{2}\right)C_1 + \sin\left(\frac{\theta}{2}\right)C_3 \xrightarrow[\theta=0]{z_{out}} C_1$$

$$-C_1 \xleftarrow[\theta=\pi]{z_{in}} B_3 = -\sin\left(\frac{\theta}{2}\right)C_1 + \cos\left(\frac{\theta}{2}\right)C_3 \xrightarrow[\theta=0]{z_{out}} C_3$$

If the system starts in one of its eigenvectors, and the adiabatic criteria in Eq. (2.22) is fulfilled, the system stays in the same eigenvector. As the adiabatic states tends to different unperturbed states via the z-dependent mixing angle θ, the population gradually passes from C_1 to C_3 (or vice versa), and complete population transfer is feasible.
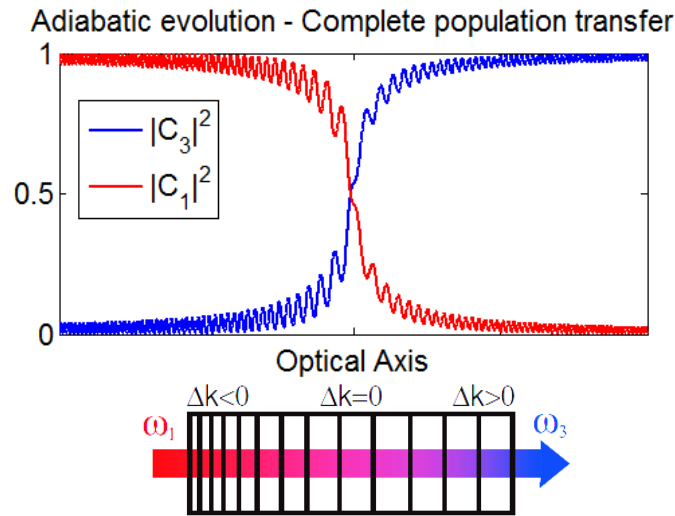
Figure 10. Adiabatic evolution. By adiabatically changing the phase mismatch parameter along the crystal optical axis, complete population transfer is feasible. In other words, complete conversion between the signal and idler photon flux, defined in Eq. (2.11).

A grating possessing a varying phase mismatch $\Delta k(z)$ is inherently broadband, as diverse TWM interactions differ in their phase mismatch can be efficiently generated at different locations on the optical axis. The broadband operation of such an adiabatic design was experimentally demonstrated in Ref. [23], where 680-870nm NIR pulse were efficiently down converted into an octave spanning $2-5\mu m$ MIR pulse using a 1047nm pump.

Figure 11. Main figure: Conversion efficiency map as a function of the generated wavelength (y-axis) and the location along the optical axis (x-axis). The pump intensity is $8.1 GW/cm^2$. The upper panel shows the conversion efficiency for several wavelengths along the propagation axis. As seen, all are designed to have adiabatic trajectories for efficient conversion from near IR to mid IR. At the output facet of the nonlinear crystal (L = 2 cm), high conversion efficiency is achieved for the 1300-5500 nm spectral range. Graph is taken with permission from Ref. [23].
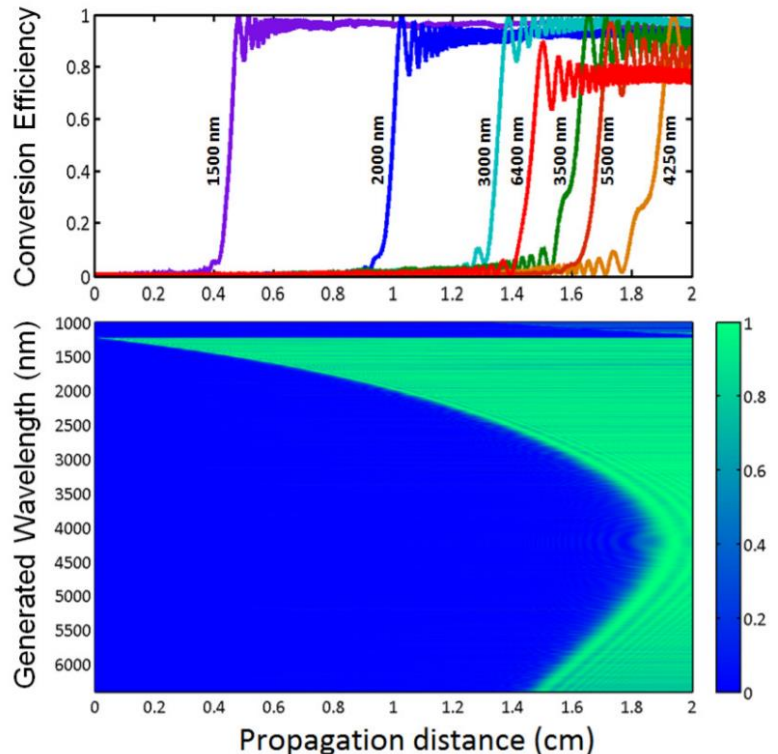
2.5 SU(2) geometrical representation – Bloch sphere

The geometrical representation used to visualize the dynamics of spin ½ system by F. Bloch [29], R. Feynman for atomic systems [30] and Poincare in polarization optics can be adopted to the field of frequency conversions. In Bloch sphere presentation, the dynamics of SFG (or alternatively DFG) dictated by Eq. set (2.18) is visualized by a unit vector $\vec{\rho}_{SFG}$ capsulated by the sphere. The state vector

$$\vec{\rho}_{SFG} = \begin{pmatrix} U_{SFG} \\ V_{SFG} \\ W_{SFG} \end{pmatrix}, \text{ given by } \vec{\rho}_{SFG} = \begin{pmatrix} C_3^*C_1 + C_1^*C_3 \\ i\left(C_3^*C_1 - C_1^*C_3\right) \\ |C_3|^2 - |C_1|^2 \end{pmatrix} \text{ obeys the precession equation:}$$

$$(2.23) \quad \frac{d\vec{\rho}_{SFG}}{dz} = \vec{g} \times \vec{\rho}_{SFG}$$
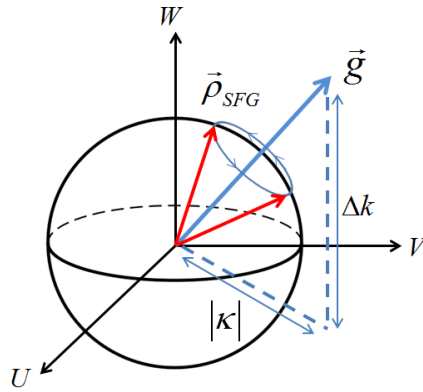
Figure 12. The precession equation. Visualization of the state vector $\vec{\rho}_{SFG}$ precession around the torque vector $\vec{g}$.

The torque vector, given by $\vec{g} = (\mathrm{Re}(\kappa), \mathrm{Im}(\kappa), \Delta k)$ determines the evolution of the nonlinear interaction. While the south pole of the sphere $\vec{\rho}_{SFG} = (0,0,-1)$ corresponds to $C_3 = 0$, i.e zero conversion, the north pole $\vec{\rho}_{SFG} = (0,0,1)$ corresponds to full conversion. An efficient conversion process will be therefore visualized by a gradually rising state vector, as conversion efficiency depends on the state trajectory on the W axis $\eta = |C_3|^2 = \frac{1+W}{2}$.

In the undepleted pump approximation where κ is constant, the SFG (or DFG) dynamics in the case of constant phase mismatch Δk are given by the precession equation with constant torque vector $\vec{g}$. The state vector trajectory is therefore a periodic circle with period $\Delta z = \frac{2\pi}{|g|} = \frac{2\pi}{\sqrt{\Delta k^2 + \kappa^2}}$, as already stated in Eq. (2.10). In the case of zero phase mismatch Δk, the torque vector lies in the UV plane, and the state vector trajectory passes through both the south and north poles. In other words, full conversion and back conversion of the generated idler occurs. When the phase mismatch is not zero, and the system starts without SFG/DFG present (that is to say in the south pole), the state vector trajectory can never pass through the north pole, and full conversion is therefore impossible. Visualization of the described trajectories is exhibited in Fig. 12.
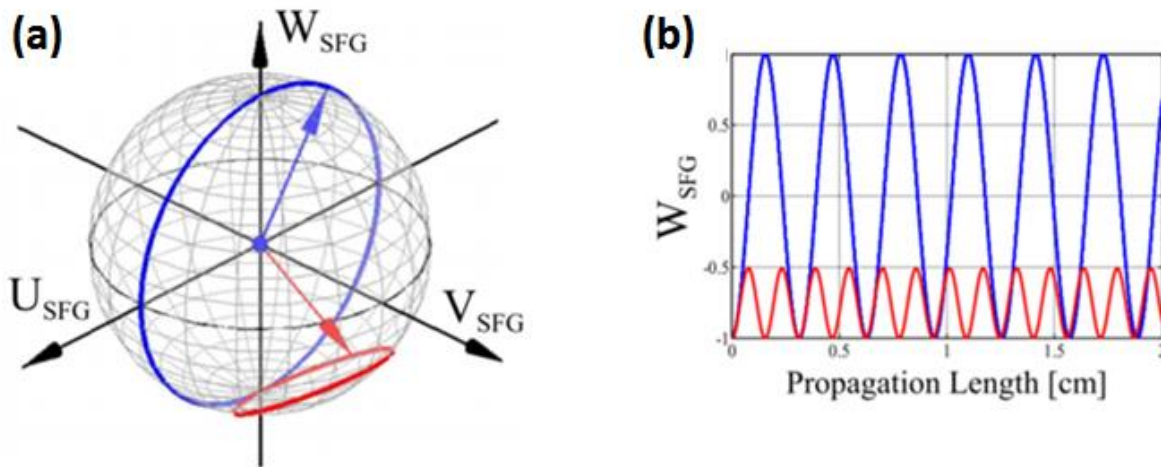
Figure 13. (a) Bloch Sphere visualization for the case of constant phase matching and constant coupling strength κ. Blue trajectory - $\Delta k = 0$. Red trajectory - $\Delta k \neq 0$. (b) State vector trajectory on the W axis. Conversion and back conversion of the generated idler is presented for the described trajectories via $\eta = \frac{1+W_{SFG}}{2}$, with accordance to Eq. (2.10). Graphs are taken with permission from Ref. [14].

The state vector trajectory is completery different in the adiabatic regime. While the phase mismatch parameter gradually changes between negative values to positive ones (as described in section 2.4), the torque vector $\vec{g}$ climbs from the south pole towards the north pole. Since the state vector trajectoy precess the torque vector $\vec{g}$, the state vector itself gradually climbs towards the north pole, and high conversion efficieny is achieved. The transition between low conversion efficienies towards high ones occurs in the regime $|\Delta k / \kappa| \ll 1$, where the precession vector $\vec{g}$ lies in the UV plane and the state vector moves from the south hemisphere to the north one.
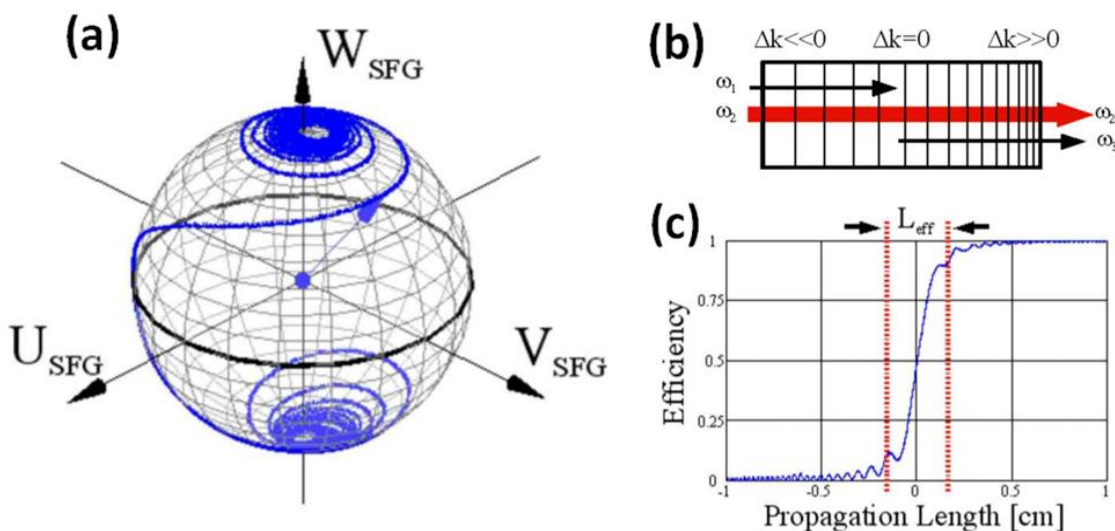
Figure 14. Bloch sphere visualization for adiabatic frequency conversion. (a) State vector trajectory in the adiabatic regime gradually climbs between the south pole (zero efficiency conversion) towards the north pole (full conversion efficiency). (b) Phase mismatch dependence with the optical axis in the adiabatic regime. (c) Conversion efficiency increases with propagation length. The transition between the southern hemisphere to the northern one effectively occurs within L_{eff}, centered around $\Delta k = 0$. Graphs are taken with permission from Ref. [14].

3. Spectral and temporal numerical simulation of TWM

Simulating the nonlinear interaction between ultrafast pulses inside the grating crystal was done in two presentations. In the first one, the common continuous wave (CW) amplitude equations describing mono-chromatic sources were generalized to deal with wideband sources. In that method, the nonlinear interactions are described in terms of the fields spectral amplitudes, while in the second method the nonlinear interactions are described using the pulses time-envelopes. In what follows it is shown that although mathematically equivalent, the time domain presentation surpasses the frequency domain presentation in terms of calculation time and ease of calculation.

3.1 Frequency domain based simulation

3.1.1 Equations derivation in the frequency domain

We present the equations of an input pulse being inserted into a media with chirped second order nonlinear susceptibility. Denoting the fields amplitudes with A_j, where j denotes the frequency ω_j, the electric field is written in the following manner:

$$(3.1)\, E = \sum_j A_j(z)\, e^{i(\omega_j t - k_j z)}\, F(x, y)\Delta f$$

where k_j is the electric field wave number, given by $k_j = \dfrac{\omega_j}{c} n(\omega_j)$, z is the optical axis of the crystal, $\Delta f = f_{j+1} - f_j$ is the simulation resolution in the frequency domain, and $F(x, y)$ is the electric field mode profile obeying Helmholtz equation:

$$(3.2)\, \nabla^2_t F(x, y) + \left(\left(\frac{\omega_j n}{c}\right)^2 - k_j^2\right) F(x, y) = 0 \ .$$

Detailed derivation of the equations dictating the frequency conversion process is presented in [appendix A](appendix).

To summarize, the equations obtained are the following:

$$(3.3)\frac{dB_I(z,f_j)}{dz} = i\frac{X_2(z)\omega_j^2}{k_j c^2} e^{+ik_j z}\left(B_S(z,f_m)e^{-jk_m z}\right) * \left(\left(B_P(z,f_k)e^{-jk_k z}\right)^*\right)\Delta f$$

$$\frac{dB_P(z,f_k)}{dz} = i\frac{X_2(z)\omega_k^2}{k_k c^2} e^{ik_k z}\left(B_S(z,f_m)e^{-ik_m z}\right)\odot\left(B_I(z,f_j)e^{-ik_j z}\right)\Delta f$$

$$\frac{dB_S(z,f_m)}{dz} = i\frac{X_2(z)\omega_m^2}{k_m c^2} e^{ik_m z}\left(B_P(z,f_k)e^{-ik_k z}\right)\odot\left(\left(B_I(z,f_j)e^{-ik_j z}\right)^*\right)\Delta f$$

with the following notations:

- $A_\alpha(z,f_j)$ - Amplitude of pulse $\alpha \in [I,P,S]$ at frequency f_j, where $\alpha \in [I,P,S]$ denotes the Idler (I), pump (P) and signal (S) pulses.
- Υ - Normalization constant defined by the electromagnetic field mode profile:

$$\Upsilon = \frac{\int|F(x,y)|^2 F(x,y)dxdy}{\int|F(x,y)|^2 dxdy}$$

- $B_\alpha = \Upsilon A_\alpha$ - Normalized pulses amplitudes.
- Δf - The spectral simulation resolution defined by $\Delta f = f_{j+1} - f_j$.
- The symbol $*$ between two arguments $f*g$ defines the discrete convolution operation:

$$(f*g)[n] = \sum_k f[k]g[n-k]$$

- The symbol $\odot$ between two arguments $f\odot g$ defines the discrete correlation operation:

$$(f\odot g)[n] = \sum_k f[k]g^*[n+k]$$

3.1.3 Simulation procedure in the frequency domain

I. Pulses definition:

In section ([10.3.2](#)) it is shown that the pulse energy density is given by:

$$(3.4)\ E_d = \frac{E_d}{A_{eff}}\left[\frac{J}{m^2}\right] = \int \frac{n(f)}{2\eta_0}\left|B(z,f)\right|^2 df$$

where η_0 is the waves impedance (377Ω) and $n(f)$ is the frequency dependent refraction index. We start by defining the spectral pulses shape and normalizing it such that Eq. (3.4) is obeyed for each of the pulses with the corresponding energy density:

$$(3.5)\ B(f)_{Normalized} = \sqrt{\frac{2\eta_0 \cdot Ed}{\sum_j n(f_j)\left|B(f_j)\right|^2 \Delta f}} B(f)$$

The pulses time duration is then determined by the pulses spectral phase. As an option, a parabolic spectral phase can be applied to broaden the pulse [28]:

$$(3.6)\ B(z_{in},f) = \exp\left(-i\frac{Chirp}{2}\left(\omega - \omega_{center}\right)^2\right)B(f)_{Normalized}$$

Where ω_{center} is the central pulse frequency and z_{in} is the crystal entrance facet position.

II. Numerical integration

Defining the pulses amplitudes $\vec{B} = \begin{pmatrix} B_S(z,f) \\ B_P(z,f) \\ B_I(z,f) \end{pmatrix}$ and the nonlinear Eq. set (3.3) by $G(\vec{B},z,f)$, the numerical integration is performed using 4'th order Runge-Kutta method in the following manner:

$$(3.7)\ \frac{\partial \vec{B}(f,z)}{\partial z} = G(\vec{B},f,z),\ \ \vec{B}(z_{in}) = \vec{B}_{in}$$
$$n = 0,1,2,3....$$
$$k_1 = G(\vec{B}_n, f, z_n)$$

$$k_2 = G\left(\vec{B}_n + \frac{h}{2}k_1, z_n + \frac{h}{2}\right)$$

$$k_3 = G\left(\vec{B}_n + \frac{h}{2}k_2, z_n + \frac{h}{2}\right)$$

$$k_4 = G\left(\vec{B}_n + hk_3, z_n + h\right)$$

$$\vec{B}_{n+1} = \vec{B}_n + \frac{h}{6}\left(k_1 + 2k_2 + 2k_3 + k_4\right) , \quad z_{n+1} = z_n + h$$

where h is the spatial resolution of the optical axis, n indexing the position on the optical axis grid, and z_{in} is the crystal entrance facet position.

III. Time domain-presentation

The time domain presentation of the simulation is obtained using inverse Fourier transform:

$$E_\beta(x, y, z, t) = F(x, y)\left(e^{i\omega_\beta t}\int_{-\infty}^{+\infty} A_\beta(z, \omega)e^{-i\beta(\omega)z}e^{+i(\omega-\omega_\beta)t}df\right)$$

where the subscript β stands for the signal, pump and idler pulse. In other words:

$$(3.8)\, B_\beta(z,t) = \int_{-\infty}^{+\infty} B_\beta(z,\omega)e^{-i\beta(\omega)z}e^{+i(\omega-\omega_\beta)t}df = \Im^{-1}\left(B_\beta(z,\omega)e^{-i\beta(\omega)z}\right)$$

3.2 Novel time domain based simulation

3.2.1 Equations derivation in the time domain

The equations describing the nonlinear frequency generation process are presented in the time domain.

We begin with decomposing the electric field into plane waves:

$$(3.9)\ E(z,t) = \int_0^{+\infty} \frac{d\omega}{2\pi} |A(z,\omega)| \cos\left(\omega t - \beta(\omega)z + \sphericalangle A(z,\omega)\right) =$$

$$= \frac{1}{2} \int_0^{+\infty} \frac{d\omega}{2\pi} \left(A(z,\omega)e^{i\left(\omega t - \frac{\omega n(\omega)}{c}z\right)} + A^*(z,\omega)e^{-i\left(\omega t - \frac{\omega n(\omega)}{c}z\right)} \right)$$

$$= \int_{-\infty}^{+\infty} \frac{d\omega}{2\pi} \frac{1}{2}\left(A(z,\omega) + A^*(z,-\omega)\right)e^{+i\left(\omega t - \frac{\omega n(\omega)}{c}z\right)}$$

where $A(z,\omega)$ is the spectral density of the electric field amplitude, and $\beta(\omega) = \dfrac{\omega n(\omega)}{c}$ is the

frequency dependent electric field wavenumber.
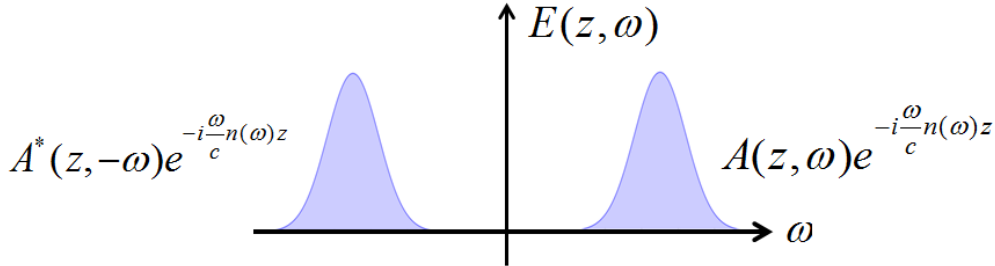
Figure 15. Frequency domain field presentation

We assume, as presented above, that $A(z,\omega)$ is centered around some central frequency and exist only for positive values of ω.

Defining the following amplitudes:

$$(3.10)\ C_\beta(z, \omega - \omega_\beta) = \tilde{A}_\beta(z,\omega) = A_\beta(z,\omega)e^{-i\beta(\omega)z}$$

where the subscript $\beta \in [s, p, i]$ stands for the signal, pump and idler pulses respectively, and ω_β is the corresponding pulse central frequency.

The pulses electric field can be easily represented in terms of C_β:

$$(3.11)\; E_\beta(z,t) = \frac{1}{2}\int_0^{+\infty}\frac{d\omega}{2\pi}\left(e^{i\omega t}C(z,\omega-\omega_\beta)+e^{-i\omega t}C^*(z,\omega-\omega_\beta)\right)$$

$$= \frac{1}{2}e^{i\omega_\beta t}\int_0^{+\infty}\frac{d\omega}{2\pi}e^{i(\omega-\omega_\beta)t}C_\beta(z,\omega-\omega_\beta)+\text{c.c} = \frac{1}{2}e^{i\omega_\beta t}C_\beta(z,t)+c.c$$

where $C_\beta(z,t)$ defined above is the Fourier transform of the electric field spectral density envelope centered at ω_β:

$$(3.12)\; C_\beta(z,t) = \int_0^{+\infty}\frac{d\omega}{2\pi}e^{i(\omega-\omega_\beta)t}C_\beta(z,\omega-\omega_\beta) = \Im\left(C_\beta(z,\omega-\omega_\beta)\right)$$

Detailed derivation of the equations dictating the frequency conversion process is presented in appendix B. To summarize, the equations obtained are the following:

- The TWM equations in the frequency domain:

$$(3.13)\; \partial_z\tilde{A}_s(z,\omega)+i\beta(\omega)\tilde{A}_s(z,\omega) = -i\frac{\omega}{c}\frac{\chi(z)}{n(\omega)}\tilde{A}_i(z,\omega)*\tilde{A}_p(z,\omega)$$

$$\partial_z\tilde{A}_p(z,\omega)+i\beta(\omega)\tilde{A}_p(z,\omega) = -i\frac{\omega}{c}\frac{\chi(z)}{n(\omega)}\tilde{A}_s(z,\omega)*\tilde{A}_i^*(z,-\omega)$$

$$\partial_z\tilde{A}_i(z,\omega)+i\beta(\omega)\tilde{A}_i(z,\omega) = -i\frac{\omega}{c}\frac{\chi(z)}{n(\omega)}\tilde{A}_s(z,\omega)*\tilde{A}_p^*(z,-\omega)$$

- The TWM equations in the time domain:

$$(3.14)\; \frac{\partial C_s(z,t)}{\partial z}+i\Im^{-1}\left(\beta(\omega+\omega_s)\Im C_s(z,t)\right) = -i\chi(z)\Im^{-1}\left(\frac{\omega+\omega_s}{n(\omega+\omega_s)c}\Im\left(C_i(z,t)C_p(z,t)\right)\right)$$

$$\frac{\partial C_p(z,t)}{\partial z}+i\Im^{-1}\left(\beta(\omega+\omega_p)\Im C_p(z,t)\right) = -i\chi(z)\Im^{-1}\left(\frac{\omega+\omega_p}{n(\omega+\omega_p)c}\Im\left(C_s(z,t)C_i^*(z,t)\right)\right)$$

$$\frac{\partial C_i(z,t)}{\partial z}+i\Im^{-1}\left(\beta(\omega+\omega_i)\Im C_i(z,t)\right) = -i\chi(z)\Im^{-1}\left(\frac{\omega+\omega_i}{n(\omega+\omega_i)c}\Im\left(C_s(z,t)C_p^*(z,t)\right)\right)$$

If $C_s(z,t), C_p(z,t), C_i(z,t)$ have bandwidth much smaller than their central frequency, it can be

assumed that $\omega + \omega_\alpha \approx \omega_\alpha$, hence:

$$(3.15) \; -i\chi(z)\mathfrak{I}^{-1}\left(\frac{\omega + \omega_i}{n(\omega + \omega_i)c} \mathfrak{I}\left(C_s(z,t)C_p^{\,*}(z,t)\right)\right) = -i\frac{\chi(z)\omega_i}{n(\omega_i)c}\mathfrak{I}^{-1}\left(\mathfrak{I}\left(C_s(z,t)C_p^{\,*}(z,t)\right)\right) =$$

$$= -i\frac{\chi(z)\omega_i}{n(\omega_i)c}\left(C_s(z,t)C_p^{\,*}(z,t)\right)$$

yielding the above set of equations:

$$(3.16) \; \frac{\partial C_s(z,t)}{\partial z} + i\mathfrak{I}^{-1}\left(\beta(\omega + \omega_s)\mathfrak{I}C_s(z,t)\right) = -i\frac{\chi(z)\omega_s}{n(\omega_s)c}C_i(z,t)C_p(z,t)$$

$$\frac{\partial C_p(z,t)}{\partial z} + i\mathfrak{I}^{-1}\left(\beta(\omega + \omega_p)\mathfrak{I}C_p(z,t)\right) = -i\frac{\chi(z)\omega_p}{n(\omega_p)c}C_s(z,t)C_i^{\,*}(z,t)$$

$$\frac{\partial C_i(z,t)}{\partial z} + i\mathfrak{I}^{-1}\left(\beta(\omega + \omega_i)\mathfrak{I}C_i(z,t)\right) = -i\frac{\chi(z)\omega_i}{n(\omega_i)c}C_s(z,t)C_p^{\,*}(z,t)$$

used in Ref. [27].

3.2.2 Simulation procedure in the time domain

I.   **Pulses definition**

The pulses are defined in the same manner described in section (3.1.3), except that now the pulses contain the same number of discrete points and are defined on the same grid (In contrary to Ni,Ns and Np spectral points defined in section (10.1.2):

- All pulses share the same time grid $t \in \left[-\dfrac{t_{\max}}{2}, \dfrac{t_{\max}}{2} \right]$.

- The time grid defines the frequencies vector of the pulse time envelope:

$f: \; f = \dfrac{1}{t_{\max}} \left[-\dfrac{N_t}{2} : 1 : \left(\dfrac{N_t}{2} - 1 \right) \right]$, where $dt = \dfrac{t_{\max}}{N_t}$ is the pulses resolution in the time domain.

II.   **Numerical integration**

The numerical integration is done using the split-step Fourier method. We divide the equation into two parts. The linear part accounts for dispersion, and the nonlinear part is responsible to the second order nonlinear optical generation through $\chi(z)$.

(3.17)

$$\frac{\partial}{\partial z}\begin{pmatrix} C_s(z,t) \\ C_p(z,t) \\ C_i(z,t) \end{pmatrix} = -i \underbrace{\begin{pmatrix} \Im^{-1}\big(\beta(\omega+\omega_s)C_s(z,\omega)\big) \\ \Im^{-1}\big(\beta(\omega+\omega_p)C_p(z,\omega)\big) \\ \Im^{-1}\big(\beta(\omega+\omega_i)C_i(z,\omega)\big) \end{pmatrix}}_{Linear\ Part} - i\frac{\chi(z)}{c} \underbrace{\begin{pmatrix} \Im^{-1}\left(\dfrac{\omega+\omega_s}{n(\omega+\omega_s)} \Im\big(C_i(z,t)C_p(z,t)\big) \right) \\ \Im^{-1}\left(\dfrac{\omega+\omega_p}{n(\omega+\omega_p)} \Im\big(C_s(z,t)C_i^*(z,t)\big) \right) \\ \Im^{-1}\left(\dfrac{\omega+\omega_i}{n(\omega+\omega_i)} \Im\big(C_s(z,t)C_p^*(z,t)\big) \right) \end{pmatrix}}_{Nonlinear\ Part}$$

The linear part of the equations is first calculated in the frequency domain:

$$(3.18) \; C_\alpha^{Disperesed}(z,\omega) = e^{-iL_\alpha(\omega)h} C_\alpha(z,\omega)$$

where $\alpha \in [s,p,i]$, $L_\alpha(\omega)$ is given by $(3.19)\; L_\alpha(\omega) = \beta(\omega+\omega_\alpha)$ and h is the spatial resolution on the optical axis. If we wish to work in a time reference that moves together with the pump pulse, all

amplitudes must be translated: $(3.20)\ C_\alpha(z,t) \to C_\alpha(z,t-t_p) = C_\alpha(z,t-\dfrac{h}{v_g(\omega_p)})$, where $v_g(\omega_p)$ is

the pump pulse group velocity and t_p is the time it takes the pump pulse to propagate distance h. In the

frequency domain Eq. (3.20) takes the form $C_\alpha(z,\omega+\omega_\alpha) \to e^{+i\frac{(\omega+\omega_\alpha)h}{v_g}} C_\alpha(z,\omega+\omega_\alpha)$, generalizing the

linear operator $L_\alpha(\omega)$ defined above: $(3.21)\ L_\alpha(\omega) = \beta(\omega+\omega_\alpha) - \dfrac{(\omega+\omega_\alpha)}{v_g(\omega_p)}$.

The nonlinear part of Eq. set (3.17) is then numerically integrated using 4'th order Runge-Kutta, where

the fields amplitudes are taken to be the dispersed ones defined in Eq. (3.18).

3.3 Simulation Examples

We display some simulation results for general impression. We present the simulation outputs for DFG process between 1um Gaussian pump pulse to 0.75um Gaussian signal pulse. The simulated grating is periodically poled Lithium Niobade crystal with periodicity of 20um. The simulated susceptibility is therefore $\chi(z) = sign\left(\cos\left(K_g z\right)\right)$, where the grating momenta K_g is given by $K_g = \dfrac{2\pi}{\left(\lambda = 20\mu m\right)}$.

All simulation parameters are summarized below:

Simulation parameter	Value
Pump Spectrum	Gaussian pulse
Pump wavelength [um]	1
Pump energy [mJ]	1
Pump temporal width (Transform limit) [ps]	100
Pump Mode Field Diameter (MFD) [um] (Mode Field Diameter - 4σ of the intensity profile)	$MFD_x = 0.5mm$ $MFD_y = 0.5mm$
Pump Average Area $[mm^2]\ \dfrac{\pi}{4}MFD_xMFD_y$	0.196
Signal Spectrum	Gaussian pulse
Signal wavelength [um]	0.75
Signal temporal width (Transform limit) [ps]	50
Signal Energy [uJ]	14
Signal Mode Field Diameter (MFD) [um] (Mode Field Diameter - 4σ of the intensity profile)	$MFD_x = 0.5mm$ $MFD_y = 0.5mm$
Signal Average Area $[mm^2]\ \dfrac{\pi}{4}MFD_xMFD_y$	0.196

The fields amplitudes demonstrated below are computed in the lab frame. The linear operator defined by Eq. (3.18) merely accounts to dispersion as defined in Eq. (3.19).
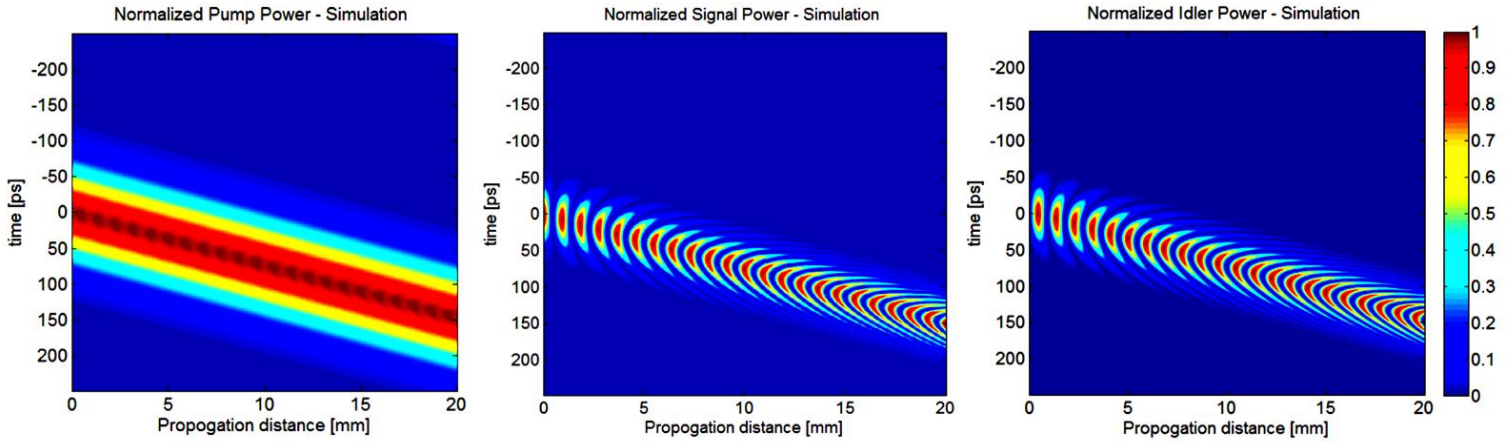
The time dynamics of the frequency conversion process is exhibited. The known behavior of periodic frequency conversion and back-conversion is typical to periodically poled crystals and was already addressed for the CW case in section (2.2).

The pulse temporal characteristics effect on the frequency conversion process can be further examined. For demonstration we present the time dependent conversion process when the pump pulse is 1ps delayed from the signal pulse:
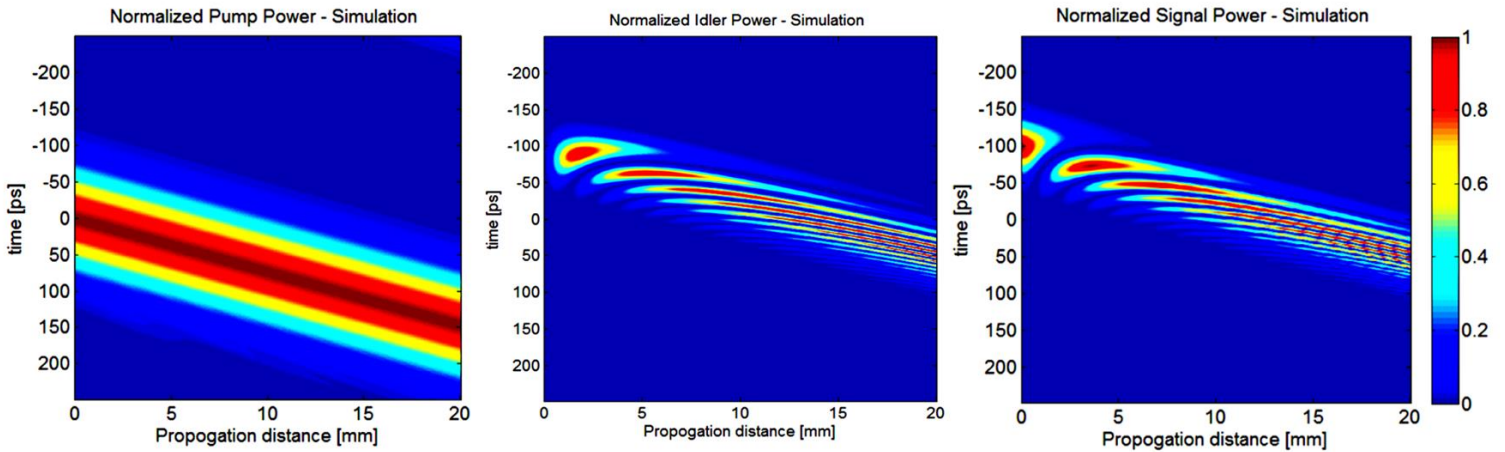
3.4 Time domain simulation vs frequency domain simulation – performance comparison

We compare the time domain simulation and the frequency domain simulation in terms of calculation time and absolute errors, defined as follows:

$$Absolute\ Error\,[\%] = 100 \cdot \frac{\left| E_{Total}(z_{out}) - E_{Total}(z_{in}) \right|}{E_{Total}(z_{in})}$$

where E_{Total} is the total energy of the system defined in section (3.5) and z_{in}, z_{out} are the crystal input and output facets respectively. We compared the simulation results for a DFG process between 1030nm pump pulse and a stretched Ti-Sappire oscillator pulse. Simulation parameters are provided below:

Simulation parameter	Value
Pump Spectrum	Gaussian pulse
Pump wavelength [nm]	1030
Pump energy [uJ]	20
Pump FWHM $\Delta\lambda$ [nm]	2
Pump chirp $\mathrm{Chirp}_{Pump}[10^{-27}s^2]$	50
Pump Mode Field Diameter (MFD) [um] (Mode Field Diameter - 4σ of the intensity profile)	$MFD_x = MFD_y = 0.5mm$
Pump Average Area $[mm^2]\ \frac{\pi}{4}MFD_xMFD_y$	0.196
Signal Spectrum	Ti-Sappire oscillator measured spectral shape
Signal Energy [uJ]	1
Signal chirp $\mathrm{Chirp}_{Signal}[10^{-27}s^2]$	0.5
Signal Mode Field Diameter (MFD) [um] (Mode Field Diameter - 4σ of the intensity profile)	$MFD_x = 0.5mm$ $MFD_y = 0.5mm$
Signal Average Area $[mm^2]\ \frac{\pi}{4}MFD_xMFD_y$	0.196
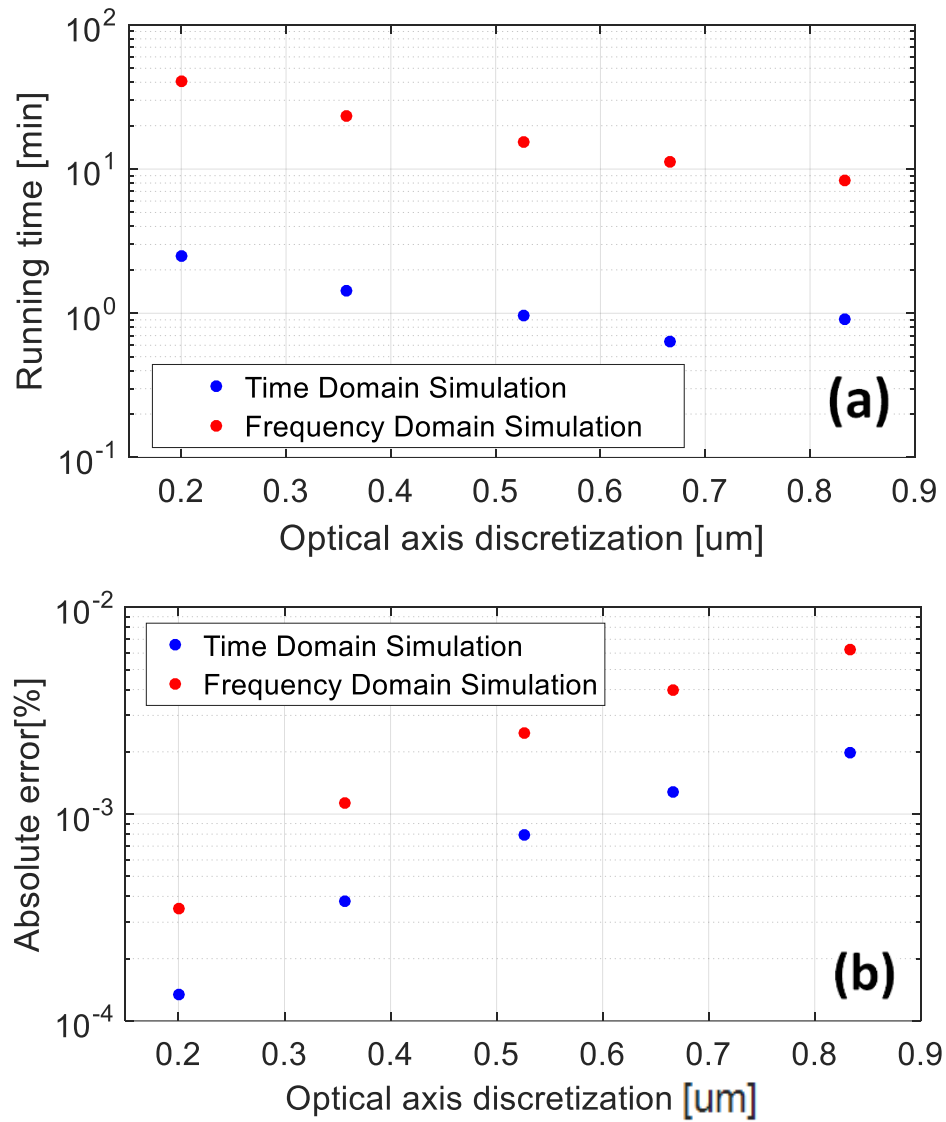
Figure 16. Performance comparison between the time domain simulation and the frequency domain simulation. (a) Running time comparison. (b) Absolute error comparison.

Although not presented herein, we calculated the Mean Square Error (MSE) of the difference between the output pulses spectral shape for various values of optical axis discretization, and deduced that steady simulation results, where the obtained MSE is smaller than 1%, are achieved for optical axis discretization smaller that $0.5 \mu m$ (more than 2000 calculations per mm). It is displayed, that the time domain simulation is both significantly faster (~X 10) and accurate (~X 3) than the frequency domain one.

3.5 Energy considerations in the presence of nonlinear polarization

In the following section, we present the energy flux equation in the presence on nonlinear polarization, and demonstrate its validity for the pulsed TWM Eq. set (3.13) obtained above.

It is derived in appendix C section (10.3.1), that the following energy flux equation holds:

$$(3.22)\quad \frac{\partial u_e}{\partial t} + \frac{\partial S}{\partial z} = -\frac{1}{2}\varepsilon_0\chi\vec{E}^2\frac{\partial E}{\partial t}$$

with the following notations:

- The electromagnetic field energy density $u_e = \frac{1}{2}\left(\varepsilon\vec{E}\cdot\vec{E} + \mu\vec{H}\cdot\vec{H} + \vec{P}_{NL}\cdot\vec{E}\right)$.

- The pointing vector $\vec{S} = \vec{E}\times\vec{H}$, calculated using the electromagnetic fields without taking into account their nonlinear polarization contribution.

Integrating the above Eq. (3.22) over both the spatial domain and the time domain $\int dxdydt$ results in the following:

$$\frac{\partial u_e}{\partial t} + \frac{\partial S}{\partial z} = -\frac{1}{2}\varepsilon_0\chi(z)\vec{E}^2\frac{\partial E}{\partial t} \Rightarrow$$

$$\int dxdy\frac{\partial u_e}{\partial t}dt + \frac{\partial\int Sdxdydt}{\partial z} = -\frac{1}{2}\varepsilon_0\chi(z)\int dxdy\vec{E}^2\frac{\partial E}{\partial t}dt$$

$$(3.23)\quad \int dxdy\, u_e\Big|_{t=-\infty}^{t=+\infty} + \frac{\partial\bar{S}(z)}{\partial z} = -\frac{1}{2}\varepsilon_0\chi(z)\int dxdy\frac{\vec{E}^3}{3}\Big|_{t=-\infty}^{t=+\infty}$$

As all pulses diminishes at $t=\pm\infty$, both u_e and $\vec{E}$ diminishes at $t=\pm\infty$, which leads:

$$(3.24)\quad \frac{\partial\bar{S}(z)}{\partial z} = 0$$

where $\bar{S}(z)$ is the total energy passing through plane perpendicular to the optical axis at place z

$$\bar{S}(z) = \iint_{\frac{Energy}{m^2\sec}} S_{m^2} \; dxdy\,dt_{\sec}$$

and the pointing vector $\vec{S} = \vec{E}\times\vec{H}$ is calculated using the fields separated from their nonlinear polarization contribution.

To validate that the obtained pulsed TWM Eq. set (3.13) is correct, we verified that it obeys the energy conservation indicated in Eq. (3.23). Detailed derivation of the energy conservation rule is presented in appendix C section (10.3.2) and summarized herein:

- The energy density E_d $\left[\dfrac{J}{m^2}\right]$ of pulse $\beta \in [S, P, I]$, where β stands for the signal, pump and idler pulses respectively is given by:

$$(3.25)\ E_d = \int_{t=-\infty}^{t=+\infty} S dt = \int_{t=-\infty}^{t=+\infty} \left(\vec{E}_\beta \times \vec{H}_\beta \right) dt = \int_0^{+\infty} df\, \frac{n(\omega)}{2\mu c} \left| A(z,\omega) \right|^2$$

The pulse spectral density is therefore defined as

$$(3.26)\ S(\omega) = \frac{n(\omega)}{2\mu c} \left| A(z,\omega) \right|^2$$

- The total energy of all three pulses is conserved:

$$(3.27)\ \frac{dE_d(z)}{dz} = \frac{d}{dz} \left(\int_0^{+\infty} df\, \frac{n(\omega)}{2\eta_0} \left(\left| A_i(z,\omega) \right|^2 + \left| A_p(z,\omega) \right|^2 + \left| A_s(z,\omega) \right|^2 \right) \right) = 0$$

3.7 Sum frequency simulation

The equations describing the generation of an idler pulse centered around ω_i, as the result of a DFG process between the signal and pump pulses centered around ω_s and ω_p respectively, were presented in the previous sections, where the idler central frequency was defined such that $\omega_i = \omega_s - \omega_p$. The equations describing the generation of a SFG process between the signal and pump pulses can be easily deduced by observing the DFG process as an SFG process between the idler and the pump pulses:

$$\omega_i + \omega_p = \omega_s$$

The equations describing SFG are therefore the same as those for the DFG process with the following subscript exchange:

$$i \rightarrow s$$
$$s \rightarrow i$$

The equations describing SFG are easily obtained:

$$(3.28)\ \partial_z \tilde{A}_i(z,\omega) + i\beta(\omega)\tilde{A}_i(z,\omega) = -i\frac{\omega}{c}\frac{\chi(z)}{n(\omega)}\tilde{A}_s(z,\omega)*\tilde{A}_p(z,\omega)$$

$$\partial_z \tilde{A}_p(z,\omega) + i\beta(\omega)\tilde{A}_p(z,\omega) = -i\frac{\omega}{c}\frac{\chi(z)}{n(\omega)}\tilde{A}_i(z,\omega)*\tilde{A}_s^{\ *}(z,-\omega)$$

$$\partial_z \tilde{A}_s(z,\omega) + i\beta(\omega)\tilde{A}_s(z,\omega) = -i\frac{\omega}{c}\frac{\chi(z)}{n(\omega)}\tilde{A}_i(z,\omega)*\tilde{A}_p^{\ *}(z,-\omega)$$

4. Phase matching technique – design procedure

In section ([2.3](#)) we briefly presented the QPM technique used to compensate the inherent phase mismatch between the interacting waves. While the method displayed accounts to periodic poling where the grating momenta is constant, i.e $K_g(z) = \Delta k$, in the following we present our phenomenological method for obtaining adiabatically varying phase mismatch designs. First, we present our method used to obtain first order QPM designs. later on, the developed method is used to account to higher order QPM crystals.

4.1 First order QPM design procedure

In order to obtain adiabatic evolution from one frequency to another, the phase mismatch of the interaction shall be swept from a large negative (positive) value to a large positive (negative) one. If the phase mismatch is swept adiabatically compared to the interaction strength κ, dictated by the adiabatic criteria (Eq. (2.22)), efficient conversion occurs. As presented in section ([2.4](#)), the adiabatic sweep allows efficient conversion for a range of frequencies, because diverse wavelengths can be generated in different locations along the optical axis, where the phase mismatch of the interaction is approximately zero $|\Delta k|/\kappa \ll 1$. It is therefore clear that in order to convert a broadband source, the grating momenta shall range between all values of phase-mismatch parameter $\Delta k(\omega)$ within the desired range of converted frequencies. The adiabatic design procedure of the grating function starts with a crude approximation, where the grating period $\Lambda(z) = \dfrac{2\pi}{K_g(z)}$ is increased linearly with the optical axis:

$$(4.1). \Lambda_{min} = \min\left(\frac{2\pi}{\Delta k(\omega)}\right), \Lambda_{max} = \max\left(\frac{2\pi}{\Delta k(\omega)}\right)$$

$$(4.2). \Lambda(z) = \Lambda_{min} + \frac{(\Lambda_{max} - \Lambda_{min})}{L_c}(z - z_{in})$$

where L_c is the crystal length and z_{in} is the crystal input facet.

The obtained grating function $K_g(z) = 2\pi / \Lambda(z)$ is than expanded in polynomial manner in terms of normalized optical coordinates $z_{norm} = (z - z_{in})/L_c$:

$$(4.3). K_g^{\,initial}(z) = \sum_{k=0}^{n} a_k z_{norm}{}^{k} = \sum_{k=0}^{n} a_k \left(\frac{z - z_{in}}{L_c}\right)^{k}$$

where n is the expansion order, and $\{a_k\}$ are the expansion coefficients. The obtained performance of the achieved design is than examined using the numerical simulation, and the conversion efficiency of the adiabatic process is calculated all over the desired range of generated frequencies. The initial grating

function design is then improved in an iterative manner using three parameters α, β and γ, that enable us to modify the simulated wavelength dependent conversion efficiency:

$$(4.4).\, K_g^{\,iterative}(z) = \sum_{k=0}^{n} a_k \left(\frac{\alpha z - z_{in}}{L_c} \right)^{\beta k} + \gamma$$

A scheme of the design process is presented:
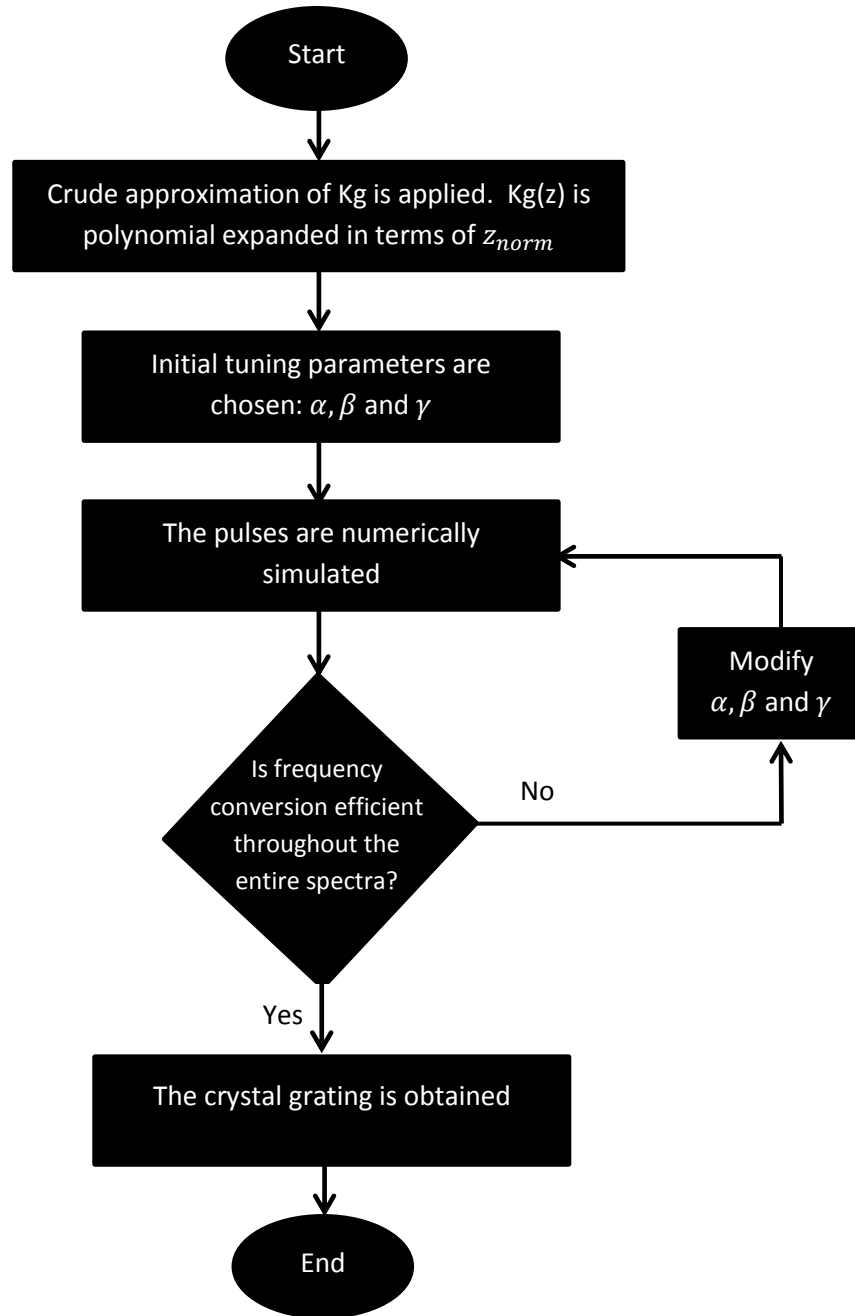
Figure 17. Design Method Scheme.

As described, optimizing over α, β and γ results in an optimal design for specific crystal length and pulses spectra. Each of the parameters has a different effect on the conversion efficiency curve:

- The parameter α determines the bandwidth of the conversion efficiency curve. Typical α values are in the range $\alpha \in [0.5, 1]$.

- The parameter β determines the slope of the conversion efficiency curve. Typical β values are in the range $\beta \in [0.5, 1.5]$.

- The parameter γ is used to apply fine tuning on the obtained design. γ deflects the entire conversion efficiency curve. Typical γ values are $O\left(10^4 \, cm^{-1}\right)$.
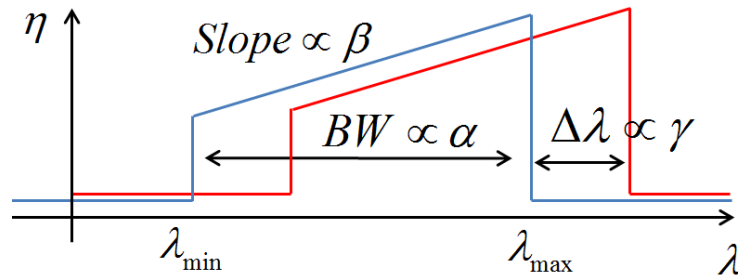
Figure 18. Conversion efficiency dependence with the grating parameters α, β and γ.

We continue with providing illustrative explanation to the conversion efficiency dependence with each of the parameters defined above. For clarity, the influence of each parameter on the grating momenta function $K_g(z)$ will be examined when all other parameters effects are diminished, i.e $\alpha = 1, \beta = 1$ and $\gamma = 0$.

a) **α parameter effect**:

The functional dependence between $K_g(z)$ and α is given by ($\beta = 1, \gamma = 0$):

$$K_g(z, \alpha) = K_g\left(\frac{\alpha z - z_{in}}{L_c}\right)$$

The modification to $K_g(z)$ can be stated as $K_g(z, \alpha) = K_g(\alpha z)$. The stretching imposed by α therefore modifies the possible momenta provided by the grating, hence altering the bandwidth of the conversion efficiency curve. The dependency of the rapid adiabatic passage (RAP) curve with the optical axis is therefore strongly affected by the parameter α, and the RAP curve slope variability is displayed in the following graphs for both $\alpha = 0.5$ and $\alpha = 1$.
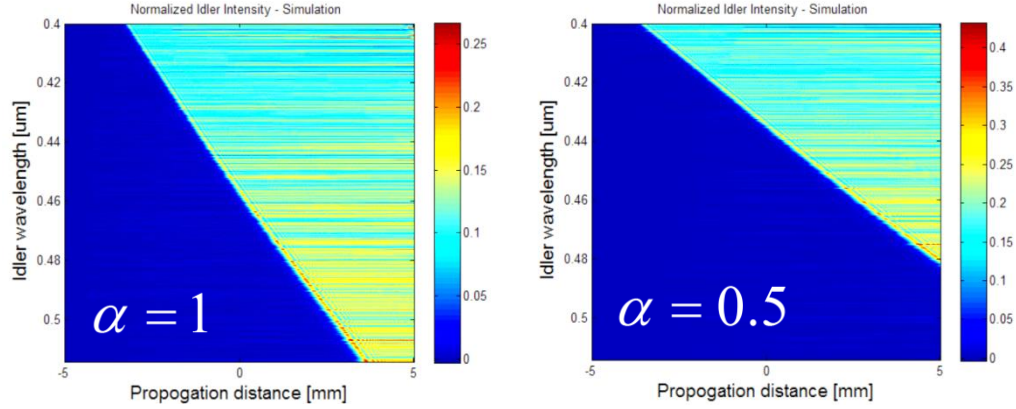
Figure 19. The parameter α changes the bandwidth of the conversion efficiency curve as it modifies the RAP position slope curve. The added possible momenta provided with enlarging α is manifested through the conversion efficiency curve.

b) **β parameter effect:**

The functional dependence between $K_g(z)$ and β is given by ($\alpha = 1, \gamma = 0$):

$$K_g(z) = K_g\left(z^{\beta}_{norm}\right)$$

To understand why β modifies the conversion efficiency slope, the grating momenta is depicted for various values of β. We recall the first crude approximation to $K_g(z)$:

$$K_g(z) = \frac{2\pi}{\Lambda_{\min} + \left(\Lambda_{\max} - \Lambda_{\min}\right) z_{norm}} = \frac{2\pi}{\left(\Lambda_{\max} - \Lambda_{\min}\right)} \left(\frac{1}{\dfrac{\Lambda_{\min}}{\left(\Lambda_{\max} - \Lambda_{\min}\right)} + z_{norm}} \right)$$

which up to a constant can be described as:

$$K_g(z) \propto \frac{1}{\dfrac{\Lambda_{\min}}{\left(\Lambda_{\max} - \Lambda_{\min}\right)} + z_{norm}}$$

For a DFG process between Ti-Sappire oscillator signal pulse and 1030nm pump pulse in a Mgcln, the crystal grating periods $\Lambda_{\min}$ and $\Lambda_{\max}$ are given by 14um and 20um respectively. For the corresponding SFG process $\Lambda_{\min}$ and $\Lambda_{\max}$ are given by 2.7um and 4.5um respectively. $\Lambda_{\min} / \left(\Lambda_{\max} - \Lambda_{\min}\right)$ is therefore quite close to 1, and the dependency between $K_g\left(z^{\beta}_{norm}\right)$ and β can be exhibited using $K_g(z,\beta) \propto \dfrac{1}{1 + z_{norm}^{\beta}}$.
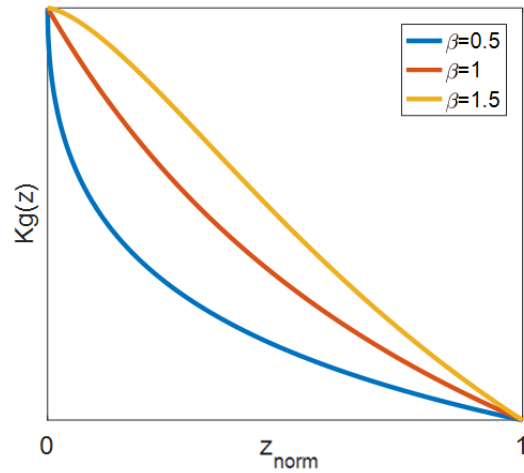
Figure 20. The parameter β effect on the grating momenta $K_g(z,\beta) \propto \left(1 + z_{norm}{}^\beta\right)^{-1}$.

It can be seen that by changing β, one alters the slope of the grating momenta $\dfrac{dK_g(z,\beta)}{dz}$ in two opposite directions compared to the case with $\beta = 1$: close to the crystal input facet, where the short wavelengths are generated, the slope absolute value $\left|\dfrac{dK_g(z,\beta)}{dz}\right|$ increases with $\beta < 1$ and decreases with $\beta > 1$, while near the crystal output facet, where the long wavelengths are generated, the opposite dependecny with β is observed: the slope absolute value $\left|\dfrac{dK_g(z,\beta)}{dz}\right|$ decreases with $\beta < 1$ and increases with $\beta > 1$. Because the adiabatic criteia in Eq. (2.22) strongly depends on the grating momenta slope, one can use β in order to alter the conversion efficieny of frequecies generated near the crystal input and output facets in opposite manner.
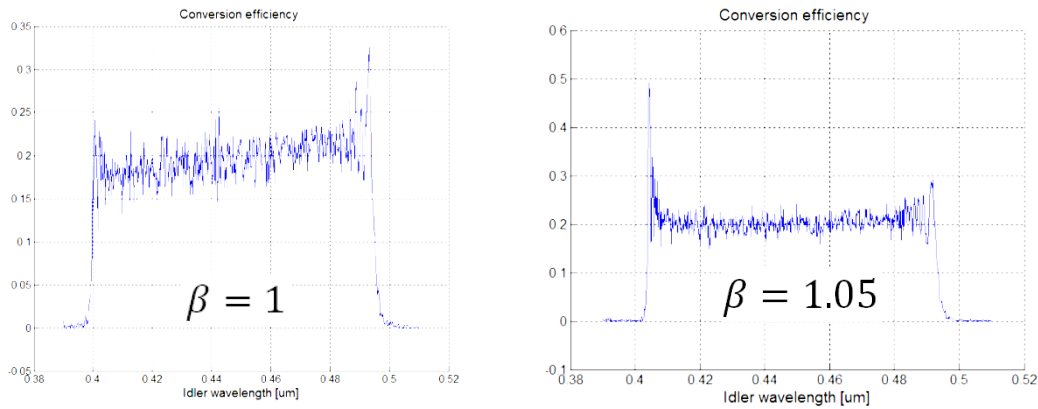
Figure 21. Enlarging β increases the conversion efficiencies of the wavelengths generated near the crystal input facet, while decreases the conversion efficiencies of wavelengths generated near the crystal output facet. Flat conversion efficiency curve is obtained.

c) **γ parameter effect:**

The functional dependence between $K_g(z)$ and γ is given by ($\alpha = 1, \beta = 1$):

$$K_g(z,\gamma) = K_g(z) + \gamma$$

The parameter γ is used to deflect the entire conversion efficiency curve, thus enabling us to carefully tune the maximal and minimal generated frequencies.
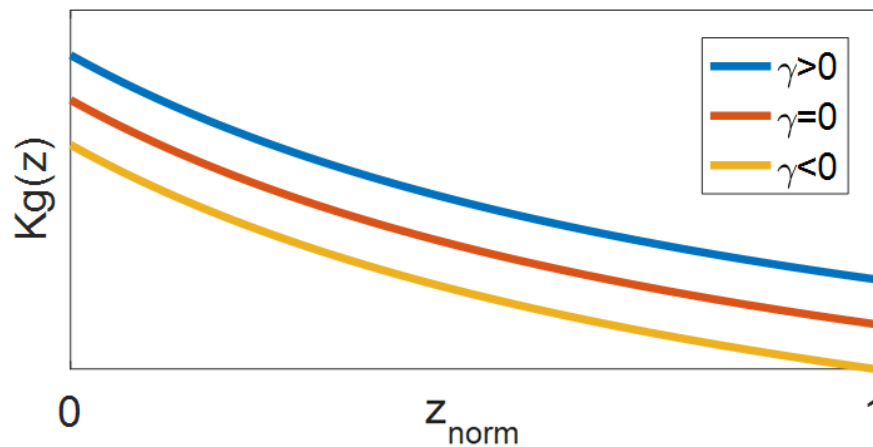
Figure 22. The parameter γ effect on the grating momenta.

Shifting the entire grating momenta changes the maximal and minimal momenta provided by the fluctuating second order nonlinear susceptibility, hence deflecting the entire conversion efficiency conversion curve.
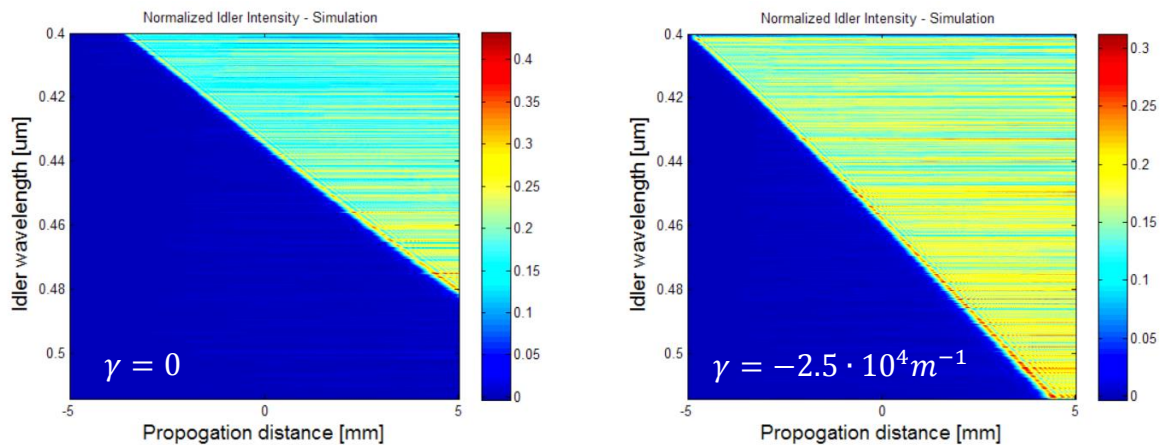
Figure 23. Conversion efficiency dependence with γ. The shifting of the entire conversion spectrum is observed.

4.2 High order QPM design procedure

As stated before, the second order nonlinear susceptibility $\chi(z)$ fluctuates between $+\chi$ to $-\chi$ according to the grating momenta $K_g(z)$: $\chi(z) = \chi \operatorname{sign}\left(K_g(z)z\right)$. When the batches in which the second order susceptibility is constant are too small, manufacturing limitations arise. In that case, high order QPM shall be taken into account. Applying high order QPM of order N_{QPM} in small intervals around specific location z, is achieved merely by multiplying the grating period $\Lambda(z) = \dfrac{2\pi}{K_g(z)}$ at the same location with the factor N_{QPM}, hence duplicating every batch in which $\chi(z)$ is constant with N_{QPM}: $\Lambda(z) = \dfrac{2\pi}{K_g(z)} \rightarrow \dfrac{2\pi}{K_g(z)} N_{QPM}$. In other words:

$$(4.5)\, K_g(z) \rightarrow \frac{K_g(z)}{N_{QPM}}$$

We present simulation results for the conversion efficiency of SFG process between 20nm bandwidth pump pulse centered around 1030nm and its second harmonic for various QPM orders:
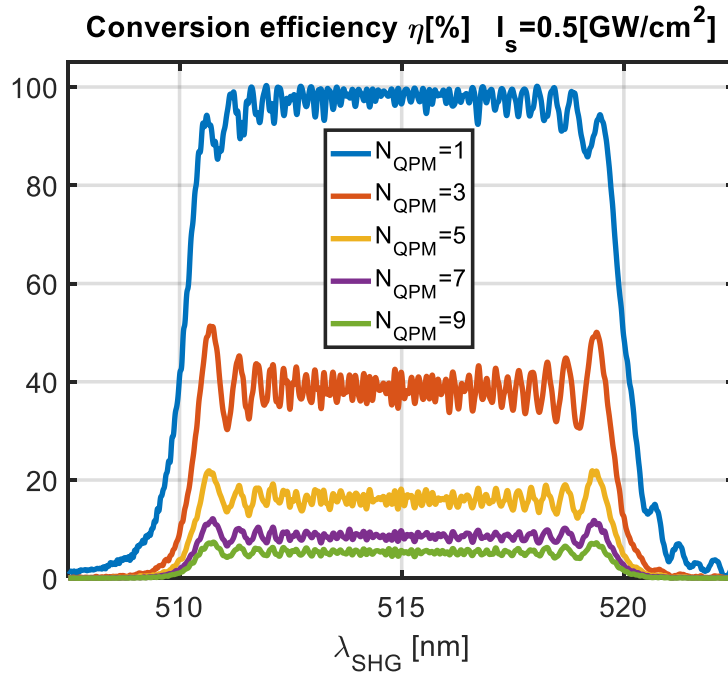
Figure 24. Conversion efficiency dependence with QPM order for a SFG process between undepleted signal and its second harmonic.

It is exhibited that in contrary to the periodically poled case, where the conversion efficiency dependence with the QPM order is given by $\eta \propto N^{-2}_{QPM}$ [28], the dependence in the case of adiabatically varying designs is much weaker. The supremacy of adiabatic designs over periodically poled crystals is presented in terms of sensitivity to the QPM order.

5. Article - Ultrafast adiabatic second harmonic generation

Ultrafast adiabatic second harmonic generation

Asaf Dahan[1], Assaf Levanon[1], Mordechai Katz[1,2] and Haim Suchowski[1,3,4]

[1] Raymond and Beverly Sackler School of Physics and Astronomy, Tel Aviv University, 69978 Tel Aviv, Israel
[2] Solid State Physics Department, Electro-Optics Division, Soreq NRC, Yavne 81800, Israel
[3] The center of Light-Matter Interaction, Tel Aviv University, 69978 Tel Aviv, Israel

E-mail: haimsu@post.tau.ac.il

CrossMark

Abstract

We introduce a generalization of the adiabatic frequency conversion method for an efficient conversion of ultrashort pulses in the full nonlinear regime. Our analysis takes into account dispersion as well as two-photon processes and Kerr effect, allowing complete analysis of any three waves with arbitrary phase mismatched design and any nonlinear optical process. We use this analysis to design an efficient and robust second harmonic generation, the most widely used nonlinear process for both fundamental and applied research. We experimentally show that such design not only allows for very efficient conversion of various of ultrashort pulses, but is also very robust to variations in the parameters of both the nonlinear crystal and the incoming light. These include variation of more than 100 °C in the crystal temperature, a wide bandwidth of up to 75 nm and a chirp variation of 300 fs to 3.5 ps of the incoming pulse. Also, we show the dependency of the adiabatic second harmonic generation design on the pump intensity and the crystal length. Our study shows that two photon absorption plays a critical role in such high influence nonlinear dynamics, and that it must be considered in order to achieve agreement with experimental results.

Keywords: nonlinear optics, ultrafast phenomena, adiabatic processes, frequency conversion

(Some figures may appear in colour only in the online journal)

1. Introduction

Second harmonic generation (SHG) is the most basic nonlinear optical process, yet the most powerful and widely used. Since the first demonstration of the SHG process right after introducing the first laser [1], it revolutionized the field of light–matter interactions, allowing a new way for exploring atomic, molecular and condensed matter systems. Due to its simplicity, requiring solely shining a single laser beam into a nonlinear crystal, it gained popularity among diverse applications from nonlinear spectroscopy, metallurgy, photoinduced dynamics in 2D and condensed matter dynamics, noninvasive background free diagnostics, and the generation of new color sources [2–5]. It is, however, generally difficult to obtain efficient and robust conversion from a pump pulse to its harmonics for a broad range of colors. This is mainly due to the lack of phase mismatch (lack of momentum conservation) between the interacting waves, which conventionally can be compensated only for a narrow band of frequencies. In the fully nonlinear regime, where none of the interacting waves can be considered to be undepleted, efficient broadband conversion is even more difficult due to its complex dynamics. Although, in the past, several methods were suggested to deal with the conversion of a broadband source, such as short birefringent crystals [6], multi-periodic modulation [7], chirp patterns [8, 9], temperature gradient manipulations [10, 11]

[4] This article belongs to the special issue: Emerging Leaders, which features invited work from the best early-career researchers working within the scope of *Journal of Physics: Condensed Matter*. This project is part of the *Journal of Physics* series' 50th anniversary celebrations in 2017. Haim Suchowski was selected by the Editorial Board of *Journal of Physics: Condensed Matter* as an Emerging Leader.

1

and random oriented crystal [12]. Those indeed achieved very broadband conversion, but at the expense of limited conversion efficiencies.

In recent years, a new direction in frequency conversion has emerged—adiabatic frequency conversion—a method that is based on adiabatic evolution of the nonlinear optics dynamics. The suggested method enables to overcome the tradeoff between conversion efficiency and bandwidth [13, 14]. Although it was first considered theoretically for SHG by Baranova [15], the initial extensive experimental research was performed in sum/difference frequency conversion (SFG/DFG) in the undepleted pump approximation, offering the use of SU(2) dynamical symmetry with the analogous mechanism of Landau–Zener transition [16]. In the past few years, the fully nonlinear regime received special attention. Reasearch on adiabatic interactions with nonlinear dynamics as adiabatic OPA and OPO was conducted by Phillips *et al* [17, 18], Heese *et al* [19–21] and Yaacobi [22]. In parallel, adiabatic DFG allowed an efficient conversion of near-IR few cycle pulses to octave-spanning mid-IR pulses [23, 24]. A general physical model of adiabatic frequency conversion in the fully nonlinear dynamics regime, was presented recently by Porat and Arie [25]. In the past year, a first proof of adiabatic SHG was demonstrated with nanosecond pulses [26], exhibiting an unmatched temperature robustness. Yet, the efficient SHG conversion of ultrashort pulses is still lacking. Here, the adiabatic conversion method is generalized to include efficient SHG conversion of ultrashort pulses. In our analysis, we do not only solve the full nonlinear dynamics with arbitrary interacting ultrashort pulses and nonlinear phase-mismatched design, but also take into account Kerr effect and two photon absorption of the generated SHG. This will be shown to be a critical aspect in our experimental observations that was lacking in all previous research of adiabatic frequency conversion.

2. Theoretical background

Let us start by developing the fully nonlinear dynamical equations that dictate nonlinear conversion of any three wave mixing, and in particular of SHG. We will present the full nonlinear equations in the time domain, including two photon absorption (TPA) and Kerr effect, and will discuss the adiabaticity criteria for an efficient frequency conversion process.

2.1. Nonlinear dynamics in three wave mixing

The electric field wave equation, in the presence of nonlinear polarization is given by

$$\nabla^2 \vec{E}(\vec{r},t) - \mu\epsilon_0 n^2 \frac{\partial^2 \vec{E}(\vec{r},t)}{\partial t^2} = \mu \frac{\partial^2 \vec{P}_{NL}(\vec{r},t)}{\partial t^2} \quad (1)$$

where μ is the material permeability, ϵ_0 is the vacuum permittivity, n is the material refractive index and $\vec{P}_{NL}(\vec{r},t)$ is the nonlinear polarization [27]. In our analysis we assume that the electric field is planar. One can therefore write:

$$\vec{E}(\vec{r},t) = \frac{1}{2\pi}\int_0^{+\infty}\frac{1}{2}(\vec{A}(z,\omega)e^{i(\omega t - \beta(\omega)z)} + \text{c.c})d\omega \quad (2)$$

where $\vec{A}(z,\omega)$ is the field amplitude spectral density and $\beta(\omega) = \frac{\omega n(\omega)}{c}$ is the material wave vector. By changing the integral limits one can deduce the electric field: $\vec{E}(z,\omega) = (\vec{A}(z,\omega) + \vec{A}^*(z,-\omega))e^{-i\beta(\omega)z}$. By applying Fourier transform to equation (1), substitute $\vec{E}(z,\omega)$, and assuming the slowly varying amplitude approximation $|\frac{\partial^2\vec{A}(z,\omega)}{\partial^2 z}| \ll |\beta(\omega)\vec{A}(z,\omega)|$, equation (1) takes the form:

$$\left(\frac{\partial\vec{A}(z,\omega)}{\partial z} + \frac{\partial\vec{A}^*(z,-\omega)}{\partial z}\right)e^{-i\beta(\omega)z} = -\mu\omega^2\vec{P}_{NL}(z,\omega). \quad (3)$$

Without loss of generality, we will assume that the electric field is polarized along the x direction. By applying Fourier transform to the nonlinear polarization term $\vec{P}_{NL}(z,t) = 2\epsilon_0\chi(z)E^2(z,t)\hat{x}$ and substituting it into equation (3), the master equation for second order nonlinear interactions is deduced:

$$\left(\frac{\partial\vec{A}(z,\omega)}{\partial z} + \frac{\partial\vec{A}^*(z,-\omega)}{\partial z}\right)e^{-i\beta(\omega)z}$$
$$= -2i\frac{\omega\chi(z)}{cn(\omega)}E(z,\omega)*E(z,\omega) \quad (4)$$

where '$*$' stands for convolution. We continue the derivation by expanding the electric field in terms of the interacting pulses: $E(z,\omega) = (E_1(z,\omega) + E_2(z,\omega) + E_3(z,\omega))$, where $E_j(z,\omega) = (A_j(z,\omega) + A_j^*(z,-\omega))e^{-i\beta(\omega)z}$ for $j = 1, 2, 3$. $A_1(z,\omega), A_2(z,\omega)$ and $A_3(z,\omega)$ are centered around frequencies ω_1, ω_2 and ω_3 respectively, obeying $\omega_1 + \omega_2 = \omega_3$. Inserting the electric fields into equation (4) and observing the spectral shape of the convoluted signals, one can deduce the following set of equations:

$$\frac{\partial B_1(z,\omega)}{\partial z} + i\beta(\omega)B_1(z,\omega) = -i\frac{\omega\chi(z)}{cn(\omega)}B_3(z,\omega)*B_2^*(z,-\omega)$$
$$\frac{\partial B_2(z,\omega)}{\partial z} + i\beta(\omega)B_2(z,\omega) = -i\frac{\omega\chi(z)}{cn(\omega)}B_3(z,\omega)*B_1^*(z,-\omega)$$
$$\frac{\partial B_3(z,\omega)}{\partial z} + i\beta(\omega)B_3(z,\omega) = -i\frac{\omega\chi(z)}{cn(\omega)}B_1(z,\omega)*B_2(z,\omega) \quad (5)$$

where $B_{1,2,3}(z,\omega) = A_{1,2,3}(z,\omega)e^{-i\beta(\omega)z}$. In the continuous wave (CW) case, the electric field is monochromatic: $B_j(z,\omega) = B_j\delta(\omega - \omega_j)$ where $j = 1, 2, 3$. Substitution of the monochromatic amplitudes into equations (5) yields the conventional set of equations (in terms of A_j) as presented in [27]:

$$\frac{\partial A_1}{\partial z} = -i\gamma_1 A_3 A_2^* e^{-i\Delta\beta z}$$
$$\frac{\partial A_2}{\partial z} = -i\gamma_2 A_3 A_1^* e^{-i\Delta\beta z}$$
$$\frac{\partial A_3}{\partial z} = -i\gamma_3 A_1 A_2 e^{+i\Delta\beta z} \quad (6)$$

2

where $\gamma_j = \frac{\omega_j \chi(z)}{cn(\omega_j)}$ is the coupling coefficient and $\Delta\beta = (\beta(\omega_3) - \beta(\omega_2) - \beta(\omega_1))$ is the phase mismatch between the interacting waves. Using equations (6) it is possible to design the nonlinear second susceptibility $\chi(z)$ in order to compensate the inherent phase mismatch $\Delta\beta$. The obtained design will work fine even in the case of quasi-monochromatic waves, having their bandwidth much smaller than their central frequency, thus having an inherent phase mismatch $\Delta\beta$ which is nearly the same as in the CW regime. It is possible to use equations (6) also for ultrashort pulses whenever group-velocity mismatch (GVM) between the interacting waves can be neglected. For example, in the case of 10 mm SHG potassium titanyl phosphate (KTP) crystal designed to convert 1030 nm pump pulse into 515 nm SHG pulse, the maximum GVM along the crystal can be at most $\tau_{GVM} = L(v_g^{-1}(\lambda_{SHG}) - v_g^{-1}(\lambda_{Pump})) = 6.8$ ps. It is therefore not possible to use the conventional equations (6) to calculate the dynamics in the picosecond regime.

For the ultrashort pulse case, we shall continue by describing every pulse centered around central frequency ω_j as a multiplication of slowly varying time domain amplitude function modulated with the central pulse frequency: $B_j(z, \omega) = \mathscr{F}(B_j(z, t)e^{i\omega_j t})$. We will use the following identities:

$$\mathscr{F}^{-1}(B_j(z, \omega - \omega_j)) \equiv e^{i\omega_j t}B_j(z, t)$$
$$\mathscr{F}^{-1}(B_j(z, \omega - \omega_j) * B_l(z, \omega - \omega_l))_{\omega + \omega_m}$$
$$\equiv e^{i(\omega_j + \omega_l - \omega_m)t}B_j(z, t)B_l(z, t) \qquad (7)$$

where $j, l, m \in [1, 2, 3]$. Applying inverse Fourier transform to equations (5) and using identities (7), the general nonlinear dynamical equations are obtained in the time domain:

$$\frac{\partial B_1(z, t)}{\partial z} + i\mathscr{F}^{-1}(\beta(\omega + \omega_1)B_1(z, \omega))$$
$$= -i\chi(z)\mathscr{F}^{-1}\left(\frac{\omega + \omega_1}{cn(\omega + \omega_1)}\mathscr{F}(B_3(z, t)B_2^*(z, t))\right)$$
$$\frac{\partial B_2(z, t)}{\partial z} + i\mathscr{F}^{-1}(\beta(\omega + \omega_2)B_2(z, \omega))$$
$$= -i\chi(z)\mathscr{F}^{-1}\left(\frac{\omega + \omega_2}{cn(\omega + \omega_2)}\mathscr{F}(B_3(z, t)B_1^*(z, t))\right)$$
$$\frac{\partial B_3(z, t)}{\partial z} + i\mathscr{F}^{-1}(\beta(\omega + \omega_3)B_3(z, \omega))$$
$$= -i\chi(z)\mathscr{F}^{-1}\left(\frac{\omega + \omega_3}{cn(\omega + \omega_3)}\mathscr{F}(B_1(z, t)B_2(z, t))\right). \qquad (8)$$

The left-hand side term $\beta(\omega + \omega_j)B_j(z, \omega)$ accounts for the dispersion the pulses experience through propagation along the crystal, while the right-hand side accounts for the nonlinear interaction between the pulses. In the case of narrowband pulses, where the pulse bandwidth is much smaller than their central frequency, $(\omega + \omega_j) \approx \omega_j$ and equations (8) takes the form:

$$\frac{\partial B_1(z, t)}{\partial z} + i\mathscr{F}^{-1}(\beta(\omega + \omega_1)B_1(z, \omega))$$
$$= -i\frac{\chi(z)\omega_1}{cn_1}B_3(z, t)B_2^*(z, t)$$
$$\frac{\partial B_2(z, t)}{\partial z} + i\mathscr{F}^{-1}(\beta(\omega + \omega_2)B_2(z, \omega))$$
$$= -i\frac{\chi(z)\omega_2}{cn_2}B_3(z, t)B_1^*(z, t)$$
$$\frac{\partial B_3(z, t)}{\partial z} + i\mathscr{F}^{-1}(\beta(\omega + \omega_3)B_3(z, \omega))$$
$$= -i\frac{\chi(z)\omega_3}{cn_3}B_1(z, t)B_2(z, t) \qquad (9)$$

which are the equations obtained in [28].

The equations for the SHG process can be easily deduced from equations (8). The pump pulse, centered around $\omega_1 = \omega_2 = \omega_p$ interacts with itself and generates the SHG pulse around $\omega_{SHG} = \omega_3 = 2\omega_p$:

$$\frac{\partial B_{SHG}(z, t)}{\partial z} + i\mathscr{F}^{-1}(\beta(\omega + \omega_{SHG})B_i(z, \omega))$$
$$= -i\chi(z)\mathscr{F}^{-1}\left(\frac{\omega + \omega_{SHG}}{cn(\omega + \omega_{SHG})}\mathscr{F}\left(B_p^2(z, t)\right)\right)$$
$$\frac{\partial B_p(z, t)}{\partial z} + i\mathscr{F}^{-1}(\beta(\omega + \omega_p)B_p(z, \omega))$$
$$= -i\chi(z)\mathscr{F}^{-1}\left(\frac{\omega + \omega_p}{cn(\omega + \omega_p)}\mathscr{F}\left(B_{SHG}(z, t)B_p^*(z, t)\right)\right). \qquad (10)$$

In our analysis we also take into account nonlinear processes that are propotional to the real and imaginary parts of the third order nonlinearity χ^3, namely Kerr effect and TPA. When the optical material experiences TPA, an intensity density dependent term is added to the linear absorption, constituting an absorption coefficient $\alpha = \alpha_0 + \beta I$, where $\beta(mW^{-1})$ is the two photon absorption coefficient [27]. KTP absorbs in the range $\lambda < 350$ nm, hence, two photon absorption may limit the performance of the SHG crystal if the generated SHG wavelength is smaller than 700 nm. The second effect we take into account is the Kerr effect, which is the physical process constituting an intensity dependent refractive index term [27] $n = n_0 + n_2 I$, where n_0 is the weak-field refractive index and $n_2(m^2 W^{-1})$ is the second-order index of refraction.

The incorporation of both TPA and Kerr effect to the simulation is done in the time domain:

$$\frac{\partial B_{SHG}(z, t)}{\partial z} + i\mathscr{F}^{-1}(\beta(\omega + \omega_{SHG})B_{SHG}(z, \omega))$$
$$= -i\chi(z)\mathscr{F}^{-1}\left(\frac{\omega + \omega_{SHG}}{cn(\omega + \omega_{SHG})}\mathscr{F}\left(B_p^2(z, t)\right)\right)$$
$$- \frac{\beta}{2}I_{SHG}(z, t)B_{SHG}(z, t)$$
$$- ik_0 n_2(\omega_{SHG})\left(I_p(z, t) + I_{SHG}(z, t)\right)B_{SHG}(z, t)$$
$$\frac{\partial B_p(z, t)}{\partial z} + i\mathscr{F}^{-1}(\beta(\omega + \omega_p)B_p(z, \omega))$$
$$= -i\chi(z)\mathscr{F}^{-1}\left(\frac{\omega + \omega_p}{cn(\omega + \omega_p)}\mathscr{F}\left(B_{SHG}(z, t)B_p^*(z, t)\right)\right)$$
$$- ik_0 n_2(\omega_p)\left(I_p(z, t) + I_{SHG}(z, t)\right)B_p(z, t) \qquad (11)$$
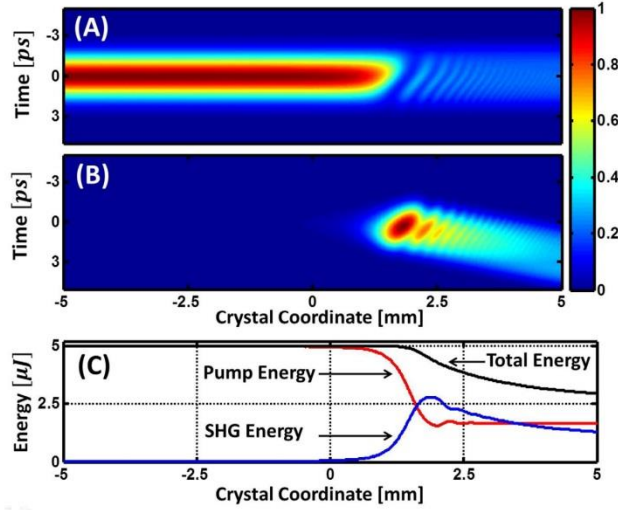
3

Figure 1. Numerical propagation simulation of the pump pulse and its SHG in the presence of two-photon absorption. (A) The pump pulse intensity as a function of propagation length (*x*-axis). The pump intensity remains centered around the figure time axis (*y*-axis) because the presented time frame moves relative to the pump pulse. (B) The generated SHG intensity as a function of propagation length (*x*-axis). The SHG pulse, having smaller wavelengths, moves slower than the pump pulse as expected in the normal dispersion regime. (C) The pump (solid red) and the SHG (solid blue) energies as a function of propagation length. The total energy (solid black) is not conserved due to TPA of the generated SHG.

where $I_p(z,t) = \frac{|B_p(z,t)|^2 n_p}{\eta_0}$ and $I_{SHG}(z,t) = \frac{|B_{SHG}(z,t)|^2 n_{SHG}}{2\eta_0}$.

2.2. Adiabaticity condition in the nonlinear regime

In an efficient second harmonic generation process, most of the pump energy is transferred to the SHG pulse energy. The pump is therefore by definition depleted. The comprehensive theory for an adiabatic frequency conversion process, involving three wave mixing (TWM) was developed by Porat and Adie [25]. The adiabacity criteria for the general case, where the interacting waves may be depleted, was developed in the CW regime. Start with defining the relative strength of the phase mismatch compared to the nonlinearity $\Delta\Gamma = \Delta\beta/\sqrt{\gamma_1\gamma_2\gamma_3}$, and continue with defining the scaled propogation length $\xi = z\sqrt{\gamma_1\gamma_2\gamma_3}$. The adiabaticity criteria takes the form:

$$\left| \frac{d(P_1^\pm/P_3)}{d\Delta\Gamma} \frac{d\Delta\Gamma}{d\xi} \right| \ll \nu \qquad (12)$$

where $(P_1^\pm, Q_1^\pm)$ are the canonical coordinates of the two stationary states of the system, P_1 is the photon flux excess of the two low-frequency waves over the high-frequency wave, P_3 is the total photon flux and $\nu = \sqrt{\left.\frac{\partial^2 H}{\partial Q_1^2}\right|_{P_1^\pm Q_1^\pm} \left.\frac{\partial^2 H}{\partial P_1^2}\right|_{P_1^\pm Q_1^\pm}}$ is the frequency in which the system orbits its fixed point in the phase space. The adiabacity condition in equation (12) is suitable for the CW regime or to a narrow-band pulses, and cannot

be used when analyzing ultrashort pulses with bandwidth not negligible compared to their central frequency. Adiabatic evolution theory for ultra-short pulses is still absent, and numerical simulations are therefore required.

3. Numerical approach and predictions

The numerical simulations of equations (10) were performed by implementing the split-step Fourier method for the linear part of the equations, while the numerical integration for the nonlinear part is implemented using the 4th order Runge–Kutta method. The simulation procedure for every integration step Δz starts with accounting to the linear term. The pulses are first propagated:

$$C_{SHG/p} = e^{-iL_{SHG/p}(z,\omega)\Delta z} B_{SHG/p}(z,\omega)$$

$$L_{SHG/p}(z,\omega) = \beta(\omega + \omega_{SHG/p}) - \frac{(\omega + \omega_{SHG/p})}{v_g(\omega_p)}. \qquad (13)$$

All pulses are simulated relative to a time reference that moves together with the pump pulse, hence, a time domain translation term $\frac{(\omega + \omega_{SHG/p})}{v_g(\omega_p)}$ is added to the dispersion.

The second step is to account for the nonlinear term, which is numerically integrated in the time domain. Using the amplitudes $C_{SHG/p}(z,\omega)$, $B_{SHG/p}(z + \Delta z, \omega)$ are calculated. The numerical procedure is iteratively repeated until the numerical integration is done all over the crystal optical axis. An example of the simulated amplitudes in the time domain is shown in figure 1 .
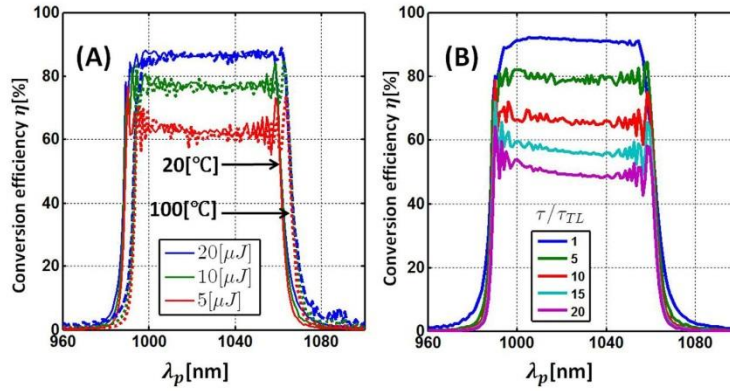
Figure 2. Simulated conversion efficiency as a function of central pump wavelength, for different energies and pump chirp. (A) The conversion efficiency is simulated for several energies for both $T = 20\,°C$ and $T = 100\,°C$. (B) The conversion efficiency curve is simulated for several input pump chirp.

We would like to numerically examine the robustness of the designed SHG crystal without taking into account undesired parasitic effects as TPA. The crystal grating function $K_g(z)$ is

$$K_g(z_{cm}) = (118.24 z_{cm}^3 - 45.19 z_{cm}^2 - 997.92 z_{cm} + 7957.08)\, cm^{-1}$$

where the second order nonlinear susceptibility is given by $\chi(z) = \chi\, \text{sign}(\cos(K_g z))$, thus fluctuating between $+\chi$ to $-\chi$ in batches spanning between $3.5\,\mu m$ to $4.5\,\mu m$. The crystal dimensions are depicted in figure 3. The crystal grating period $\Lambda = \frac{2\pi}{K_g(z)}$ adiabatically changes from $\Lambda = 7.4\,\mu m$ to $\Lambda = 8.4\,\mu m$ along the optical axis of the nonlinear crystal.

We define the energy conversion efficiency of the crystal to be the ratio between the generated SHG pulse energy to the input pump pulse energy:

$$\eta = \frac{E_{SHG}(z_{final})}{E_p(z_{initial})}.$$

In figure 2(A) the crystal conversion efficiency is simulated for an input Gaussian pump pulse with $\Delta\lambda_{FWHM} = 1$ nm, $\Delta\tau_{FWHM} = 4$ ps, $T = 20\,°C$ and mode field diameter of $0.5\,mm$ for several energies. It is therefore shown that efficient wideband ultrashort second harmonic generation is feasible in a single KTP crystal, exhibiting a flat conversion efficiency curve with a bandwidth of $75\,nm$, spanning from 980 to $1070\,nm$. It is shown that decreasing the energy lowers the typical conversion efficiency, while maintaining the plateau in the conversion efficiency curve.

We also added to figure 2(A) the conversion efficiency for $T = 100\,°C$ in the dashed line. It is clear that the design is not prone to temperature changes. The reason for its robustness is the fact that the conversion efficiency will be dramatically altered only for wavelengths having their rapid adiabatic passage (RAP) near the crystal edges, thus sensitive to refractive index change that might change the RAP position outside or inside the crystal. Refractive index dependence with temperature was taken from [29].

We have also examined the robustness of the adiabatic design to different pulse chirps. In figure 2(B), the conversion efficiency is plotted for the same Gaussian pulse as in figure 2(A), being chirped in the time domain. τ/τ_{TL} is the ratio between the chirped pulse full width half maximum (FWHM) in the time domain and the transform limited pulse FWHM. The interaction term generating the SHG pulse is proportional to $B_p^2(z, t)$, hence proportional to the pump intensity. It is therefore clear why stretching the pulses in the time domain has the same effect as lowering the pulse energy, leaving the pump intensity unchanged.

4. Experimental results

The experiment setup is depicted in figure 3. The second output of an optical parametric chirped pulse amplification (OPCPA) system (Venteon dual) served as the front end, delivering $10\,\mu$J, 2 Mhz pump pulses. The CPA beam is then focused on an adiabatically aperiodically poled KTP (adAPKTP) crystal, extraordinary-wave (e-wave) polarized along the crystal c-axis. The residual pump and the generated SHG were seperated using a dichroic mirror around $950\,nm$. The spectrum of the pump and the generated SHG pulse was measured using a HORIBA spectrometer and displayed in figure 3, thus demonstrating an efficient conversion efficiency all over the pump spectra between $1020–1040\,nm$.

The adAPKTP domain structure was fabricated in uncoated, $1\,mm$ thick z-cut, flux grown KTP plates by 'Raicol Crystals'. Conventional photolithographic process and electric-field poling were used to create the designed domain structure [30, 31].

It was possible to control both the temporal and the spectral properties of the pump pulse using a mechanism located inside the venteon CPA module. By spatially stretching the beam spectra using a grating, it was feasible to truncate parts of the scattered beam thus controlling its bandwidth, altering the measured $20\,nm$ pump spectra presented in figure 3 into a Gaussian-shape pump pulse centered around $1036\,nm$ with a bandwidth of $10\,nm$. An adjustable mirror, placed after
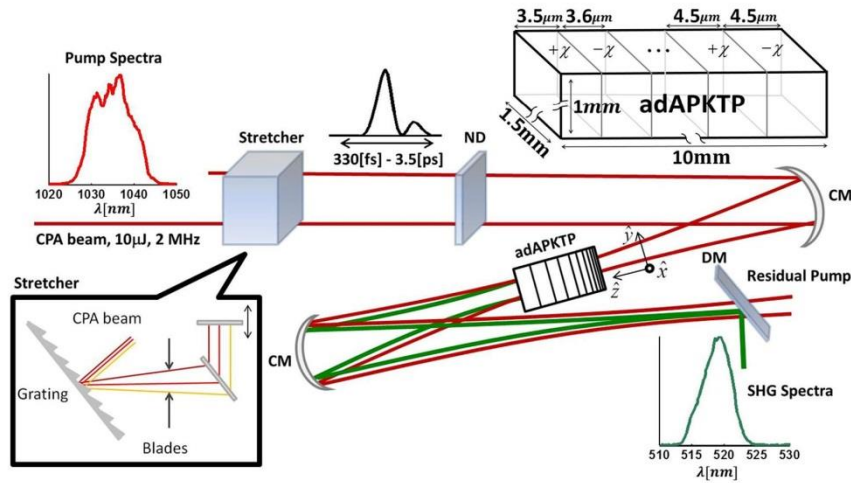
Figure 3. The adiabatic SHG experimental apparatus. ND—neutral density filter, CM—curved mirror, DM—dichroic mirror, adAPKTP—the designed crystal. Left upper inset—the measured pump spectra, left lower inset—the inner CPA module (stretcher), enabling us to control both the time domain and the spectral domain characteristics of the pump pulse, right upper inset—the crystal physical dimensions, right lower inset–the measured SHG spectra.
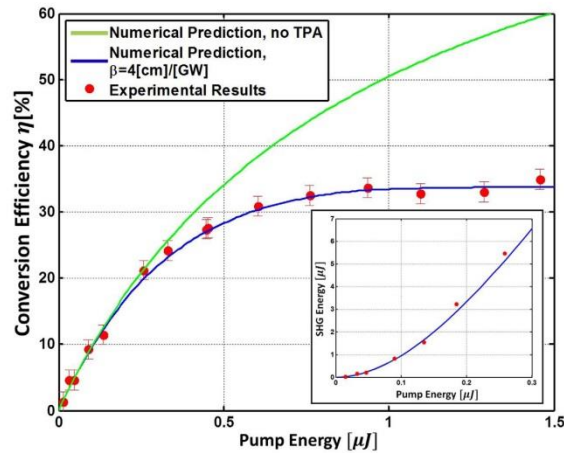
Figure 4. Conversion efficiency as a function of pump energy. Deviation between the loss-free numerical predication and experimental results can be attributed to TPA. Inset: the SHG pulse energy and the pump pulse energy exhibit quadratic dependency in small energy.

the grating, enabled us to change the relative phase between the pulse wavelengths, hence changing its duration between 350 fs to 3.5 ps in the full-bandwidth case, or between 600 fs to 2.6 ps in the truncated-bandwidth case. Measurements of the pump pulse duration were done using frequency resolved optical grating (FROG).

Conversion efficiency measurements were conducted for a large span of pump energies and presented in figure 4. For low pump energies, a good correspondence between numerical prediction and experimental results was achieved, even without taking into account parasitic effects such as TPA. For the strong pump regime, we have examined several mechanisms in order to explain the early saturation in the conversion efficiency curve. We examined through numerical simulation back-conversion of the generated SHG and other nonlinear cascaded effects through TWM, and found that such effects are not occurring in our adiabatic design. Possible degenerate four wave mixing (FWM) interactions were also

6

A Dahan *et al*
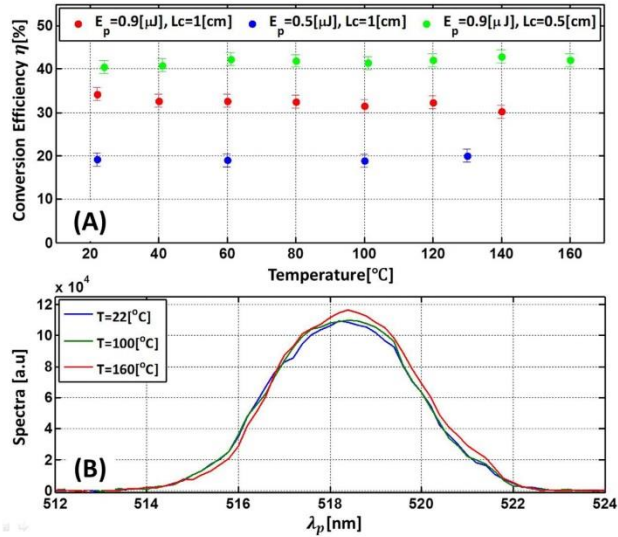
Figure 5. Temperature robustness. (A) Temperature barely affects the conversion efficiency for a very wide span of temperatures. The robustness is not altered with pump energy, as discussed in figure 2(A). Measurements of the conversion efficiency with the crystal cut in half give better results than those obtained with the whole crystal (green dots versus red dots), attributed to shorter possible absorption length. (B) SHG spectra is measured at 0.1 μJ for different temperatures. As seen, the different spectra are hardly affected by temperature.
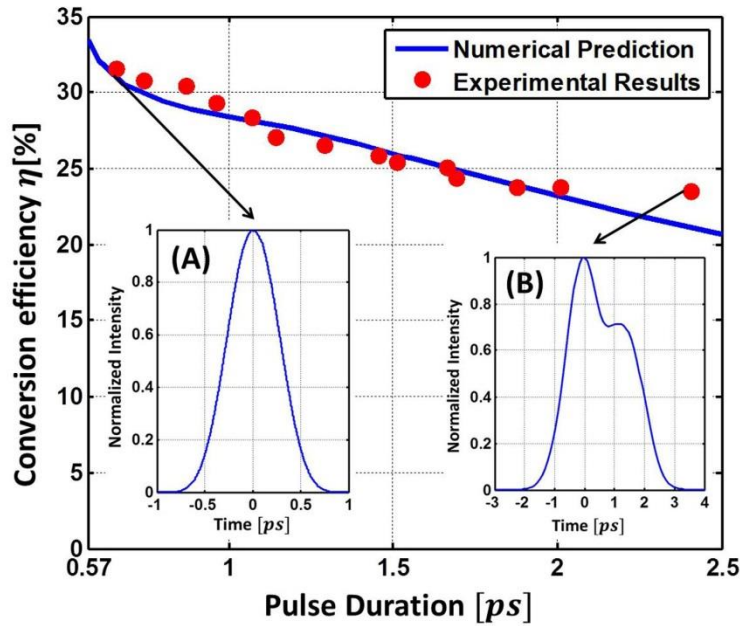
Figure 6. Pulse duration effect on conversion efficiency. Inset (A) FROG measurement of 660 fs pulse duration. Inset (B) FROG measurement of 2.58 ps pulse duration.

7

51

dismissed due to phase mismatch considerations. We inserted the pump pulse into a bulk-KTP and experienced no absorption at all, giving rise to the fact that the generated green is absorbed during propagation along the crystal optical axis, decreasing the measured conversion efficiencies. Assuming that the absorption is attributed to TPA of the generated SHG pulse and incorporating it into the simulation, enabled us to fit the numerical predication to the experimental results at the full nonlinear regime with $\beta = 4(\text{cm GW}^{-1})$, in very good agreement with the nonlinear coefficient measurements of $\beta(532 \text{ nm})$ [32]. Kerr effect included in the simulation had no significant effect. The performance of the adiabatic SHG design has been validated for both the broader spectrum of 20 nm as well as to the 10 nm truncated one.

We also measured the dependence of the conversion efficiency as a function of the temperature of the nonlinear crystal. The results, which are presented in figure 5, exhibit a complete robustness of the designed crystal and experimentally validate the numerical prediction presented in figure 2(A). It is shown that temperature barely affects the adAPKTP performance. The conversion efficiency along with the SHG spectra are indifferent to temperature over a very wide range of more than 100 °C.

In order to examine whether the conversion efficiency is bounded due to TPA as predicted by simulation, the adAPKTP crystal was cut into two, hence decreasing the length in which SHG can be absorbed throughout. The saturation plateau in the conversion efficiency curve was now measured to be in the range of 40%–50%, justifying our assumption.

The effect of stretching the pump pulse on the conversion efficiency was also examined for the truncated bandwidth case. The pump energy was measured to be 0.7 μJ. The pulse durations, defined by 10%–90% knife edge and FROG measurement, varied between 660 fs (figure 6 inset (A)) to 2.58 ps (figure 6 inset (B)). In our measurements we observe that although the intensity density is decreased by $\sim$4, the conversion efficiency did not change dramatically, as could be naively expected when comparing to the CW regime where $\eta \propto I_p$ [27]. The robustness shown in figure 2(B) is experimentally validated. Numerical predication with $\beta = 4(\text{cm GW}^{-1})$ is in agreement with experimental results. Measurements in the full bandwidth case were also conducted, with pump energy of 0.9 μJ, exhibiting a decrease in conversion efficiency from $\eta = 27\%$ to $\eta = 9\%$ as pulse duration increases from 290 fs to 3.23 ps.

5. Conclusions

To conclude, we have experimentally demonstrated a robust and efficient SHG of ultrashort pulses based on adiabatic frequency conversion. We have shown that the conversion from near-IR to visible in a SHG process is not sensitive to the bandwidth of the fundamental pulse and to the temperature of the nonlinear crystal. It was also demonstrated that stretching the pump does not have a critical effect on the conversion process. A time domain simulation for any TWM process was developed, and good correspondence with experimental results has been obtained. The frame work of the simulation enables us to easily incorporate parasitic effects, both in the time or in

the spectral domain, and can be generalized to include high-order nonlinear effects such as FWM for further research on ultrashort frequency conversion. Such an achievement can be useful in the design of extremely stable frequency conversion optical elements, aimed to perform at harsh environmental conditions as adverse temperatures, shocks, tensile stress and external pressure, as well as in fundamental research in second harmonic imaging microscopy and plasmonic nanostructures. Thus, appealing for a wide range of applications in medical procedures, avionics, satellites, and field-deployable communications systems.

Acknowledgments

References

[1] Franken P, Hill A E, Peters C and Weinreich G 1961 Phys. Rev. Lett. **7** 118
[2] Fiebig M, Pavlov V V and Pisarev R V 2005 J. Opt. Soc. Am. B **22** 96–118
[3] Corn R M and Higgins D A 1994 Chem. Rev. **94** 107–25
[4] Helmchen F and Denk W 2005 Nat. Methods **2** 932–40
[5] Campagnola P J and Loew L M 2003 Nat. Biotechnol. **21** 1356–60
[6] Suchowski H, Bruner B D, Arie A and Silberberg Y 2010 Opt. Photon. News **21** 36–41
[7] Boulanger B, Hum D S and Fejer M M 2007 C. R. Phys. **8** 180–98
[8] Suhara T and Nishihara H 1990 IEEE J. Quantum Electron. **26** 1265–76
[9] Arbore M A, Galvanauskas A, Harter D, Chou M H and Fejer M M 1997 Opt. Lett. **22** 1341–3
[10] Lee Y L, Noh Y C, Jung C, Yu T, Ko D K and Lee J 2003 Opt. Express **11** 2813–9
[11] Regelskis K, Želudevičius J, Gavrilin N and Račiukaitis G 2012 Opt. Express **20** 28544–56
[12] Baudrier-Raybaut M, Haidar R, Kupecek P, Lemasson P and Rosencher E 2004 Nature **432** 374–6
[13] Suchowski H, Porat G and Arie A 2014 Laser Photon. Rev. **8** 333–67
[14] Suchowski H, Oron D, Arie A and Silberberg Y 2008 Phys. Rev. A **78** 063821
[15] Baranova N B 1993 J. Exp. Theor. Phys. Lett. **57** 790
[16] Suchowski H, Prabhudesai V, Oron D, Arie A and Silberberg Y 2009 Opt. Express **17** 12731–40
[17] Phillips C R and Fejer M M 2010 Opt. Lett. **35** 3093–5
[18] Phillips C R, Langrock C, Chang D, Lin Y W, Gallmann L and Fejer M M 2013 J. Opt. Soc. Am. B **30** 1551–68
[19] Heese C, Phillips C R, Gallmann L, Fejer M M and Keller U 2010 Opt. Lett. **35** 2340–2
[20] Heese C, Phillips C R, Gallmann L, Fejer M M and Keller U 2012 Opt. Express **20** 18066–71
[21] Heese C, Phillips C R, Mayer B W, Gallmann L, Fejer M M and Keller U 2012 Opt. Express **20** 26888–94
[22] Yaakobi O, Caspani L, Clerici M, Vidal F and Morandotti R 2013 Opt. Express **21** 1623–32
[23] Suchowski H, Krogen P R, Huang S W, Kärtner F X and Moses J 2013 Opt. Express **21** 28892–901
[24] Krogen P, Suchowski H, Liang H, Flemens N, Hong K H, Kärtner F X and Moses J 2017 Nat. Photon. submitted
[25] Porat G and Arie A 2013 J. Opt. Soc. Am. B **30** 1342–51

8

A Dahan *et al*

[26] Leshem A, Meshulam G, Porat G and Arie A 2016 *Opt. Lett.* **41** 1229–32

[27] Boyd R W 2008 *Nonlinear Optics* 3rd edn, ed R W Boyd (Burlington: Academic)

[28] Krogen P R 2014 A novel few-cycle optical source in the mid-infrared *Dissertation* Massachusetts Institute of Technology

[29] Kato K and Takaoka E 2002 *Appl. Opt.* **41** 5040–4

[30] Rosenman G, Skliar A, Oron M and Katz M 1997 *J. Phys. D: Appl. Phys.* **30** 277

[31] Englander A, Lavi R, Katz M, Oron M, Eger D, Lebiush E, Rosenman G and Skliar A 1997 *Opt. Lett.* **22** 1598–9

[32] Maslov V A, Mikhailov V A, Shaunin O P and Shcherbakov I A 1997 *Quantum Electron.* **27** 356

6. Article - Pulse shaping of broadband adiabatic SHG

Optics Letters

Pulse shaping of broadband adiabatic SHG from a Ti-sapphire oscillator

Assaf Levanon,[1] Asaf Dahan,[1] Achiya Nagler,[1] Erga Lifshitz,[1] Eyal Bahar,[1] Michael Mrejen,[1] and Haim Suchowski[1,2,*]

[1]Condensed Matter Physics Department, School of Physics and Astronomy, Tel Aviv University, Tel Aviv 69978, Israel
[2]The Center of Light-Matter Interaction, Tel Aviv University, Tel Aviv 69978, Israel
*Corresponding author: haimsu@post.tau.ac.il

We experimentally demonstrate an efficient broadband second-harmonic generation (SHG) process with a tunable mode-locked Ti:sapphire oscillator. We have achieved a robust broadband and efficient flat conversion of more than 35 nm wavelength by designing an adiabatic aperiodically poled potassium titanyl phosphate crystal. Moreover, we have shown that with such efficient flat conversion, we can shape and control broadband second-harmonic pulses. More specifically, we assign a spectral phase of absolute value and π-step, which allows wavelength tunable intense pump-probe and amplitude modulation of the broadband second-harmonic output. Such spectral phases serve as a proof of concept for other pulse-shaping applications for nonlinear spectroscopy and imaging. © 2017 Optical Society of America

Ultrafast laser sources are at the heart of ultrafast experimental science. In the past two decades, ultrashort pulse laser oscillators and amplifiers have become common equipment in the fundamental scientific exploration, as well as in a handful of industrial applications. Those sources which, by their nature, are broadband and coherent, allow exploring many phenomena that occur at the ultrafast timescale of many scientific processes and dynamical evaluations in nature [1–3]. Due to the extremely high peak power, nonlinear optics in the ultrashort regime results in efficient frequency conversion generation processes and, therefore, is of great interest in a vast number of fields, such as color generation, nonlinear spectroscopy, imaging for metallurgy, photo-induced dynamics, and noninvasive background-free diagnostics [4–6]. As these ultrashort pulses are much faster than any electronic system, many unique methods have been developed to characterize them. These include finding ultrafast pump-probe and interferometric capabilities, allowing femtosecond temporal resolution experiments and ultrafast characterization methods, such as frequency-resolved optical gating (FROG), multiphoton intrapulse

interference phase scan and spectral phase interferometry for direct electric-field reconstruction [1,7–9]. Among the various nonlinear conversion processes, three-wave mixing and, especially, second-harmonic generation (SHG), became widely used. Yet, frequency conversion in the ultrashort regime remained quite complicated, as the conventional conversion devices usually exhibit a tradeoff between the conversion bandwidth and the conversion efficiency, rooted in the phase mismatch between the interacting waves, which usually compensates for only a narrowband of frequencies [10,11].

In the last decade, adiabatic frequency conversion has gained high interest and has been the subject of vast theoretical and experimental research [12–19]. The adiabatic method has overcome the tradeoff between conversion efficiency and bandwidth for sum frequency generation (SFG), difference frequency generation (DFG), and optical parametric amplification (OPA) and, recently, in SHG processes. In the fully nonlinear regime, where all interacting waves considerably change their power, efficient broadband conversion is more difficult due to the complex nonlinear dynamics. In the past few years, there were tremendous theoretical and experimental efforts to reconcile the requirements of the fully nonlinear regime processes and the high efficiency broad-bandwidth frequency conversion using the adiabatically varying design. A comprehensive theory for an adiabatic frequency conversion process of any quasi-CW three waves was developed by Porat and Arie [20] and by Phillips *et al.* [21], later validated by Leshem *et al.* [22] for the case of adiabatic SHG in the nano-second regime. The theoretical generalization and the experimental demonstration of adiabatic SHG for ultrashort pulses, which also take into account dispersion effects and higher-order nonlinear parasitic effects, was later developed by Dahan *et al.* [23], demonstrating an efficient robust frequency doubling for a 75 nm acceptance bandwidth, thermal acceptance of more than 100°C, and chirp variation of 300 fs–3.5 ps, thus displaying an unmatched robustness under both environmental conditions and characteristics of the incoming pulse. However, to satisfy the adiabatic criteria, all of these demonstrations of adiabatic frequency conversion in various nonlinear processes have relied on pump energies requiring amplification.

In this Letter, we experimentally demonstrate that an adiabatic design is capable of extremely robust efficient SHG also at

power levels characteristic of high-repetition-rate femtosecond oscillators. We show that with pulse peak energies of nanojoule regime, one can achieve above 50% of energy conversion efficiencies for 70 fs Ti-sapphire pulses. Furthermore, the flat-top conversion frequency response of the presented design allows us to perform broadband pulse shaping manipulations prior to the nonlinear optical conversion, thus not suffering from the spectral limitation that is conventionally imposed by the limited bandwidth of birefringence or regular periodic crystal designs. More specifically, using a spatial light modulator (SLM) in a 4-f pulse shaper, we present a tunable pump-probe apparatus based on a varying absolute spectral phase profile in the frequency domain. In a similar way, we show that when applying a π-step spectral phase, coherent control of the SHG spectrum can be achieved, imposing a complete dip in the SHG, originating in the complete destructive interference of the second-harmonic field of the fundamental waves [23].

The experimental setup, illustrated in Fig. 1, consists of an 80 MHz repetition rate tunable coherent oscillator between 690 and 1040 nm (Mai-Tai) which served as the pump pulse, delivering 17.5 nm full width half-maximum (FWHM) ~70 fs transform-limited pulses, with energies spanning 10–30 nJ. The pump pulse then passes through JENOPTIK 640D SLM, enabling us to alter the pump pulse spectral phase and temporal shape before it is focused into an adiabatically aperiodically poled potassium titanyl phosphate (adAPKTP) crystal. The residual pump and the generated SHG are separated using a dichroic mirror around 950 nm. The spectrum of the SHG pulse, measured using an Avantes spectrometer, is displayed in the right lower image of Fig. 1, demonstrating efficient conversion over the entire pump-pulse spectrum.

The phase mismatch between the interacting waves is compensated for by using the poling method [10]. In the presented design, the second-order nonlinear susceptibility $\chi(z)$ fluctuates between $+\chi$ and $-\chi$ in batches determined by $\chi(z) = \text{sign}(\cos(K_g(z)z))$, where the grating function $K_g(z)$ is given

by $K_g(z) = (118.2z^3 - 45.2z^2 - 997.9z + 7957.1)[\text{cm}^{-1}]$, and z spans the crystal length $z \in [-0.5\ \text{cm}, 0.5\ \text{cm}]$.

The crystal grating period $\Lambda = 2\pi/K_g(z)$ adiabatically changes from $\Lambda = 7.1\ \mu\text{m}$ to $\Lambda = 8.9\ \mu\text{m}$ along the optical axis of the nonlinear crystal.

In our analysis, we use the three-dimensional generalization of the fully nonlinear dynamical equations, which dictates the nonlinear conversion of any three-wave mixing and, in particular, the depleted ultrashort SHG case [23]. Two-photon absorption (TPA) of the fundamental pump and the generated SHG was also taken into account as in the case of Ref. [23], likewise found to be of great importance. Since the SHG process occurred within the Rayleigh range of the pump pulse, spatial diffraction has been neglected, eliminating the interaction between different areas of the transverse intensity profile.

The following three-dimensional generalization of the SHG [Eqs. (1) and (2)], is applied for predicting the SHG process behavior:

$$\frac{\partial B_{\text{SHG}}(r,z,t)}{\partial z} + i\mathcal{F}^{-1}(\beta(\omega + \omega_{\text{SHG}})B_{\text{SHG}}(r,z,\omega))$$
$$= -i\chi(z)\mathcal{F}^{-1}\left(\frac{\omega + \omega_{\text{SHG}}}{n(\omega + \omega_{\text{SHG}})c}\mathcal{F}(B_p^2(r,z,t))\right)$$
$$- \frac{\beta}{2}I_{\text{SHG}}(r,z,t)B_{\text{SHG}}(r,z,t), \tag{1}$$

$$\frac{\partial B_p(r,z,t)}{\partial z} + i\mathcal{F}^{-1}(\beta(\omega + \omega_p)B_p(r,z,\omega))$$
$$= -i\chi(z)\mathcal{F}^{-1}\left(\frac{\omega + \omega_p}{n(\omega + \omega_p)c}\mathcal{F}(B_{\text{SHG}}(r,z,t)B_p^*(r,z,t))\right), \tag{2}$$

where $B_{\text{SHG}}(r,z,\omega)$, $B_p(r,z,\omega)$ are the electric field spectral density amplitudes of the pulses, $B_{\text{SHG}}(r,z,t)$ and $B_p(r,z,t)$ are the electric field modulation around the pulses central frequencies, and $\beta(\omega)$ is the dispersion relation. All physical variables in Eqs. (1) and (2) are carefully defined in Ref. [23].

Incorporation of the measured FROG pump pulse and the measured 40 μm FWHM Gaussian beam profile into the simulations yields great agreement with the experimental results for $\beta = 4[\frac{\text{cm}}{\text{GW}}]$, the TPA coefficient, in correspondence with the nonlinear coefficient obtained in Refs. [23,24].

The energy conversion efficiency of the crystal is the ratio between the generated SHG pulse energy to the pump pulse energy:

$$\eta = \frac{E_{\text{SHG}}(z_{\text{out}})}{E_p(z_{\text{in}})}, \tag{3}$$

where z_{out} and z_{in} are the locations of the crystal output and input facets, respectively. The conversion efficiency measurements as a function of the central pump wavelength are presented as red dots in Fig. 2(a). Although conversion efficiency measurements were limited in the range of 970–1030 nm due to source limitations, the adiabatic design is capable of an efficient frequency doubling within a bandwidth of 80 nm, shown as blue solid line.

Next, we have added a broadband 4-f pulse shaper based on computer-controlled SLM positioned at its Fourier plane. First, by varying the spectral quadratic phase [25], we have used it as an aligned tunable compressor that can control the group delay dispersion of the fundamental, which also influences SHG output spectral distribution. The architecture for the 4-f pulse
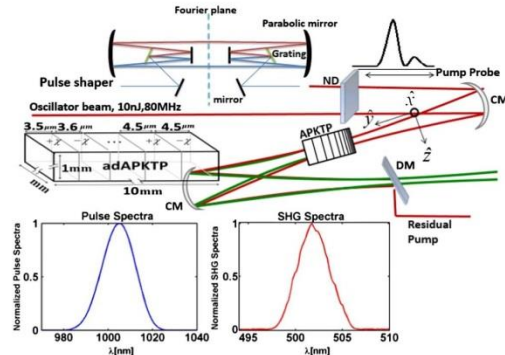
Fig. 1. Adiabatic SHG experimental apparatus. The programmable 4-f of the quadratic phase tunable pulse shaper is composed of a pair of diffraction gratings with 600 lines/mm and a pair of parabolic curved mirrors. Two-dimensional SLM was placed at the Fourier plane and was used as a dynamic filter for spectral phases. ND, neutral density filter; CM, curved mirror; DM, dichroic mirror; adAPKTP, adiabatically aperiodically poled KTP. Left lower inset—the measured pump normalized spectra. Right lower inset—the measured SHG normalized spectra.
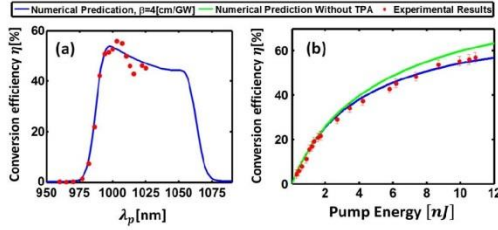
Fig. 2. Conversion efficiency as a function of (a) pump central wavelength and (b) pump energy. The blue curve is the conversion efficiency predicted by our numerical simulations with the addition of TPA. (a) Conversion efficiency dependence with a pump central wavelength. (b) Conversion efficiency as a function of pump energy centered at a 1005 nm wavelength. The deviation between the loss-free numerical prediction (green curve) and the experimental results (red dots) is attributed to TPA (blue curve).

shaper includes two pieces of 600 grooves/mm ruled grating which disperse the light angularity into a telescope, based on a pair of curved 913.4 mm parabolic mirrors, which fits a 4-f arrangement in a chirped pulse amplification system.

The pump-probe apparatus is implemented by applying an absolute-valued spectral phase centered within the bandwidth of the fundamental spectral phase, denoted by ω_{Abs}, i.e., $\phi \propto |\omega - \omega_{Abs}|$. Determined by the sign of the linear phase slope, different parts of the pump spectrum shifted in opposite directions in the time domain, therefore enabling splitting the incoming pump pulse into two localized pump pulses, with an extinction ratio and delay determined by ω_{Abs} and the absolute phase slope. The idler's spectrum dependence with $\lambda_{Abs} = \frac{2\pi c}{\omega_{Abs}}$ is presented in Fig. 3 for an input hyperbolic secant pump pulse centered on 1005 nm. When applying the absolute-valued shape spectral phase in the center of the pump pulse $\lambda_{Abs} = 1005$ nm, as shown in Fig. 3(a-I), the initial pump pulse splits into two pulses with the same peak intensity, resulting in a symmetrical normalized pump probe SHG spectra. When the absolute-valued shape phase is not symmetrical with respect to the pump central frequency, as shown in Fig. 3(a-II), the generated asymmetrical pump pulses result in asymmetrical SHG spectra.

We proceed by applying a π-step spectral phase. As a result of destructive interference between the different frequency components, the π-step induces SHG/SFG pulses with spectral dips at different wavelengths. It is worth noting that due to the mathematical similarity between the perturbative solution of a TPA process in a non-resonant two-level quantum system and the instantaneous SHG process (where time scaling t is replaced by z, the propagation length in crystal), most of the coherent control schemes that were applied in atomic physics can be adopted to a pulse-shaped SHG using the ASHG non-linear crystal. In order to demonstrate the shaping of the SHG spectra, we have also applied a π-step function at different locations on the pump spectral phase.

We consider the case of second-harmonic generation of ultrashort pulse with an electric field distribution of $\varepsilon(t)$. From second-order non-resonant time-dependent perturbation theory, the instantaneous second-harmonic spectral field can be
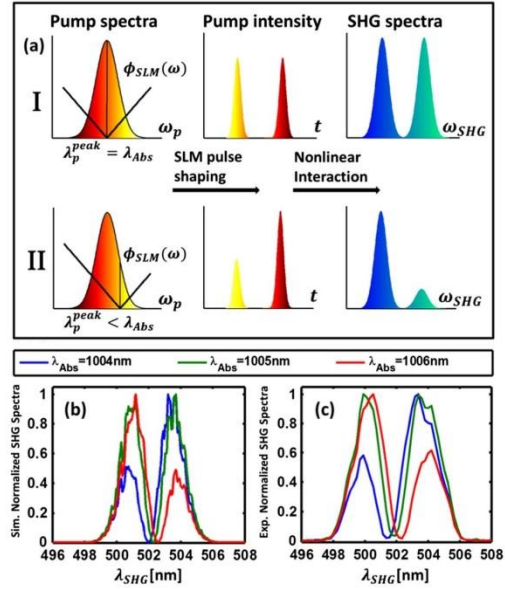
Fig. 3. Absolute phase effects on the SHG pulse for different ω_{Abs}, the central absolute phase frequency. (a) Illustration of absolute phase concept. (b) Simulated normalized SHG spectra. (c) Experimental normalized SHG spectra.

found by the autoconvolution of the fundamental spectral field $\tilde{\varepsilon}(\Omega) = F.T\{\varepsilon(t)\}$ [10], which is described by

$$\varepsilon_{SHG}(\omega_0) = \left| \int_{-\infty}^{\infty} \epsilon^2(t) \cdot \exp(i\omega_0 t)\mathrm{d}t \right|^2$$
$$= \left| \int_{-\infty}^{\infty} \tilde{\varepsilon}(\Omega)\tilde{\varepsilon}(\omega_0 - \Omega)\mathrm{d}\Omega \right|^2, \quad (4)$$

where ω_0 is the SHG frequency.

If we perform change of variables as $\Omega \rightarrow \Omega + \frac{\omega_0}{2}$, and write explicitly $\tilde{\varepsilon}(\Omega) = A(\Omega)\exp[i\Phi(\Omega)]$, we obtain Eq. (5):

$$\varepsilon_{SHG}(\omega_0) = \left| \int_{-\infty}^{\infty} A\left(\frac{\omega_0}{2} + \Omega\right) A\left(\frac{\omega_0}{2} - \Omega\right) \right.$$
$$\left. \cdot \exp\left[i\left\{ \Phi\left(\frac{\omega_0}{2} + \Omega\right) + \Phi\left(\frac{\omega_0}{2} - \Omega\right) \right\} \right]\mathrm{d}\Omega \right|^2, \quad (5)$$

where $A(\omega)$ and $\Phi(\omega)$ are the spectral amplitude and spectral phase, respectively.

The equation reflects that the SHG/SFG occurs for all pairs of photons with frequencies which add up to ω_0 and lie within the spectrum of the exciting pulse. It is easy to see that when the phase cancels (i.e., $\Phi(\frac{\omega_0}{2} + \Omega) + \Phi(\frac{\omega_0}{2} - \Omega) = 0$) and, for a symmetric amplitude $A(\omega)$ with respect to $\frac{\omega_0}{2}$, the amount of SHG is maximized. This is in agreement with the finding of Meshulach and Silberberg [25,26], where they showed that an anti-symmetrical spectral phase can result in the same TPA rate as transform-limited excitation. The same behavior happens for the instantaneous SHG/SFG case, where the
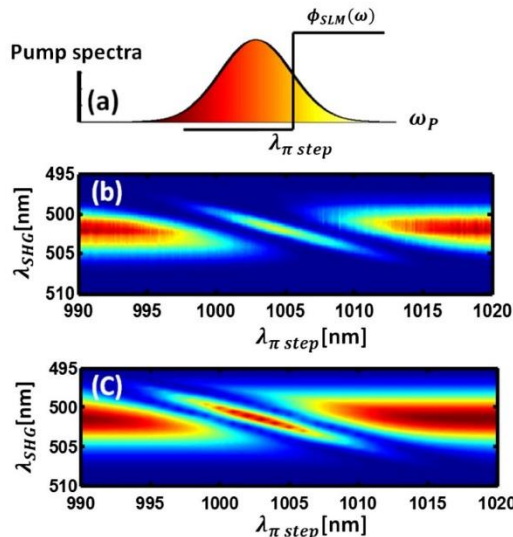
Fig. 4. ASHG conversion in KTP crystal excited by a pulse with a spectral phase of π-step, as a function of the step position. (a) Illustration of SLM-induced π-step phase centered at $\lambda_{\pi\,\text{step}}$. (b) Experimental results. (c) Simulation results. The simulation results were obtained by inserting the measured spectrum of the original pulse.

transform-limited pulse ($\Phi(\Omega) = 0$), and every anti-symmetric phase with respect to $\frac{\omega_0}{2}$, result in the same SHG generation. Therefore, the anti-symmetric phase can significantly affect the shape of the pulse to have much smaller amplitude and a much longer duration, it does not affect the SHG [24].

Our experimental results of applying an anti-symmetric π-step phase each time at a different wavelength show different SHG/SFG spectra for each measurement. As expected, this destructive interference appears in the SHG/SFG if the step is not in the middle of the spectrum, and could even lead to complete destructive interference of the SHG/SFG signal at a specific wavelength. In Fig. 4, we show the experimental results, as well as the simulations of broadband ASHG conversion as a function of the π-step position. The simulation results were obtained by inserting the measured spectrum of the original pulse. Very good agreement is obtained between the experimental results and the numerical simulations.

To conclude, we experimentally investigate the performance of an adiabatic aperiodically poled KTP crystal using a conventional femtosecond high-repetition-rate oscillator in the nanojoule energy regime. We show that efficient wideband ultrashort second-harmonic generation is feasible in a single crystal, experimentally demonstrating an acceptance bandwidth bigger than 40 nm with nanojoule level excitation. Furthermore, we show that the broadband operation of the adiabatic crystal design enables us to perform pulse shaping manipulations on the fundamental pulses. An SLM-dependent tunable pump probe was given as an example, where altering the pump probe spectral and temporal characteristics is possible without the need of realigning the experimental apparatus.

Based on the broad spectral conversion response of the ASHG nonlinear crystal. We show that the SHG/SFG spectrum can be manipulated by tailoring the shape of the exciting ultrashort pulse. In particular, we investigate the effect of a spectral phase modulation of absolute value and a π-step spectral phase. We show that spectral shaping, as well as complete destructive interference in the SHG can be achieved. In addition, we show that certain π-step spectral phase modulation, which leads to long pulses, induces SHG as effective as transform-limited pulses. The basic principles presented here open a wide new area for theoretical and experimental work, as well as possible applications in nonlinear spectroscopy and in atomic and molecular physics.

REFERENCES

1. J.-C. Diels and W. Rudolph, *Ultrashort Laser Pulse Phenomena: Fundamentals, Techniques, and Applications on a Femtosecond Time Scale*, 2nd ed. (Academic, 2006).
2. H. A. Zewail, Angew. Chem. (Int. Ed.) **39**, 2586 (2000).
3. A. M. Weiner, *Ultrafast Optics* (Wiley, 2008).
4. L. A. Cavalieri, N. Müller, T. Uphues, V. S. Yakovlev, A. Baltus Caronka, B. Horvath, B. Schmidt, L. Blümel, R. Holzwarth, S. Hendel, M. Drescher, U. Kleineberg, P. M. Echenique, R. Kienberger, F. Krausz, and U. Heinzmann, Nature **449**, 1029 (2007).
5. A. V. Kimel, A. Kirilyuk, P. A. Usachev, R. V. Pisarev, A. M. Balbashov, and T. Rasing, Nature **435**, 655 (2005).
6. N. Dudovich, D. Oron, and Y. Silberberg, Ann. Rev. Phys. Chem. **60**, 277 (2009).
7. R. Trebino, *Frequency-Resolved Optical Gating: The Measurement of Ultrashort Laser Pulses* (Springer, 2012).
8. V. V. Lozovoy, I. Pastirk, and M. Dantus, Opt. Lett. **29**, 775 (2004).
9. C. Iaconis and I. A. Walmsley, Opt. Lett. **23**, 792 (1998).
10. R. W. Boyd, *Nonlinear Optics*, 3rd ed. (Academic, 2011).
11. H. Suchowski, B. Bruner, A. Arie, and Y. Silberberg, Opt. Photon. News **21**(10), 36 (2010).
12. H. Suchowski, G. Porat, and A. Arie, Laser Photon. Rev. **8**, 333 (2014).
13. C. Heese, C. R. Phillips, B. W. Mayer, L. Gallmann, M. M. Fejer, and U. Keller, Opt. Express **20**, 26888 (2012).
14. H. Suchowski, V. Prabhudesai, D. Oron, A. Arie, and Y. Silberberg, Opt. Express **17**, 12731 (2009).
15. C. Heese, C. R. Phillips, L. Gallmann, M. M. Fejer, and U. Keller, Opt. Lett. **35**, 2340 (2010).
16. C. Heese, C. R. Phillips, L. Gallmann, M. M. Fejer, and U. Keller, Opt. Express **20**, 18066 (2012).
17. O. Yaakobi, L. Caspani, M. Clerici, F. Vidal, and R. Morandotti, Opt. Express **21**, 1623 (2013).
18. H. Suchowski, P. R. Krogen, S. W. Huang, F. X. Kartner, and J. Moses, Opt. Express **21**, 28892 (2013).
19. P. Krogen, H. Suchowski, H. Liang, N. Flemens, K.-H. Hong, F. X. Kärtner, and J. Moses, Nat. Photonics **11**, 222 (2017).
20. G. Porat and A. Arie, J. Opt. Soc. Am. B **30**, 1342 (2013).
21. C. R. Phillips, C. Langrock, D. Chang, Y. W. Lin, L. Gallmann, and M. M. Fejer, J. Opt. Soc. Am. B **30**, 1551 (2013).
22. A. Leshem, G. Meshulam, G. Porat, and A. Arie, Opt. Lett. **41**, 1229 (2016).
23. A. Dahan, A. Levanon, M. Katz, and H. Suchowski, J. Phys. **29**, 84004 (2017).
24. V. A. Maslov, V. A. Mikhailov, O. P. Shaunin, and I. A. Shcherbakov, Quantum Electron. **27**, 356 (1997).
25. D. Meshulach and Y. Silberberg, Nature **396**, 239 (1998).
26. D. Meshulach and Y. Silberberg, Phys. Rev. A **60**, 1287 (1999).

7. Difference frequency generation mid-IR pulse compression

The mid – IR regime is of great importance in many scientific areas as chemistry, materials science biology and condensed matter physics, as it covers many of the vibrational absorption bands of molecules. The spectroscopic optical methods in the MIR enable us to capture the material "fingerprints" through its absorption, transmission spectra and phase distortions, thus providing us with an effective mechanism to determine the local structure and dynamics of individual molecule. By providing a broadband- ultrafast source, one can also account to the femtosecond time dynamics of molecules conformational changes, necessary for femto-chemistry experiments. Broadband ultrashort MIR source is also desired for attosecond pulse generation, as the number of harmonics generated in the strong field regime scales with λ.

As broadband sources in the MIR are lacking, frequency conversions are used in order to create such sources. In the following, we examine the generation of a MIR pulse through conversion between a broadband Ti-Sappire oscillator pulse and a strong pump. Using the simulation developed in the previous sections, a robust optical scheme for the generation of an ultrashort MIR pulse is presented.

The compression scheme contains Spatial Light Modulator (SLM), diffractive element and an adiabatic crystal, and the conversion is between the output of a Ti-Sappire oscillator, spanning between 600nm to 1000nm and a narrowband pump pulse around 1032nm.

The problem was to find the optimal parameters for the compression scheme, which includes the pulses time durations, the pump pulse bandwidth, the SLM phase, the distances the pulses goes through the air before the nonlinear crystal, and the dispersive element length and material, to obtain both efficient conversion all along the signal spectra as well as SLM phase requirements well within its operational limitations. The optical scheme is plotted herein:
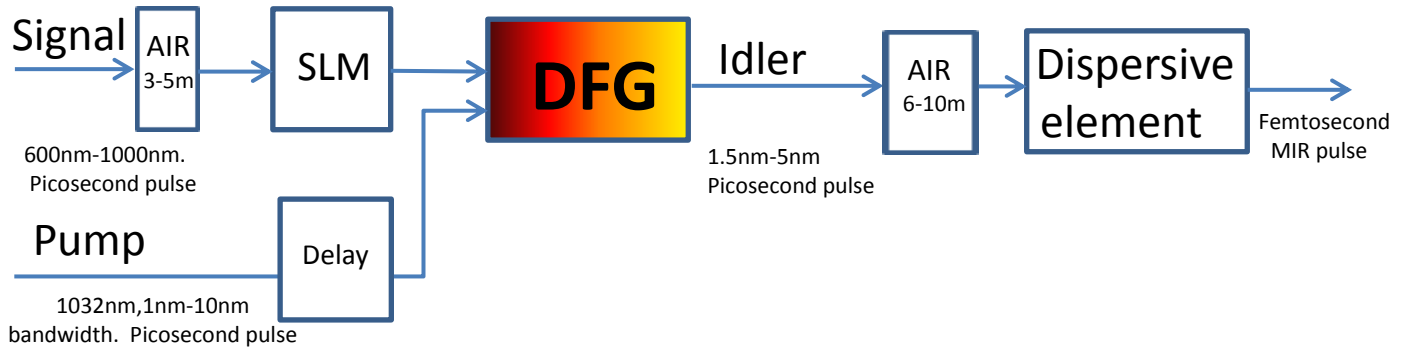
Figure 25. MIR pulse generation and compression scheme.

The compression scheme is based on the fact that when the pump spectral bandwidth is much smaller than the signal pump spectra, the generated DFG pulse phase is linear with the signal pulse phase. By assigning $\tilde{A}_p(z,\omega) = \tilde{A}_p(z)\delta(\omega - \omega_p)$ to Eq. set (3.13) one obtains:

$$(7.1)\ \partial_z \tilde{A}_i(z,\omega) + i\beta(\omega)\tilde{A}_i(z,\omega) = -i\frac{\omega}{c}\frac{\chi(z)}{n(\omega)}\tilde{A}_s(z,\omega) * \tilde{A}_p^*(z,-\omega) =$$

$$= -i\frac{\omega}{c}\frac{\chi(z)\tilde{A}_p^*(z)}{n(\omega)}\tilde{A}_s(z,\omega+\omega_p)$$

It is therefore clear that by adding the incoming signal pulse phase the opposite of the generated idler phase, using the SLM, one can obtain a MIR pulse with no phase difference between its spectral components, that is to say transform limited pulse. Due to damage threshold limitations, we wish the MIR pulse to be compressed not inside the adiabatic crystal but rather inside some simple diffractive element (silicone in our case). The MIR pulse phase added to the signal pulse was therefore calculated after the propagation inside the silicone.

      The simulation parameters are the following:

Simulation Parameters	Simulation Value
Pump Pulse Central Wavelength $\lambda_p[nm]$ (Gaussian Pulse)	1032
Pump Pulse Time Domain FWHM $\Delta\tau^p{}_{FWHM}[ps]$	Positively chirped – Detailed value will be determined in the following
Pump pulse FWHM $\Delta\lambda_{FWHM}[nm]$	1-8
Pump Pulse Energy $E_p[uJ]$	20
Signal Pulse Spectra	Spectral measurements, plotted below
Signal Pulse Time Domain FWHM $\Delta\tau^s{}_{FWHM}[ps]$	Detailed value will be determined in the following
Signal Pulse Energy $E_s[uJ]$	1
Effective Diameter $[um]$	150
Nonlinear Susceptibility $\chi(z)\left[\dfrac{pm}{V}\right]$	27
Crystal Length $[mm]$	20
Crystal Material	Mgcln5
Crystal Grating Function $\left[\dfrac{1}{cm}\right]$	$K_g(z_{cm}) = \left(3569 - 714z_{cm} + 156z_{cm}^2\right)$
Dispersive element	Silicone. The length will be determined in the following

The input simulated Ti-Sappire oscillator spectra is the experimentally measured venteon laser spectra:

Normalized signal intensity
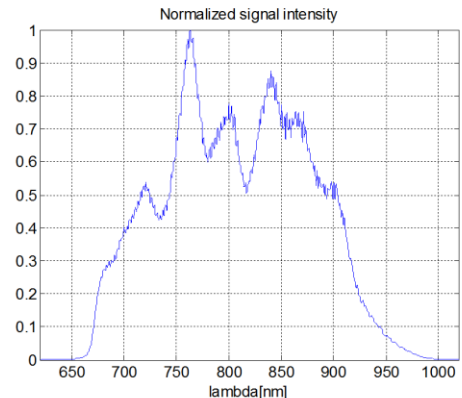
7.1 Conversion efficiency dependence with pulses durations

Before Examining the compression scheme we wish to find what is the best combination of signal and pump pulses durations such that efficient frequency conversion is achieved all over the signal spectra.

We define $(7.2)\,\eta(\lambda)=1-\dfrac{P_s(z_f,\lambda)}{P_s(z_i,\lambda)}$, where $P_s(z,\lambda)$ is the signal spectra as function of the crystal optical axis. The next quantities are defined: $(7.3)\,\eta_{Mean}=mean(\eta(\lambda))$, and $(7.4)\,\sigma_\eta=std(\eta(\lambda))$.

η_{Mean} is a measure for the conversion efficiency, while σ_η is a measure of the effectiveness of the conversion efficiency all along the signal wavelengths.

For a pump pulse bandwidth of 1nm, the following graphs are obtained:
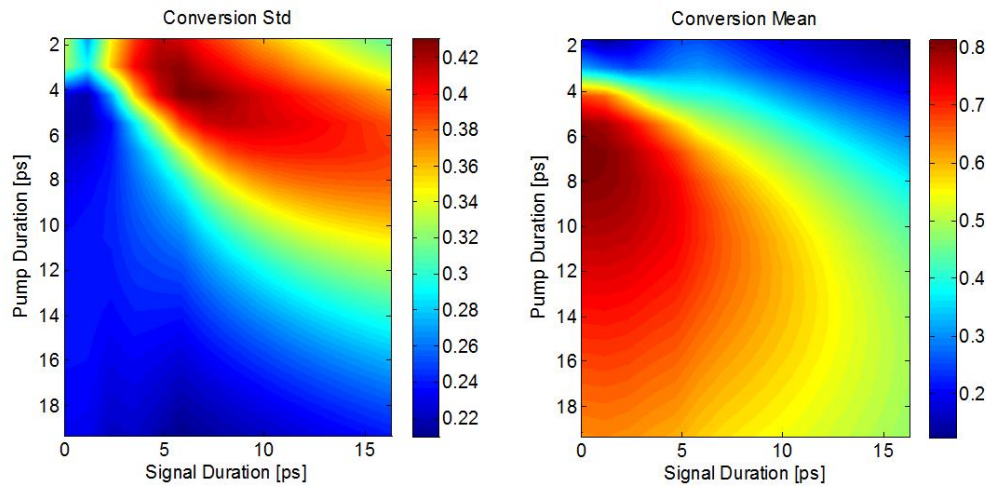
Figure 26.The DFG average conversion efficiency η_{Mean} **and conversion efficiency variance** σ_η **as function of the pulses time durations, for a pump pulse bandwidth of 1nm.**

For a pump pulse bandwidth of 8nm, the following graphs are obtained:
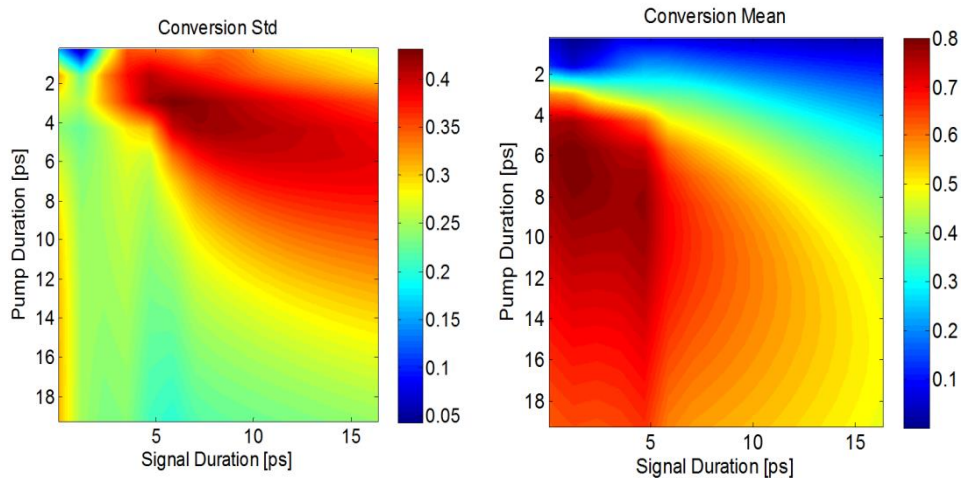
Figure 27. The DFG average conversion efficiency η_{Mean} **and conversion efficiency variance** σ_η **as function of the pulses time durations, for a pump pulse bandwidth of 8nm.**

60

One can conclude from the previous graphs, that both conversion efficiency as well as its robustness all along the signal spectra is dictated by the pump and signal pulse durations and is insensitive to the pump spectral bandwidth. The pulses time durations for optimal **conversion** are obtained:

- Pump pulse duration shall be between 6ps-8ps.
- Signal pulse duration shall be smaller than 2ps.

All pump pulse durations are defined using (10%-90%) knife edge method, namely the pulse duration between 10% to 90% of the pulse cumulative energy distribution function:

$$f(t) = \left(\int_{-\infty}^{t} |A(\tau)|^2 \, d\tau \right) / \left(\int_{-\infty}^{+\infty} |A(\tau)|^2 \, d\tau \right)$$

which for a Gaussian pulse results in $\tau_{(10\%-90\%)} = 1.0871 \, \tau_{FWHM}$.

As displayed, conversion efficiency is maximal when the pump pulse duration is between 6ps-8ps. Hence in following simulations, the simulated (10%-90%) pump pulse duration was taken to be 7ps.

7.2. Compression feasibility dependence with signal chirp

While efficient conversion demands very short signal pulses (<2ps), it was not a priori clear that compression is feasible with such pulses. In the following we examined the compression feasibility for different signal chirps, spanning between $C_s = -5 \cdot 10^{-27} [s^2]$ to $C_s = +5 \cdot 10^{-27} [s^2]$, where

$$\phi_s(\omega) = C_s \left(\omega - \omega_p^{signal} \right)^2, \text{ and } \lambda_p^{signal} = 763 [nm].$$

For every given signal chirp, air propagation length before the nonlinear crystal and air propagation length after the nonlinear crystal, we calculated the total phase that needed to be compensated by the SLM for various lengths of the silicone element. A measure for the total phase needed to be compensated by the SLM is the following:

$$(7.5) \; SLM_{compensation} = \max \left(\sphericalangle Idler \, Phase \right)_{1.8\,\mu m < \lambda_i < 5.5\,\mu m} - \min \left(\sphericalangle Idler \, Phase \right)_{1.8\,\mu m < \lambda_i < 5.5\,\mu m}$$

We observed that the total phase defined above is minimal for specific silicone lengths, which enabled us to examine the compression scheme only for a discrete set of lengths, which we denoted as $\{ L_{opt} \}$.

The $SLM_{compensation}$ at the specific set of silicone lengths $\{ L_{opt} \}$ is denoted as

$$(7.6) \; \Phi_{opt} = SLM_{compensation} \left(L_{opt} \right)$$

Numerical trial and error examinations show that good SLM compensation can be done whenever

$$\Phi_{opt} \leq 350[\text{Rad}]$$
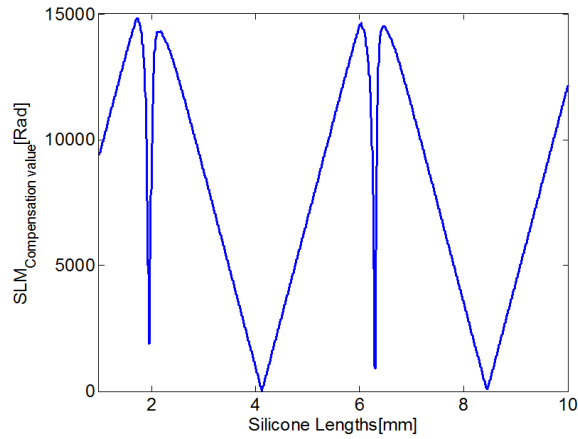
Figure 28. SLM compensation phase as function of the silicone length.

For every signal chirp and calculated silicone length, the SLM phase was calculated, interpolated to 640 values, and inserted again into the simulation, yielding a compressed pulse with phase we seek to be flat. We measured the phase difference by Delta SLM:

$$(7.7)\, Delta_{SLM} = \max(\sphericalangle \text{idler}_{Compressed}) - \min(\sphericalangle \text{idler}_{Compressed})$$

In appendix D section ([10.4.1)](#), we present the simulated Φ_{opt} defined in Eq. (7.6) for various values of signal chirp, and for a span of air lengths before and after the nonlinear crystal. Observing the tables in the appendix, several conclusions are deduced:

- It is easier to compress the MIR pulse in the regime $C_s \in [-4 \cdot 10^{-27} \quad 1 \cdot 10^{-27}][s^2]$.
- For a given air propagation lengths, the shorter the crystal the compensation is better (less phase to compensate).
- The transform limit case is not inferior in terms of compensation vs. other signal chirps.

7.3. Signal conversion efficiency dependence with signal chirp, after SLM compensation

We would like to understand what the desired signal chirp in terms of efficiency is, after being compensated by the SLM.

The quantities $(7.8)\,\eta_E = \dfrac{E_{Idler}(z_f)}{E_{Signal}(z_i)}$, and $(7.9)\,\sigma_\eta = std(\eta(\lambda))$ are presented for the different

scenarios. η_E measures the frequency conversion efficiency, and σ_η is a measure to the conversion efficiency wavelength dependence.

In appendix D section ([10.4.2](#)), we present the simulated efficiencies η_E and σ_η for various values of signal chirp, and for a span of air lengths before and after the nonlinear crystal. Observing the tables in the appendix, several conclusions are deduced:

7.4. Transform limited examination

After being convinced that the transform limited case is not inferior to the chirped case, we examined the transform limited case thoroughly. The examination is detailed in appendix D section ([10.4.3](#)).

Several conclusions can be deduced from the examination:

- In terms of both conversion efficiency and compensation quality we wish the crystal length to be ~ 10mm
- The longer the signal goes through the air, conversion efficiency fluctuation is smaller $\sigma_\eta = std(\eta(\lambda))$.
- The following useful formula is deduced:
- $(7.9)\; L_{crystal}{}^{n,m} \approx 7.76 + 4.31\cdot n + 5.68\left(L_{air}{}^{before}[m]-3\right)m - 0.795\left(L_{air}{}^{after}[m]-6\right)[mm]$

  where n,m are discrete numbers.
- Buying 16mm of silicone allows a robust compression scheme for every propagation distance before the nonlinear crystal in the range of 3-4m, and with propagation distance after the nonlinear crystal in the range 6-10m

7.5 Efficient MIR pulse compression – conclusions

In the previous sections we investigate the optimal scheme for both efficient and robust generation of transform limited pulse. We arrive at the following conclusions:

- Pump temporal width (FWHM) shall be around 7ps.
- The signal transform limited case is not inferior to other chirped signal pulses, in terms of both compression feasibility and conversion efficiency.
- While many solutions exist, all obeying Eq. (7.9), not all solutions exhibit good conversion efficiency curve. If we buy 16mm of silicone, for every propagation distance before the nonlinear crystal, fine solution for the compression scheme exist with propagation distance after the nonlinear crystal in the range 6-10m. The expected energy conversion efficiency is between 25% to 15%.

The simulated generated compressed transform limited MIR pulse is presented:
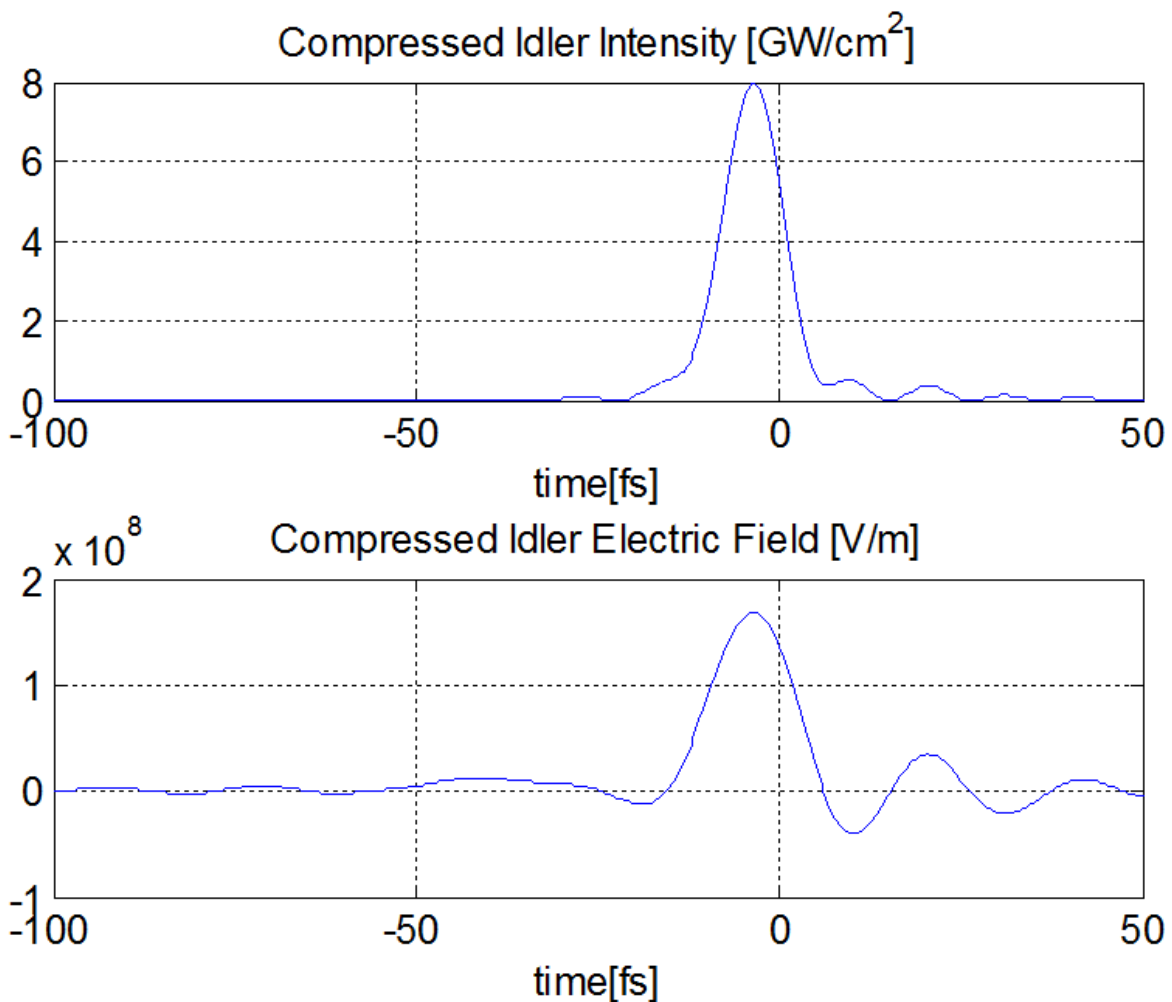
Figure 29. Compressed generated MIR pulse.

8. Adiabatic four-wave mixing frequency conversions

In recent years, much effort has been invested in developing schemes to efficiently convert broader and broader optical spectra. Yet the common paradigm of nonlinear frequency conversion with constant phase-matching includes a restrictive tradeoff between the conversion efficiency and its bandwidth.

The adiabatic frequency conversion concept, exhibited in the previous chapters, offered the ability to sidestep efficiency-bandwidth trade-offs in nonlinear frequency conversion. The adiabatic character of the conversion both dramatically increases the available bandwidth in these applications while also ensuring high conversion efficiency. Application of this concept to three-wave mixing in aperiodically poled quasi-phase-matched media, allowed the generation of phase and amplitude-controlled, octave-spanning, coherent mid-IR light sources by means of adiabatic TWM processes. Moreover, as presented in section ([6](#)), the amplitude and phase transferring qualities of adiabatic frequency conversion allowed amplitude and phase tunability by pulse shaping prior to conversion, allowing great flexibility for spectroscopic applications.

Though very promising, the traditional platforms for frequency conversion using TWM, such as SFG, DFG, optical parametric amplification (OPA), and optical parametric oscillation (OPO), are limited to devices based on specialized materials engineered and grown specifically for the application, whether for ultrashort pulses or for single-frequency sources. In contrast, the ubiquitous presence of cubic optical nonlinearities means that all devices employing light propagation have the capacity for frequency conversion. Examples include optical amplifiers used for telecommunications, silicon and other semiconductor waveguides used for photonics applications, and gas filled capillaries used for spectral broadening of ultrashort pulses. In each of these technologies, four-wave mixing frequency conversion (FWMFC) has been employed [31] [32] [33] [34], and four-wave mixing frequency converters have appeared in other settings, such as highly nonlinear and photonic crystal fibers [35] [36]. Like all nonlinear frequency conversion, application of four-wave mixing to the generation of broadband light sources are limited in bandwidth, and are further limited by a trade-off between efficiency and bandwidth.

In the following, we introduce the concept of adiabatic frequency conversion for four-wave mixing, which we find broadly applicable to numerous χ_3 nonlinear platforms. First, we present a general propagation equation for four-wave mixing derived from Maxwell's equations, capturing the full frequency and time domain nonlinear pulse propagation effects for wave-guided interactions. Later on, we present that the obtained equations can be simplified in several conditions to reveal the SU(2) symmetry in FWM, which leads to an analogy with rapid adiabatic passage in two-level atomic systems.

8.1 Pulsed four wave mixing wave- guided interactions

We describe the time dependent evolution of Four Wave Mixing in dielectrical waveguides via third order susceptibility. We assume that only one waveguide mode is excited.

$$(8.1)\, \vec{E}_t = \int_{-\infty}^{+\infty} \frac{d\omega}{2\pi} \underbrace{\frac{1}{2}\left(A(z,\omega) + A^*(z,-\omega) \right)\vec{E}_t(x,y,\omega)e^{-i\beta(z,\omega)z}}_{\bar{E}(z,\omega)}\, e^{i\omega t}$$

where $A(z,\omega)$ is the spectral density of the electric field amplitude, $\beta(\omega) = \dfrac{\omega n(\omega)}{c}$ is the frequency dependent electric field wavenumber, and $\vec{E}_t(x,y,\omega)$ obeys Helmholtz Eq. (3.2). The subscript t in the electric field written above denotes the electric field transverse dimension, perpendicular to the optical axis.

Detailed derivation of the equations dictating the FWM frequency conversion process is presented in appendix E. We summarize the derivation herein:

- $A_\beta(z,\omega)$ is the spectral density of a pulse centered around ω_β, where $\beta \in [1,2,3,4]$ and the pulses central frequencies obey $\omega_1 + \omega_2 = \omega_3 + \omega_4$.

- We assume that the electric field profile merely changes within the spectral envelope of the pulses. In order words:

$$\vec{E}(\vec{r},\omega)e^{-i\beta(z,\omega)z}\left(A_\alpha(z,\omega) + A_\alpha^*(z,-\omega) \right) \approx \vec{E}(\vec{r},\omega_\alpha)e^{-i\beta(z,\omega)z}\left(A_\alpha(z,\omega) + A_\alpha^*(z,-\omega) \right)$$

- We define the amplitudes C_β and B_β

$$(8.2)\, C_\beta(z,\omega-\omega_\beta) = B_\beta(z,\omega) = A_\beta(z,\omega)e^{-i\beta(z,\omega)}$$

  where $\beta \in [1,2,3,4]$.

- $C_\beta(z,t)$ is the Fourier transform of the electric field spectral density envelope centered at ω_β:

$$(8.3)\, C_\beta(z,t) = \int_0^{+\infty} \frac{d\omega}{2\pi} e^{i(\omega-\omega_\beta)t} C_\beta(z,\omega-\omega_\beta) = \Im\left(C_\beta(z,\omega-\omega_\beta) \right)$$

- We define the following overlap integrals:

$$(8.4)\, \gamma_{Int} = \frac{1}{2}\iint dxdy \left(\vec{E}_3 \cdot \vec{E}_4 \vec{E}_2 \cdot \vec{E}_1 + \vec{E}_3 \cdot \vec{E}_2 \vec{E}_4 \cdot \vec{E}_1 + \vec{E}_4 \cdot \vec{E}_2 \vec{E}_3 \cdot \vec{E}_1 \right)$$

$$(8.5)\, \mu_{i,j} = \mu_{j,i} = \frac{1}{2}\iint dxdy \left(|\vec{E}_i|^2 |\vec{E}_j|^2 + 2|\vec{E}_i \cdot \vec{E}_j|^2 \right)$$

  where we denote $\vec{E}_\alpha = \vec{E}_t(\vec{r},\omega_\alpha)$.

- The FWM equations in the frequency domain reads:

(8.6)

$$\frac{dA_1(z,\omega)}{dz} = -i\omega\varepsilon_0\chi_3\, e^{i\beta(z,\omega)z} \begin{bmatrix} \gamma_{Int} A_3(z,\omega)e^{-i\beta(z,\omega)z} * A_4(z,\omega)e^{-i\beta(z,\omega)z} * A_2^*(z,-\omega)e^{-i\beta(z,\omega)z} + \\[2mm] \frac{\mu_{1,1}}{2} A_1(z,\omega)e^{-i\beta(z,\omega)z} * A_1^*(z,-\omega)e^{-i\beta(z,\omega)z} * A_1(z,\omega)e^{-i\beta(z,\omega)z} + \\[2mm] \mu_{1,2} A_2(z,\omega)e^{-i\beta(z,\omega)z} * A_2^*(z,-\omega)e^{-i\beta(z,\omega)z} * A_1(z,\omega)e^{-i\beta(z,\omega)z} + \\[2mm] \mu_{1,3} A_3(z,\omega)e^{-i\beta(z,\omega)z} * A_3^*(z,-\omega)e^{-i\beta(z,\omega)z} * A_1(z,\omega)e^{-i\beta(z,\omega)z} + \\[2mm] \mu_{1,4} A_4(z,\omega)e^{-i\beta(z,\omega)z} * A_4^*(z,-\omega)e^{-i\beta(z,\omega)z} * A_1(z,\omega)e^{-i\beta(z,\omega)z} \end{bmatrix}$$

$$\frac{dA_2(z,\omega)}{dz} = -i\omega\varepsilon_0\chi_3\, e^{i\beta(z,\omega)z} \begin{bmatrix} \gamma_{Int} A_3(z,\omega)e^{-i\beta(z,\omega)z} * A_4(z,\omega)e^{-i\beta(z,\omega)z} * A_1^*(z,-\omega)e^{-i\beta(z,\omega)z} + \\[2mm] \frac{\mu_{2,2}}{2} A_2(z,\omega)e^{-i\beta(z,\omega)z} * A_2^*(z,-\omega)e^{-i\beta(z,\omega)z} * A_2(z,\omega)e^{-i\beta(z,\omega)z} + \\[2mm] \mu_{1,2} A_1(z,\omega)e^{-i\beta(z,\omega)z} * A_1^*(z,-\omega)e^{-i\beta(z,\omega)z} * A_2(z,\omega)e^{-i\beta(z,\omega)z} + \\[2mm] \mu_{2,3} A_3(z,\omega)e^{-i\beta(z,\omega)z} * A_3^*(z,-\omega)e^{-i\beta(z,\omega)z} * A_2(z,\omega)e^{-i\beta(z,\omega)z} + \\[2mm] \mu_{2,4} A_4(z,\omega)e^{-i\beta(z,\omega)z} * A_4^*(z,-\omega)e^{-i\beta(z,\omega)z} * A_2(z,\omega)e^{-i\beta(z,\omega)z} \end{bmatrix}$$

$$\frac{dA_3(z,\omega)}{dz} = -i\omega\varepsilon_0\chi_3\, e^{i\beta(z,\omega)z} \begin{bmatrix} \gamma_{Int} A_1(z,\omega)e^{-i\beta(z,\omega)z} * A_2(z,\omega)e^{-i\beta(z,\omega)z} * A_4^*(z,-\omega)e^{-i\beta(z,\omega)z} + \\[2mm] \frac{\mu_{3,3}}{2} A_3(z,\omega)e^{-i\beta(z,\omega)z} * A_3^*(z,-\omega)e^{-i\beta(z,\omega)z} * A_3(z,\omega)e^{-i\beta(z,\omega)z} + \\[2mm] \mu_{3,4} A_4(z,\omega)e^{-i\beta(z,\omega)z} * A_4^*(z,-\omega)e^{-i\beta(z,\omega)z} * A_3(z,\omega)e^{-i\beta(z,\omega)z} + \\[2mm] \mu_{1,3} A_1(z,\omega)e^{-i\beta(z,\omega)z} * A_1^*(z,-\omega)e^{-i\beta(z,\omega)z} * A_3(z,\omega)e^{-i\beta(z,\omega)z} + \\[2mm] \mu_{2,3} A_2(z,\omega)e^{-i\beta(z,\omega)z} * A_2^*(z,-\omega)e^{-i\beta(z,\omega)z} * A_3(z,\omega)e^{-i\beta(z,\omega)z} \end{bmatrix}$$

$$\frac{dA_4(z,\omega)}{dz} = -i\omega\varepsilon_0\chi_3\, e^{i\beta(z,\omega)z} \begin{bmatrix} \gamma_{Int} A_1(z,\omega)e^{-i\beta(z,\omega)z} * A_2(z,\omega)e^{-i\beta(z,\omega)z} * A_3^*(z,-\omega)e^{-i\beta(z,\omega)z} + \\[2mm] \frac{\mu_{4,4}}{2} A_4(z,\omega)e^{-i\beta(z,\omega)z} * A_4^*(z,-\omega)e^{-i\beta(z,\omega)z} * A_4(z,\omega)e^{-i\beta(z,\omega)z} + \\[2mm] \mu_{3,4} A_3(z,\omega)e^{-i\beta(z,\omega)z} * A_3^*(z,-\omega)e^{-i\beta(z,\omega)z} * A_4(z,\omega)e^{-i\beta(z,\omega)z} + \\[2mm] \mu_{1,4} A_1(z,\omega)e^{-i\beta(z,\omega)z} * A_1^*(z,-\omega)e^{-i\beta(z,\omega)z} * A_4(z,\omega)e^{-i\beta(z,\omega)z} + \\[2mm] \mu_{2,4} A_2(z,\omega)e^{-i\beta(z,\omega)z} * A_2^*(z,-\omega)e^{-i\beta(z,\omega)z} * A_4(z,\omega)e^{-i\beta(z,\omega)z} \end{bmatrix}$$

where the symbol '*' stands for convolution: $f(\omega)*g(\omega) = \int\limits_{-\infty}^{+\infty} f(\omega-\omega')g(\omega')d\omega'$.

- The FWM equations in the time domain reads:

(8.7)

$$\frac{dC_1(z,t)}{dz} = -i\mathfrak{I}^{-1}\left(\beta(\omega+\omega_1,z)C_1(z,\omega+\omega_1) - i\left(\partial_z\beta(\omega+\omega_1,z)\right)\left(z-z_{in}\right)C_1(z,\omega+\omega_1)\right)$$

$$-i\varepsilon_0\chi_3\mathfrak{I}^{-1}\left(\omega+\omega_1\right)\mathfrak{I}\left(\begin{array}{c}\gamma_{Int}C_3(z,t)C_4(z,t)C_2^{\ *}(z,t) \\ \left(\mu_{1,2}\left|C_2(z,t)\right|^2 + \mu_{1,3}\left|C_3(z,t)\right|^2 + \mu_{1,4}\left|C_4(z,t)\right|^2 + \frac{\mu_{1,1}}{2}\left|C_1(z,t)\right|^2\right)C_1(z,t)\end{array}\right)$$

$$\frac{dC_2(z,t)}{dz} = -i\mathfrak{I}^{-1}\left(\beta(\omega+\omega_2,z)C_2(z,\omega+\omega_2) - i\left(\partial_z\beta(\omega+\omega_2,z)\right)\left(z-z_{in}\right)C_2(z,\omega+\omega_2)\right)$$

$$-i\varepsilon_0\chi_3\mathfrak{I}^{-1}\left(\omega+\omega_2\right)\mathfrak{I}\left(\begin{array}{c}\gamma_{Int}C_3(z,t)C_4(z,t)C_1^{\ *}(z,t) \\ \left(\mu_{1,2}\left|C_1(z,t)\right|^2 + \mu_{2,3}\left|C_3(z,t)\right|^2 + \mu_{2,4}\left|C_4(z,t)\right|^2 + \frac{\mu_{2,2}}{2}\left|C_2(z,t)\right|^2\right)C_2(z,t)\end{array}\right)$$

$$\frac{dC_3(z,t)}{dz} = -i\mathfrak{I}^{-1}\left(\beta(\omega+\omega_3,z)C_3(z,\omega+\omega_3) - i\left(\partial_z\beta(\omega+\omega_3,z)\right)\left(z-z_{in}\right)C_3(z,\omega+\omega_3)\right)$$

$$-i\varepsilon_0\chi_3\mathfrak{I}^{-1}\left(\omega+\omega_3\right)\mathfrak{I}\left(\begin{array}{c}\gamma_{Int}C_1(z,t)C_2(z,t)C_4^{\ *}(z,t) \\ \left(\mu_{1,3}\left|C_1(z,t)\right|^2 + \mu_{2,3}\left|C_2(z,t)\right|^2 + \mu_{3,4}\left|C_4(z,t)\right|^2 + \frac{\mu_{3,3}}{2}\left|C_3(z,t)\right|^2\right)C_3(z,t)\end{array}\right)$$

$$\frac{dC_4(z,t)}{dz} = -i\mathfrak{I}^{-1}\left(\beta(\omega+\omega_4,z)C_4(z,\omega+\omega_4) - i\left(\partial_z\beta(\omega+\omega_4,z)\right)\left(z-z_{in}\right)C_4(z,\omega+\omega_4)\right)$$

$$-i\varepsilon_0\chi_3\mathfrak{I}^{-1}\left(\omega+\omega_4\right)\mathfrak{I}\left(\begin{array}{c}\gamma_{Int}C_1(z,t)C_2(z,t)C_3^{\ *}(z,t) \\ \left(\mu_{1,4}\left|C_1(z,t)\right|^2 + \mu_{2,4}\left|C_2(z,t)\right|^2 + \mu_{3,4}\left|C_3(z,t)\right|^2 + \frac{\mu_{4,4}}{2}\left|C_4(z,t)\right|^2\right)C_4(z,t)\end{array}\right)$$

8.2. SU(2) symmetry in four wave mixing

It is presented in this section, that the adiabatic evolution frequency conversion characteristics exhibited in the previous chapters for TWM interactions, can be also adopted for the case of FWM.

The equations dictating the interaction between four waves were displayed in the previous section, Such that $\omega_1 + \omega_2 = \omega_3 + \omega_4$, where $\omega_{\beta \in [1,2,3,4]}$ are the pulses central frequencies. Ignoring the frequency dependence of the electric field transverse profile $E_j(\vec{r}, \omega_\alpha)$, all mode overlaps degenerates to the same value, denoted γ :

$$\mu \triangleq \mu_{i,j} = \gamma_{Int} = \frac{3}{2} \iint \left| \vec{E} \right|^4 dxdy \, .$$

Assuming that the pulses are continuous waves $A_\alpha(z,\omega) = A_\alpha \delta(\omega - \omega_\alpha)$ where $\alpha \in [1,2,3,4]$ yields:

(8.8)

$$\frac{dA_1}{dz} = -i\omega_1 \varepsilon_0 \chi_3 \mu \left[e^{i(\beta_2 + \beta_1 - \beta_3 - \beta_4)z} A_3 A_4 A_2^{*} + \frac{1}{2}|A_1|^2 A_1 + \left(|A_2|^2 + |A_3|^2 + |A_4|^2 \right) A_1 \right]$$

$$\frac{dA_2}{dz} = -i\omega_2 \varepsilon_0 \chi_3 \mu \left[e^{i(\beta_2 + \beta_1 - \beta_3 - \beta_4)z} A_3 A_4 A_1^{*} + \frac{1}{2}|A_2|^2 A_2 + \left(|A_1|^2 + |A_3|^2 + |A_4|^2 \right) A_2 \right]$$

$$\frac{dA_3}{dz} = -i\omega \varepsilon_0 \chi_3 \mu \left[e^{-i(\beta_2 + \beta_1 - \beta_3 - \beta_4)z} A_1 A_2 A_4^{*} + \frac{1}{2}|A_3|^2 A_3 + \left(|A_1|^2 + |A_2|^2 + |A_4|^2 \right) A_3 \right]$$

$$\frac{dA_4}{dz} = -i\omega \varepsilon_0 \chi_3 \mu \left[e^{-i(\beta_2 + \beta_1 - \beta_3 - \beta_4)z} A_1 A_2 A_3^{*} + \frac{1}{2}|A_4|^2 A_4 + \left(|A_1|^2 + |A_2|^2 + |A_3|^2 \right) A_4 \right]$$

We redefine the pulses notations according to the following scheme (1,2,3,4) → (Pump A, Signal, Idler, Pump B).
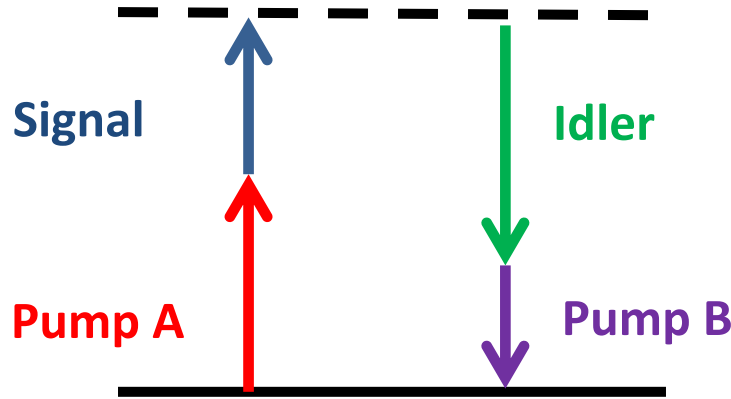
Figure 30. Four wave mixing scheme. Signal pulse is being depleted as the idler pulse is being generated via the pump pulses.

Applying the modified pulses notations to Eq. set (8.8), and assuming that the pump waves (both A and B) are much stronger than the signal and idler waves $|A_B|^2 \gg \left\{ |A_S|^2, |A_I|^2 \right\}$, $|A_B|^2 \gg \left\{ |A_S|^2, |A_I|^2 \right\}$ results in the following:

$$(8.9) \quad \frac{dA_A}{dz} \approx -2i\gamma\omega_A \left(\frac{1}{2}|A_A|^2 + |A_B|^2 \right) A_A$$

$$\frac{dA_B}{dz} = -2i\gamma\omega_B \left(\frac{1}{2}|A_B|^2 + |A_A|^2 \right) A_B$$

$$\frac{dA_I}{dz} = -2i\gamma\omega_I \left(\exp(-i\Delta k \cdot z) A_A A_S A_B^* + \left(|A_A|^2 + |A_B|^2 \right) A_I \right)$$

$$\frac{dA_S}{dz} = -2i\gamma\omega_S \left(\exp(+i\Delta k \cdot z) A_I A_B A_A^* + \left(|A_A|^2 + |A_B|^2 \right) A_S \right)$$

Where $\Delta k = \left(\beta_S + \beta_A - \beta_I - \beta_B \right)$ is the phase mismatch parameter and $\gamma = \frac{\varepsilon_0 \chi_3 \mu}{2}$. Under the assumption that the pump waves are much stronger than the signal and idler waves, one obtain that the effect of four wave mixing for the pump waves results merely in phase modification, hence not affecting to total power carried by the waves. In that case, the pump waves are therefore undepleted, and the effect of FWM is significant only for the idler and signal waves.

The solution of Eq. set (8.9) for the pump waves can be easily deduced:

$$(8.10) \quad A_A(z) = A_{A,0} \exp\left(-i\gamma\omega_A \left(|A_A|^2 + 2|A_B|^2 \right) z \right) = A_{A,0} \exp(-i\phi_A z)$$

$$A_B(z) = A_{B,0} \exp\left(-i\gamma\omega_B \left(|A_B|^2 + 2|A_A|^2 \right) z \right) = A_{B,0} \exp(-i\phi_B z)$$

where $A_{A,0}$ and $A_{B,0}$ are the pump waves amplitudes at $z = 0$.

Substitute Eq. set (8.10) into Eq. set (8.9) for the idler and signal waves results in the following:

$$(8.11) \quad \frac{dA_I}{dz} = -2i\gamma\omega_I \left(\exp\left(-i\left(\Delta k + \phi_A - \phi_B \right) \cdot z \right) A_{A,0} A_{B,0}^* A_S + \left(|A_A|^2 + |A_B|^2 \right) A_I \right)$$

$$\frac{dA_S}{dz} = -2i\gamma\omega_S \left(\exp\left(+i\left(\Delta k + \phi_A - \phi_B \right) \cdot z \right) A_I A_{B,0} A_{A,0}^* + \left(|A_A|^2 + |A_B|^2 \right) A_S \right)$$

We define the following normalized amplitudes:

$$(8.12) \quad C_I = \frac{A_I \exp(i\phi_I z)}{\sqrt{\gamma\omega_I |A_A||A_B|}}, \quad C_S = \frac{A_S \exp(i\phi_S z)}{\sqrt{\gamma\omega_S |A_A||A_B|}}$$

We continue with the derivation of C_I :

$$(8.13) \quad \frac{dC_I}{dz} = \frac{dA_I}{dz} \frac{\exp(i\phi_I z)}{\sqrt{\gamma\omega_I |A_A||A_B|}} + i\phi_I A_I \frac{\exp(i\phi_I z)}{\sqrt{\gamma\omega_I |A_A||A_B|}}$$

$$= i\phi_I C_I - 2i\gamma\omega_I \frac{\exp(i\phi_I z)}{\sqrt{\gamma\omega_I |A_A||A_B|}} \left(\exp\left(-i(\Delta k + \phi_A - \phi_B)\cdot z\right) A_{A,0} A^*_{B,0} A_S + \left(|A_A|^2 + |A_B|^2\right) A_I \right)$$

$$= i\phi_I C_I - 2i\gamma\omega_I \left(|A_A|^2 + |A_B|^2\right) C_I - 2i\gamma\omega_I \exp\left(-i(\Delta k + \phi_A - \phi_B - \phi_I)z\right) \frac{A_{A,0} A^*_{B,0}}{\sqrt{\gamma\omega_I |A_A||A_B|}} C_S \sqrt{\gamma\omega_S |A_A||A_B|} \exp(-i\phi_S z)$$

$$= iC_I \left(\phi_I - 2\gamma\omega_I \left(|A_A|^2 + |A_B|^2\right) \right) - iC_S 2\gamma\sqrt{\omega_I\omega_S} A_{A,0} A^*_{B,0} \exp\left(-i(\Delta k + \phi_A - \phi_B - \phi_I + \phi_S)z\right)$$

Define the coupling strength $\kappa = 4\gamma\sqrt{\omega_I\omega_S} A_{A,0} A^*_{B,0}$ and arrive:

$$(8.14) \quad \frac{dC_I}{dz} = iC_I \left(\phi_I - 2\gamma\omega_I \left(|A_A|^2 + |A_B|^2\right) \right) - iC_S \frac{\kappa}{2} \exp\left(-i(\Delta k + \phi_S - \phi_I + \phi_A - \phi_B)z\right)$$

In the same manner one can obtain the evolution of C_S :

$$(8.15) \quad \frac{dC_S}{dz} = iC_S \left(\phi_S - 2\gamma\omega_S \left(|A_A|^2 + |A_B|^2\right) \right) - iC_I \frac{\kappa^*}{2} \exp\left(i(\Delta k + \phi_S - \phi_I + \phi_A - \phi_B)z\right)$$

we can define ϕ_I, ϕ_S to simplify the equations obtained in the following manner:

$$(8.16) \quad \phi_S - \phi_I + \phi_A - \phi_B + \Delta k = 0$$

$$\phi_S - 2\gamma\omega_S \left(|A_A|^2 + |A_B|^2\right) = -\left(\phi_I - 2\gamma\omega_I \left(|A_A|^2 + |A_B|^2\right) \right) = -\xi$$

The solution is obtained:

$$(8.17) \quad \phi_S = -\frac{\Delta k}{2} + \frac{\gamma}{2}|A_A|^2 \left(2\omega_B - \omega_A + 2\omega_I + 2\omega_S\right) + \frac{\gamma}{2}|A_B|^2 \left(\omega_B - 2\omega_A + 2\omega_I + 2\omega_S\right)$$

$$\phi_I = +\frac{\Delta k}{2} + \frac{\gamma}{2}|A_A|^2 \left(-2\omega_B + \omega_A + 2\omega_I + 2\omega_S\right) + \frac{\gamma}{2}|A_B|^2 \left(-\omega_B + 2\omega_A + 2\omega_I + 2\omega_S\right)$$

The parameter ξ is given by:

$$(8.18) \quad \xi = -\left(\phi_S - 2\gamma\omega_S \left(|A_A|^2 + |A_B|^2 \right) \right) =$$

$$= +\frac{\Delta k}{2} - \frac{\gamma}{2}|A_A|^2 \left(2\omega_B - \omega_A + 2\omega_I - 2\omega_S \right) - \frac{\gamma}{2}|A_B|^2 \left(\omega_B - 2\omega_A + 2\omega_I - 2\omega_S \right)$$

$$= +\frac{\Delta k}{2} - \frac{\gamma\omega_A}{2}|A_A|^2 + \frac{\gamma\omega_B}{2}|A_B|^2$$

The coupled equations posses SU(2) symmetry, written in matrix form:

$$(8.19) \quad \frac{d}{dz}\begin{pmatrix} C_I \\ C_S \end{pmatrix} = -\frac{i}{2}\begin{pmatrix} -2\xi & \kappa \\ \kappa^* & +2\xi \end{pmatrix}\begin{pmatrix} C_I \\ C_S \end{pmatrix}$$

Recall the evolution of TWM in the undepleted pump approximation:

$$(8.20) \quad \frac{d}{dz}\begin{pmatrix} C_1 \\ C_3 \end{pmatrix} = -\frac{i}{2}\begin{pmatrix} -\Delta k & \kappa \\ \kappa^* & +\Delta k \end{pmatrix}\begin{pmatrix} C_1 \\ C_3 \end{pmatrix}$$

The effective phase mismatch parameter is therefore given by

$$(8.21) \quad 2\xi = \Delta k - \gamma\omega_A |A_A|^2 + \gamma\omega_B |A_B|^2$$

Which can also be denoted as $\Delta k_{eff} = 2\xi$, where every wave vector is added the corresponding SPM/XPM term:

$$(8.22) \quad \Delta k = \left(\beta_S + \beta_A - \beta_I - \beta_B \right)$$

$$\beta_S \rightarrow \beta_S + 2\gamma\omega_S \left(|A_A|^2 + |A_B|^2 \right) \qquad \beta_B \rightarrow \beta_B + 2\gamma\omega_B \left(\frac{1}{2}|A_B|^2 + |A_A|^2 \right)$$

$$\beta_A \rightarrow \beta_A + 2\gamma\omega_A \left(\frac{1}{2}|A_A|^2 + |A_B|^2 \right) \qquad \beta_I \rightarrow \beta_I + 2\gamma\omega_I \left(|A_A|^2 + |A_B|^2 \right)$$

which indeed yields the effective phase mismatch 2ξ:

$$\Delta k \rightarrow \Delta k + \gamma |A_A|^2 \left(2\omega_S + \omega_A - 2\omega_I - 2\omega_B \right) + \gamma |A_B|^2 \left(2\omega_S + 2\omega_A - 2\omega_I - \omega_B \right) \Rightarrow$$

$$\Delta k^{eff} = \Delta k - \gamma\omega_A |A_A|^2 + \gamma\omega_B |A_B|^2$$

To conclude, we obtained SU(2) symmetry

$$(8.23) \quad \frac{d}{dz}\begin{pmatrix} C_I \\ C_S \end{pmatrix} = -\frac{i}{2}\begin{pmatrix} -\Delta k_{eff} & \kappa \\ \kappa & +\Delta k_{eff} \end{pmatrix}\begin{pmatrix} C_I \\ C_S \end{pmatrix}$$

with the following definitions:

$$\Delta k_{eff} = \Delta k - \gamma\omega_A \left|A_A\right|^2 + \gamma\omega_B \left|A_B\right|^2 , \; \kappa = 4\gamma\sqrt{\omega_I\omega_S}\, A_{A,0}A^{*}_{B,0}$$

$$C_I = \frac{A_I \exp\left(+i\dfrac{\Delta k}{2}z + i\dfrac{\gamma}{2}\left|A_A\right|^2\left(-2\omega_B + \omega_A + 2\omega_I + 2\omega_S\right)z + i\dfrac{\gamma}{2}\left|A_B\right|^2\left(-\omega_B + 2\omega_A + 2\omega_I + 2\omega_S\right)z\right)}{\sqrt{\gamma\omega_I}\left|A_A\right|\left|A_B\right|}$$

$$C_S = \frac{A_S \exp\left(-i\dfrac{\Delta k}{2}z + i\dfrac{\gamma}{2}\left|A_A\right|^2\left(2\omega_B - \omega_A + 2\omega_I + 2\omega_S\right)z + i\dfrac{\gamma}{2}\left|A_B\right|^2\left(\omega_B - 2\omega_A + 2\omega_I + 2\omega_S\right)z\right)}{\sqrt{\gamma\omega_S}\left|A_A\right|\left|A_B\right|}$$

with the Hamiltonian given in the form Eq. (8.23), the normal adiabatic criteria can be deduced. It is therefore presented that the adiabatic evolution frequency conversion characteristics exhibited in the previous chapters for TWM interactions, can be also adopted for the case of FWM.

9. Future research

In the previous chapters, we presented several topics of research, encompassing areas yet to be fully researched:

1. Theoretical Adiabatic Evolution criteria in the ultrashort regime
   While the condition for an adiabatic evolution exist for the case of nonlinear TWM interactions [25] in the CW regime, adiabatic criteria evolution for ultrashort pulses is still absent. The Hamiltonian presented in Ref. [25] shall be generalized to fit to wideband pulses, towards achieving a general adiabatic criteria.

2. DFG pulse compression realization
   The DFG compression scheme presented in section (7) is to be experimentally validated for the Generation of MIR ultrashort pulse.

3. Experimental validation of adiabatic FWM using silicon photonics
   In contrary to the case of TWM interactions where we facilitated the phase mismatch compensation by adiabatically changing the signs of the second order nonlinear susceptibility, we wish to experimentally exhibit the concept of adiabatic four wave mixing by introducing physical deformations to a silicone waveguide, thus providing the missing momenta by the spatial frequencies introduced by the electric field modal overlap γ_{Int} : (Eq. (8.4))

$$\gamma_{Int}(z) = \gamma_{Int}{}^{0}\left(1 + \xi \cos\left(K_g(z)z\right)\right)$$
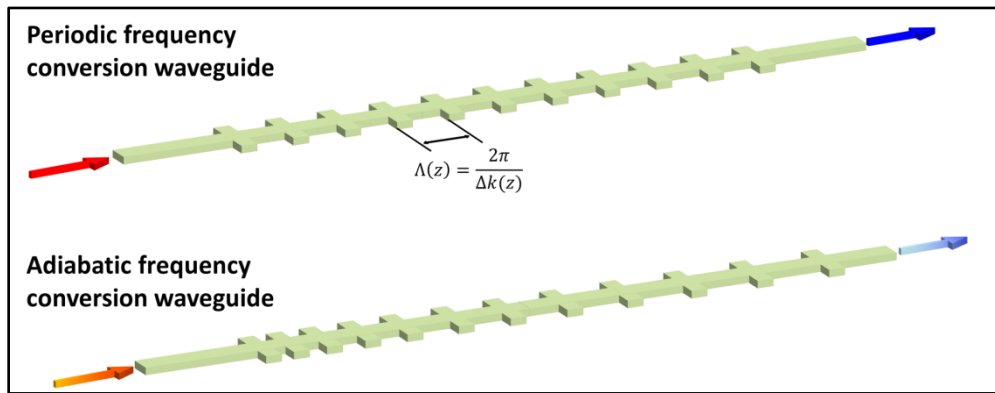
Figure 31. Adiabatic FWM in Silicon Photonics

The design of an optical waveguide tailored to specific application, using the equations introduced in section (8), and the experimental validation of the obtained set of equations is to done ahead.

10. Appendixes

10.1 Appendix A – Spectral domain modeling: derivation and formulation

10.1.1 Spectral modeling derivation

We derive the equations of an input pulse being inserted into a media with chirped second order nonlinear susceptibility. Denoting the fields amplitudes with A_j, where j denotes the frequency ω_j, the electric field can be written as:

$$(A.1) \; E = \sum_j A_j(z) e^{i(\omega_j t - k_j z)} F(x, y) \Delta f$$

where k_j is the electric field wave number, given by $k_j = \dfrac{\omega_j}{c} n(\omega_j)$, z is the optical axis of the crystal,

Δf is the simulation resolution in the frequency domain, and $F(x, y)$ is the electric field mode profile obeying Helmholtz equation:

$$(A.2) \; \nabla_t^2 F(x, y) + \left(\left(\frac{\omega_j n}{c} \right)^2 - k_j^2 \right) F(x, y) = 0 \; .$$

The total electric field in equation (A.1) also obeys Helmholtz equation with nonlinear polarization:

$$(A.3) \; \nabla^2 E - \frac{n^2}{c^2} \frac{\partial^2 E}{\partial t^2} = \mu_0 \frac{\partial^2 P_{NL}}{\partial t^2}$$

Continue with writing the nonlinear polarization term contributing to the SFG term:

$$(A.4) \; P_{NL} = 2\varepsilon_0 \chi_2 E^2 = 2\varepsilon_0 \chi_2 \sum_{j,k} A_j(z) A_k(z) e^{i(\omega_j t - k_j z)} e^{i(\omega_k t - k_k z)} F^2(x, y) \left(\Delta f \right)^2$$

The left side of equation (A.3) is:

$$\nabla^2 E = \left(\nabla_t^2 + \partial_z^2 \right) \sum_j A_j(z) e^{i(\omega_j t - k_j z)} F(x, y) \Delta f = \sum_j A_j(z) e^{i(\omega_j t - k_j z)} \nabla_t^2 F(x, y) \Delta f + \sum_j \partial_z^2 \left(A_j(z) e^{i(\omega_j t - k_j z)} \right) F(x, y) \Delta f$$

$$\nabla^2 E = \sum_j A_j(z) e^{i(\omega_j t - k_j z)} \underbrace{\left[k_j^2 - \left(\frac{\omega_j n}{c} \right)^2 \right]}_{\text{Eq. (A.2)}} F(x, y) \Delta f + \sum_j \partial_z^2 \left(A_j(z) e^{i(\omega_j t - k_j z)} \right) F(x, y) \Delta f$$

75

Applying the following slowly amplitude approximation:

$$\partial_z^2\left(A_j(z)\,\mathrm{e}^{i(\omega_j t-k_j z)}\right)\approx -k_j^2 A_j(z)\,\mathrm{e}^{i(\omega_j t-k_j z)}-2ik_j\,\frac{dA_j(z)}{dz}\,\mathrm{e}^{i(\omega_j t-k_j z)}$$

yields:

$$\nabla^2 E=\sum_j A_j(z)\,\mathrm{e}^{i(\omega_j t-k_j z)}\left(k_j^2-\left(\frac{\omega_j n}{c}\right)^2\right)F(x,y)\Delta f+\sum_j\left(-k_j^2 A_j(z)\,\mathrm{e}^{i(\omega_j t-k_j z)}\,F(x,y)\Delta f\right)$$

$$\nabla^2 E=-\sum_j\left(2ik_j\,\frac{dA_j(z)}{dz}\,\mathrm{e}^{i(\omega_j t-k_j z)}\,F(x,y)\Delta f\right)-\sum_j A_j(z)\left(\frac{\omega_j n}{c}\right)^2\mathrm{e}^{i(\omega_j t-k_j z)}F(x,y)\Delta f$$

$$\nabla^2 E=-\sum_j\left(2ik_j\,\frac{dA_j(z)}{dz}\,\mathrm{e}^{i(\omega_j t-k_j z)}\,F(x,y)\Delta f\right)+\left(\frac{n}{c}\right)^2\frac{\partial^2}{\partial t^2}\sum_j A_j(z)\,\mathrm{e}^{i(\omega_j t-k_j z)}F(x,y)\Delta f$$

$$(A.5)\;\nabla^2 E-\left(\frac{n}{c}\right)^2\frac{\partial^2 E}{\partial t^2}=-\sum_j\left(2ik_j\,\frac{dA_j(z)}{dz}\,\mathrm{e}^{i(\omega_j t-k_j z)}\,F(x,y)\Delta f\right)$$

Substitute Eq. (A.5) into the left side of Eq. (A.3), together with the insertion of Eq. (A.4) into the right side of Eq. (A.3) yields:

$$-\sum_m\left(2ik_m\,\frac{dA_m(z)}{dz}\,\mathrm{e}^{i(\omega_m t-k_m z)}\,F(x,y)\Delta f\right)=2\varepsilon_0\chi_2\mu_0\,\frac{\partial^2\left[\sum_{j,k}A_j(z)A_k(z)\,\mathrm{e}^{i(\omega_j t-k_j z)}\,\mathrm{e}^{i(\omega_k t-k_k z)}\,F^2(x,y)\left(\Delta f\right)^2\right]}{\partial t^2}$$

Multiplying both sides of the above equation with $F^*(x,y)$ and integrating over the cross section results in the following:

$$-\sum_m\left(2ik_m\,\frac{dA_m(z)}{dz}\,\mathrm{e}^{i(\omega_m t-k_m z)}\right)=-2\varepsilon_0\mu_0\chi_2\Upsilon\sum_{j,k}\left(\omega_j+\omega_k\right)^2 A_j(z)A_k(z)\,\mathrm{e}^{i(\omega_j t-k_j z)}\,\mathrm{e}^{i(\omega_k t-k_k z)}\Delta f$$

where $\Upsilon=\dfrac{\int\left|F(x,y)\right|^2 F(x,y)dxdy}{\int\left|F(x,y)\right|^2 dxdy}$.

Using the orthogonally of planar waves one can compare time domain spectral waves:

$$\omega_m = \left(\omega_j + \omega_k \right)$$

$$2ik_m \frac{dA_m(z)}{dz} e^{i(\omega_m t - k_m z)} = -2\varepsilon_0 \mu_0 \chi_2 \Upsilon \sum_{j,k} \left(\omega_j + \omega_k \right)^2 A_j(z) A_k(z) e^{i(\omega_j t - k_j z)} e^{i(\omega_k t - k_k z)} \delta \left(\omega_j + \omega_k - \omega_m \right) \Delta f$$

$$2ik_m \frac{dA_m(z)}{dz} = -\frac{2\chi_2 \omega_m^{\,2}}{c^2} \Upsilon \sum_{j,k} A_j(z) A_k(z) e^{i\left(k_m - k_j - k_k\right)z} \delta \left(\omega_j + \omega_k - \omega_m \right) \Delta f$$

$$(A.6) \quad \frac{dA_m(z)}{dz} = i \frac{\chi_2(z) \omega_m^{\,2}}{k_m c^2} \Upsilon \sum_{j,k} A_j(z) A_k(z) e^{i\left(k_m - k_j - k_k\right)z} \delta \left(\omega_j + \omega_k - \omega_m \right) \Delta f$$

The equations describing the SFG contribution to the fields amplitude were derived. The electromagnetic field intensity [W] is given by:

$$P = \iint dxdy \frac{n}{2\eta_0} \left| F(x,y) \right|^2 \left| A(z) \right|^2 \Delta f = \frac{n}{2\eta_0} \left| A(z) \right|^2 \Delta f \iint \left| F(x,y) \right|^2 dxdy = \frac{n}{2\eta_0} \left| A(z) \right|^2 \Delta f$$

We wish to normalize Eq. (A.6) such that $\dfrac{A_j^{\,2} n(\omega_j)}{2\eta_0} \Delta f$ will be in $\dfrac{W}{m^2}$ units. Define $B(z) \equiv \Upsilon A(z)$:

$$\underbrace{\frac{\left| B(z) \right|^2}{\dfrac{2\eta_0}{n}}}_{} \Delta f = \Upsilon^2 \underbrace{\underbrace{\frac{\left| A(z) \right|^2}{\dfrac{2\eta_0}{n}}}_{W} \Delta f}_{\frac{1}{m^2}} \, [\frac{W}{m^2}] \text{ as we wish to obtain.}$$

Rewriting Eq. set (A.6) in terms of $B(z)$ results in the following:

$$\frac{dB_m(z)}{dz} \frac{1}{\Upsilon} = i \frac{\chi_2(z) \omega_m^{\,2}}{k_m c^2} \Upsilon \sum_{j,k} \frac{B_j(z)}{\Upsilon} \frac{B_k(z)}{\Upsilon} e^{i\left(k_m - k_j - k_k\right)z} \delta \left(\omega_j + \omega_k - \omega_m \right) \Delta f$$

$$(A.7) \quad \frac{dB_m(z)}{dz} = i \frac{\chi_2(z) \omega_m^{\,2}}{k_m c^2} \sum_{j,k} B_j(z) B_k(z) e^{i\left(k_m - k_j - k_k\right)z} \delta \left(\omega_j + \omega_k - \omega_m \right) \Delta f$$

The familiar equation for SFG is introduced. The equation for DFG can now be easily deduced:

$$(A.8) \quad \frac{dB_m(z)}{dz} = i \frac{\chi_2(z) \omega_m^{\,2}}{k_m c^2} \sum_{j,k} B_j(z) B_k^*(z) e^{-i\left(k_j - k_m - k_k\right)z} \delta \left(\omega_m + \omega_k - \omega_j \right) \Delta f$$

10.1.2 Efficient equations formulation for difference frequency generation

We present efficient formulation of Eq. set (A.7) and (A.8) for the case of DFG. Assume we have two pulses, as presented below, denoted as "Signal" and "Pump". The interaction between the two pulses generates a third pulse, denoted as "Idler".
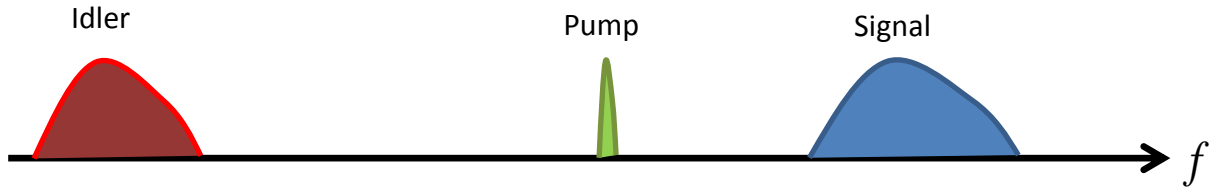
We start with defining the amplitudes:

- $B_S(f_j)$ - Signal amplitudes defined in the range $[f_s^{min}, f_s^{max}]$. The grid is equally spaced with

  spacing Δf . j denotes **ascending** frequencies on the signal grid: $f_s(j) = f_s^{min} + (j-1)\Delta f$.

- $B_P(f_j)$ - Pump amplitudes defined in some range: $[f_p^{min}, f_p^{max}]$. The grid is equally spaced with the same spacing Δf mentioned above . Subscript j denotes **descending** frequencies on the pump grid $f_p(j) = f_p^{max} - (j-1)\Delta f$.

- $B_I(f_j)$ - The idler frequencies will be defined using the pump and signal grids.

  $f_i^{min} = (f_s^{min} - f_p^{max}), f_i^{max} = (f_s^{max} - f_p^{min})$. The grid is equally spaced with the same spacing Δf mentioned above Pay attention that every DFG possible between the signal and the pump exists on the above grid. Subscript j denotes **ascending** frequencies on the idler grid:

  $f_I(j) = (f_s^{min} - f_p^{max}) + (j-1)\Delta f$.

Given that the signal grid contains N_s points: $\dfrac{f_s^{\ max} - f_s^{\ min}}{\Delta f} = (N_s - 1)$, and that the pump grid contains

N_p points: $\dfrac{f_p^{\ max} - f_p^{\ min}}{\Delta f} = (N_p - 1)$, The idler grid will contain:

$$\frac{f_i^{\ max} - f_i^{\ min}}{\Delta f} = \frac{\left(f_s^{\ max} - f_p^{\ min}\right) - \left(f_s^{\ min} - f_p^{\ max}\right)}{\Delta f} = \frac{\left(f_s^{\ max} - f_s^{\ min}\right) + \left(f_p^{\ max} - f_p^{\ min}\right)}{\Delta f}$$

$$\frac{f_i^{\ max} - f_i^{\ min}}{\Delta f} = (N_s - 1) + (N_p - 1) = N_i - 1 \Rightarrow$$

(A.9) $N_i = N_s + N_p - 1$

Let's examine the energy conservation condition $f_{Signal} = f_{Idler} + f_{Pump}$:

$$f_p(k) = f_p^{\ max} - (k-1)\Delta f$$
$$f_s(m) = f_s^{\ min} + (m-1)\Delta f$$
$$f_I(j) = \left(f_s^{\ min} - f_p^{\ max}\right) + (j-1)\Delta f$$
$$f_{Signal} = f_{Idler} + f_{Pump} \Rightarrow$$

$$f_s^{\ min} + (m-1)\Delta f = \left(f_s^{\ min} - f_p^{\ max}\right) + (j-1)\Delta f + f_p^{\ max} - (k-1)\Delta f$$
$$f_s^{\ min} + (m-1)\Delta f = f_s^{\ min} + (j-1)\Delta f + (1-k)\Delta f$$
$$j = m + k - 1$$

We observe, that by using the grids proposed, $\delta\left(\omega_I^{\ j} + \omega_P^{\ k} - \omega_S^{\ m}\right) = \delta(m + k - j - 1)$, which dramatically simplifies the equations. Continue with deriving the simplified equations by inserting the amplitudes defined above. We start with the equations defining the idler pulse, Eq. (A.8).

$$\frac{dB_I(z, f_j)}{dz} = i\frac{\chi_2(z)\omega_j^{\ 2}}{k_j c^2} \sum_{m=1}^{Ns}\sum_{k=1}^{Np} B_S(z, f_m) B^*_{\ P}(z, f_k) e^{-i\left(k_m - k_j - k_k\right)z} \delta\left(\omega_I^{\ j} + \omega_P^{\ k} - \omega_S^{\ m}\right)\Delta f$$

$$\frac{dB_I(z, f_j)}{dz} = i\frac{\chi_2(z)\omega_j^{\ 2}}{k_j c^2} \sum_{m=1}^{Ns}\sum_{k=1}^{Np} B_S(z, f_m) B^*_{\ P}(z, f_k) e^{-i\left(k_m - k_j - k_k\right)z} \delta(m + k - j - 1)\Delta f$$

$$\frac{dB_I(z, f_j)}{dz} = i\frac{\chi_2(z)\omega_j^{\ 2}}{k_j c^2} \sum_{k} B_S(z, f_{1+j-k}) B^*_{\ P}(z, f_k) e^{-i\left(k_{1+j-k} - k_j - k_k\right)z}\Delta f$$

$$\frac{dB_I(z,f_j)}{dz} = i\frac{\chi_2(z)\omega_j^2}{k_j c^2}e^{+ik_j z}\sum_k \underbrace{B_S(z,f_{1+j-k})e^{-i(k_{1+j-k})z}}_{f(1+j-k)}\underbrace{B_P^*(z,f_k)e^{i(k_k)z}}_{g(k)}\Delta f$$

this sum is a convolution. **The equations describing the pump are presented:**

$$(A.10)\ \frac{dB_I(z,f_j)}{dz} = i\frac{\chi_2(z)\omega_j^2}{k_j c^2}e^{+ik_j z}\underbrace{\left(B_S(z,f_m)e^{-jk_m z}\right)*\left(\left(B_P(z,f_k)e^{-jk_k z}\right)^*\right)}_{conv\left(B_S(z,f_m)e^{-jk_m z},\left(B_P(z,f_k)e^{-jk_k z}\right)^*\right)}\Delta f$$

Continue with defining the pump equations:

$$\frac{dB_P(z,f_k)}{dz} = i\frac{\chi_2(z)\omega_k^2}{k_k c^2}\sum_{j=1}^{NI}\sum_{m=1}^{Ns}B_S(z,f_m)B_I^*(z,f_j)e^{-i(k_m-k_j-k_k)z}\,\delta\left(\omega_I^{\,j}+\omega_P^{\,k}-\omega_S^{\,m}\right)\Delta f$$

$$\frac{dB_P(z,f_k)}{dz} = i\frac{\chi_2(z)\omega_k^2}{k_k c^2}\sum_{j=1}^{NI}\sum_{m=1}^{Ns}B_S(z,f_m)B_I^*(z,f_j)e^{-i(k_m-k_j-k_k)z}\,\delta\left(m+k-j-1\right)\Delta f$$

$$(A.11)\ \frac{dB_P(z,f_k)}{dz} = i\frac{\chi_2(z)\omega_k^2}{k_k c^2}e^{ik_k z}\sum_m \underbrace{\left(B_S(z,f_m)e^{-ik_m z}\right)}_{f(m)}\underbrace{\left(B_I^*(z,f_{m+k-1})e^{-ik_{m+k-1}z}\right)^*}_{f(m+k-1)}\Delta f$$

now we got correlation function instead of convolution

For brevity we define $S_m \equiv B_S(z,f_m)e^{-ik_m z}$, $I_m \equiv B_I(z,f_m)e^{-ik_m z}$. For the calculation of the pump amplitudes it is therefore required to calculate $C_k = \sum_m S_m I_{m+k-1}^*\Delta f$ for $k=1:N_p$, where S_m contains

N_s samples, and I_m contains N_i samples. When Matlab R2013a calculates correlation using **xcorr** function, it zero-pad the shortest input (hence the signal):

$$f(m) = xcorr\left([S_1\,S_2\,S_3\ldots S_{N_s}],[I_1 I_2 I_3\ldots I_{N_i}]\right):$$

$$\boxed{S_1\quad S_2\quad S_3\ldots S_{N_s}\quad \underbrace{0\,0\,0\ldots0}_{N_p\ zeros}}$$

$$m=1\quad I_1^*\,I_2^*\,I_3^*\ldots I_{N_i-1}^*\boxed{I_{N_i}^*}$$

$$m=2\quad\quad I_1^*\,I_2^*\,I_3^*\ldots\quad\quad\boxed{I_{N_i-1}^*I_{N_i}^*}$$

$$\vdots$$

$$m = N_s \qquad I_1^* I_2^* \ldots I_{N_p-1}^* \quad \boxed{I_{N_p}^* I_{N_p+1}^* \quad \ldots\ldots I_{N_i}^*}$$

$$m = N_s+1 \qquad I_1^* I_2^* \ldots \quad \boxed{I_{N_p-1}^* I_{N_p}^* \quad \ldots \quad I_{N_i-1}^*} I_{N_i}^*$$

$$\vdots$$

$$m = N_i \qquad\qquad \boxed{I_1^* \quad I_2^* \ldots \qquad I_{N_s}^*} I_{N_s+1}^* \cdots I_{N_i}^*$$

The rectangles highlights the elements that are being multiplied for each element of the correlation vector. For example, the first element in the correlation vector is $S_1 I_{N_i}^*$, the second term is $\left(S_1 I_{N_i-1}^* + S_2 I_{N_i}^*\right)$ and so forth. Pay attention to $m = N_s$:

$$\sum_m S_m I_{m+N_p-1}^* \Delta f = \sum_m \left(B_S(z,f_m)e^{-ik_m z}\right)\left(B_I(z,f_{m+k-1})e^{-ik_{m+k-1}z}\right)^* \Bigg|_{k=N_p} \Delta f$$

which is the term that contributes to $k = N_p$ in Eq. set (3.11). Pay attention to $m = N_i$:

$$\sum_m S_m I_m^* \Delta f = \sum_m \left(B_S(z,f_m)e^{-ik_m z}\right)\left(B_I(z,f_{m+k-1})e^{-ik_{m+k-1}z}\right)^* \Bigg|_{k=1} \Delta f$$

which is the term that contributes to $k = N_p$ in Eq. set (3.11).

In conclude ,the terms that contributes to $\left(k = 1 : N_p\right)$ are the flipped xcorr elements between $\left(N_s : N_i\right)$. The equations describing the pump pulse were derived:

$$(A.12) \quad \frac{dB_p(z,f_k)}{dz} = i\frac{\chi_2(z)\omega_k^2}{k_k c^2} e^{ik_k z} \underbrace{\left(B_S(z,f_m)e^{-ik_m z}\right)\odot\left(B_I(z,f_j)e^{-ik_j z}\right)}_{flip(\text{xcorr}(B_S(z,f_m)e^{-ik_m z}, B_I(z,f_j)e^{-ik_j z})_{N_s:N_i})}\Delta f$$

The equations describing the signal pulse can be deduced in the same manner:

$$\frac{dB_S(z,f_m)}{dz} = i\frac{\chi_2(z)\omega_m^2}{k_m c^2}\sum_{j=1}^{NI}\sum_{k=1}^{Np} B_P(z,f_k)B_I(z,f_j)\,\mathrm{e}^{+i\left(k_m-k_j-k_k\right)z}\,\delta\left(\omega_I^{\,j}+\omega_P^{\,k}-\omega_S^{\,m}\right)\Delta f$$

$$\frac{dB_S(z,f_m)}{dz} = i\frac{\chi_2(z)\omega_m^2}{k_m c^2}\,\mathrm{e}^{ik_m z}\sum_{j=1}^{NI}\sum_{k=1}^{Np}\left(B_P(z,f_k)\mathrm{e}^{-ik_k z}\right)\left(B_I(z,f_j)\mathrm{e}^{-ik_j z}\right)\delta\left(m+k-j-1\right)\Delta f$$

$$\frac{dB_S(z,f_m)}{dz} = i\frac{\chi_2(z)\omega_m^2}{k_m c^2}\,\mathrm{e}^{ik_m z}\sum_{k}\left(B_P(z,f_k)\mathrm{e}^{-ik_k z}\right)\left(B_I(z,f_{m+k-1})\mathrm{e}^{-ik_{m+k-1} z}\right)\Delta f$$

$$(A.13)\quad \frac{dB_S(z,f_m)}{dz} = i\frac{\chi_2(z)\omega_m^2}{k_m c^2}\,\mathrm{e}^{ik_m z}\underbrace{\left(B_P(z,f_k)\mathrm{e}^{-ik_k z}\right)\odot\left(\left(B_I(z,f_j)\mathrm{e}^{-ik_j z}\right)^*\right)}_{flip(\mathrm{xcorr}(B_P(z,f_k)\mathrm{e}^{-ik_k z},\,B_I^{\,*}(z,f_j)\mathrm{e}^{+ik_j z})_{N_P:N_i})}\Delta f$$

The total set of formulated equations is presented:

$$(A.14)\,\frac{dB_I(z,f_j)}{dz} = i\frac{\chi_2(z)\omega_j^2}{k_j c^2}\,\mathrm{e}^{+ik_j z}\left(B_S(z,f_m)\mathrm{e}^{-jk_m z}\right)*\left(\left(B_P(z,f_k)\mathrm{e}^{-jk_k z}\right)^*\right)\Delta f$$

$$\frac{dB_p(z,f_k)}{dz} = i\frac{\chi_2(z)\omega_k^2}{k_k c^2}\,\mathrm{e}^{ik_k z}\left(B_S(z,f_m)\mathrm{e}^{-ik_m z}\right)\odot\left(B_I(z,f_j)\mathrm{e}^{-ik_j z}\right)\Delta f$$

$$\frac{dB_S(z,f_m)}{dz} = i\frac{\chi_2(z)\omega_m^2}{k_m c^2}\,\mathrm{e}^{ik_m z}\left(B_p(z,f_k)\mathrm{e}^{-ik_k z}\right)\odot\left(\left(B_I(z,f_j)\mathrm{e}^{-ik_j z}\right)^*\right)\Delta f$$

10.2 Appendix B- Time domain modeling derivation

Start with Maxwell equations in the presence of nonlinear polarization term:

$$(B.1)\, \nabla \times \vec{E} = -\frac{\partial \vec{B}}{\partial t} = -\mu \frac{\partial \vec{H}}{\partial t}$$

$$(B.2)\, \nabla \times \vec{H} = \frac{\partial \vec{D}}{\partial t} = \frac{\partial \left(\varepsilon_0 \vec{E} + \vec{P}_L + \vec{P}_{NL} \right)}{\partial t} = \frac{\partial \left(\varepsilon_0 \vec{E} + \varepsilon_0 \chi \vec{E} + \vec{P}_{NL} \right)}{\partial t} \Rightarrow$$

$$(B.3)\, \nabla \times \vec{H} = \frac{\partial \left(\varepsilon_0 \left(1 + \chi \right) \vec{E} + \vec{P}_{NL} \right)}{\partial t} = \frac{\partial \left(\varepsilon_0 n^2 \vec{E} + \vec{P}_{NL} \right)}{\partial t}$$

Apply curl on Eq. (B.1):

$$(B.4)\, \nabla \times \left(\nabla \times \vec{E} \right) = -\mu \frac{\partial \left(\nabla \times \vec{H} \right)}{\partial t} \bigg|_{Eq(B.3)} = -\mu \frac{\partial}{\partial t} \left(\frac{\partial \left(\varepsilon_0 n^2 \vec{E} + \vec{P}_{NL} \right)}{\partial t} \right)$$

$$(B.5)\, -\nabla^2 \vec{E} + \nabla \underbrace{\left(\nabla \cdot \vec{E} \right)}_{=0} = - \underbrace{\mu \varepsilon_0}_{\frac{1}{c^2}} n^2 \frac{\partial^2 \vec{E}}{\partial t^2} - \mu \frac{\partial^2 \vec{P}_{NL}}{\partial t^2} \Rightarrow$$

$$(B.6)\, \nabla^2 \vec{E} = +\mu \varepsilon_0 n^2 \frac{\partial^2 \vec{E}}{\partial t^2} + \mu \frac{\partial^2 \vec{P}_{NL}}{\partial t^2}$$

We would like to make some of the calculations in the frequency domain:

$$(B.7)\, A(z,t) = \frac{1}{2} \int_0^{+\infty} \frac{d\omega}{2\pi} \left(A(z,\omega) e^{i\left(\omega t - \frac{\omega n(\omega)}{c} z \right)} + A^*(z,\omega) e^{-i\left(\omega t - \frac{\omega n(\omega)}{c} z \right)} \right) =$$

$$\frac{1}{2} \int_0^{+\infty} \frac{d\omega}{2\pi} A(z,\omega) e^{i\left(\omega t - \frac{\omega n(\omega)}{c} z \right)} + \underbrace{\frac{1}{2} \int_0^{+\infty} \frac{d\omega}{2\pi} A^*(z,\omega) e^{-i\left(\omega t - \frac{\omega n(\omega)}{c} z \right)}}_{\omega' = -\omega} =$$

$$\frac{1}{2} \int_0^{+\infty} \frac{d\omega}{2\pi} A(z,\omega) e^{i\left(\omega t - \frac{\omega n(\omega)}{c} z \right)} + \frac{1}{2} \int_0^{-\infty} \frac{-d\omega'}{2\pi} A^*(z,-\omega') e^{+i\left(\omega t - \frac{\omega n(\omega)}{c} z \right)} =$$

$$= \frac{1}{2} \int_0^{+\infty} \frac{d\omega}{2\pi} A(z,\omega) e^{i\left(\omega t - \frac{\omega n(\omega)}{c} z \right)} + \frac{1}{2} \int_{-\infty}^{0} \frac{d\omega}{2\pi} A^*(z,-\omega) e^{+i\left(\omega t - \frac{\omega n(\omega)}{c} z \right)} =$$

$$= \int_{-\infty}^{+\infty} \frac{d\omega}{2\pi} \frac{1}{2} \left(A(z,\omega) + A^*(z,-\omega) \right) e^{+i\left(\omega t - \frac{\omega n(\omega)}{c} z \right)}$$

Hence, the Fourier transform of the electromagnetic field $A(z,t)$ is given by:

$$(B.8)\ \Im\big(E(z,t)\big) = \vec{E}(z,\omega) = \frac{1}{2}\Bigg(\underbrace{\vec{A}(z,\omega)}_{\omega>0} + \underbrace{\vec{A}^*(z,-\omega)}_{\omega<0} \Bigg) e^{-i\frac{\omega n(\omega)}{c}z}$$
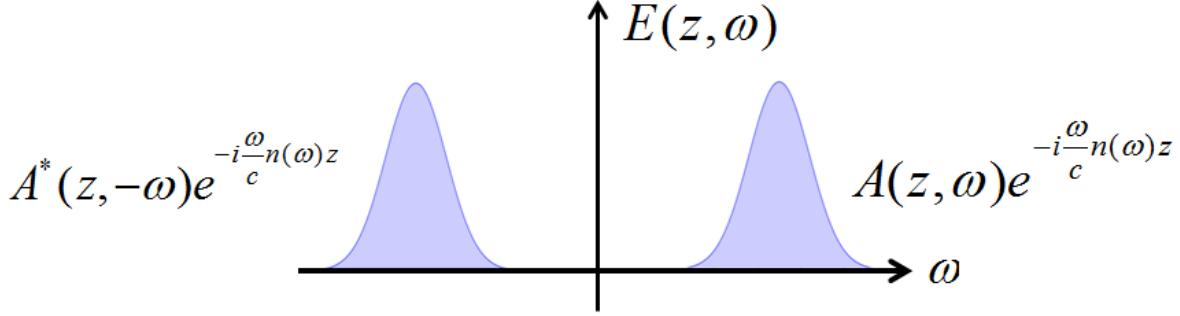
Figure 32. Frequency domain field presentation

Averaging over the transverse dimensions $\int dxdy$, and applying Fourier transform to Eq. (B.6) yields:

$$(B.9)\ \partial_z^{\,2}\vec{E}(z,\omega) = -\mu\varepsilon_0 n^2\omega^2\vec{E}(z,\omega) - \mu\omega^2\vec{P}_{NL}(z,\omega)\Big|_{\beta(\omega)=\frac{\omega n}{c}} = -\beta^2(\omega)\vec{E}(z,\omega) - \mu\omega^2\vec{P}_{NL}(z,\omega)$$

Substitute Eq. (B.7) into Eq. (B.8):

$$\partial_z^{\,2}\Bigg(\frac{1}{2}\Bigg(\underbrace{\vec{A}(z,\omega)}_{\omega>0} + \underbrace{\vec{A}^*(z,-\omega)}_{\omega<0} \Bigg)e^{-i\beta(\omega)z} \Bigg) = \underbrace{\frac{1}{2}\Big(\partial_z^{\,2}\vec{A}(z,\omega) + \cancel{\partial_z^{\,2}\vec{A}^*(z,-\omega)}\Big)e^{-i\beta(\omega)z}}_{Ignored\ Because\ of\ Slowly\ Varying\ Envelope} - \beta^2(\omega)\vec{E}(z,\omega)$$

$$-i\beta(\omega)\Big(\partial_z\vec{A}(z,\omega) + \partial_z\vec{A}^*(z,-\omega)\Big)e^{-i\beta(\omega)z}$$

$$(B.10)\ \partial_z^{\,2}\vec{E}(z,\omega) + \beta^2(\omega)\vec{E}(z,\omega) = -i\beta(\omega)\Big(\partial_z\vec{A}(z,\omega) + \partial_z\vec{A}^*(z,-\omega)\Big)e^{-i\beta(\omega)z}$$

Substitute Eq. (B.10) into Eq. (B.9) yields:

$$(B.11)\ -i\beta(\omega)\Big(\partial_z\vec{A}(z,\omega) + \partial_z\vec{A}^*(z,-\omega)\Big)e^{-i\beta(\omega)z} = -\mu\omega^2\vec{P}_{NL}(z,\omega)$$

It is time to write down the nonlinear polarization term, assuming the electric field is polarized along x:

$$P_{NL}(t) = 2\varepsilon_0\chi(z)E^2(z,t) \Rightarrow$$
$$(B.12)\ P_{NL}(\omega) = 2\varepsilon_0\chi(z)E(z,\omega)*E(z,\omega)$$

Substitute Eq. (B.12) into Eq. (B.11):

$$-i\beta(\omega)\left(\partial_z A(z,\omega)+\partial_z A^*(z,-\omega)\right)e^{-i\beta(\omega)z}=-\mu\omega^2 2\varepsilon_0\chi(z)E(z,\omega)*E(z,\omega)\Rightarrow$$

$$\left(\partial_z A(z,\omega)+\partial_z A^*(z,-\omega)\right)e^{-i\beta(\omega)z}=-2i\frac{\omega^2\mu\varepsilon_0\chi(z)}{\beta(\omega)}E(z,\omega)*E(z,\omega)\Rightarrow$$

$$\left(\partial_z A(z,\omega)+\partial_z A^*(z,-\omega)\right)e^{-i\beta(\omega)z}=-2i\frac{\left(\dfrac{\omega}{c}\right)^2\chi(z)}{\dfrac{\omega n(\omega)}{c}}E(z,\omega)*E(z,\omega)\Rightarrow$$

$$(B.13)\ \left(\partial_z A(z,\omega)+\partial_z A^*(z,-\omega)\right)e^{-i\beta(\omega)z}=-2i\frac{\omega}{c}\frac{\chi(z)}{n(\omega)}E(z,\omega)*E(z,\omega)$$

The electromagnetic field is composed of three pulses: the signal, the pump and the idler. We therefore write:

$$(B.14)\ \begin{bmatrix}\left(\partial_z A_s(z,\omega)+\partial_z A_s^*(z,-\omega)\right)e^{-i\beta(\omega)z}\ +\\ \left(\partial_z A_p(z,\omega)+\partial_z A_p^*(z,-\omega)\right)e^{-i\beta(\omega)z}\ +\\ \left(\partial_z A_i(z,\omega)+\partial_z A_i^*(z,-\omega)\right)e^{-i\beta(\omega)z}\ +\end{bmatrix}=$$

$$=-i\frac{\omega}{2c}\frac{\chi(z)}{n(\omega)}\begin{bmatrix}\left(A_s(z,\omega)+A_s^*(z,-\omega)\right)e^{-i\beta(\omega)z}\ +\\ \left(A_p(z,\omega)+A_p^*(z,-\omega)\right)e^{-i\beta(\omega)z}\ +\\ \left(A_i(z,\omega)+A_i^*(z,-\omega)\right)e^{-i\beta(\omega)z}\ +\end{bmatrix}*\begin{bmatrix}\left(A_s(z,\omega)+A_s^*(z,-\omega)\right)e^{-i\beta(\omega)z}\ +\\ \left(A_p(z,\omega)+A_p^*(z,-\omega)\right)e^{-i\beta(\omega)z}\ +\\ \left(A_i(z,\omega)+A_i^*(z,-\omega)\right)e^{-i\beta(\omega)z}\ +\end{bmatrix}$$

We start with writing the equations for the signal: $\omega_s=\omega_i+\omega_p$. By looking on the spectral shape of the convolved signals one deduces:

$$(B.15)\ \partial_z A_s(z,\omega)e^{-i\beta(\omega)z}=-i\frac{\omega}{c}\frac{\chi(z)}{n(\omega)}\left(A_i(z,\omega)e^{-i\beta(\omega)z}*A_p(z,\omega)e^{-i\beta(\omega)z}\right)$$
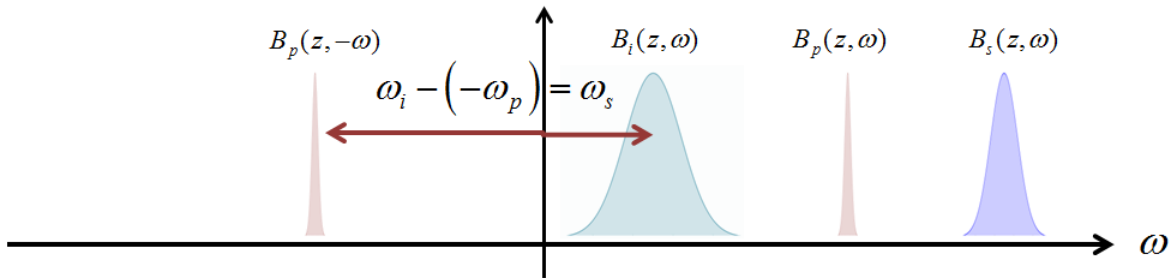
Figure 33. The generated idler. Pictorial view of the convolution term in equation (B.15).

$$\partial_z A_s(z,\omega)e^{-i\beta(\omega)z} = \partial_z\left(A_s(z,\omega)e^{-i\beta(\omega)z}\right) + i\beta(\omega)A_s(z,\omega)e^{-i\beta(\omega)z} \Rightarrow$$

$$(\text{B.16})\ \partial_z\left(A_s(z,\omega)e^{-i\beta(\omega)z}\right) + i\beta(\omega)\left(A_s(z,\omega)e^{-i\beta(\omega)z}\right) = -i\frac{\omega}{c}\frac{\chi(z)}{n(\omega)}\left(A_i(z,\omega)e^{-i\beta(\omega)z}\right)*\left(A_p(z,\omega)e^{-i\beta(\omega)z}\right)$$

We define $\tilde{A}_\beta(z,\omega) = A_\beta(z,\omega)e^{-i\beta(\omega)z}$

$$(\text{B.17})\ \tilde{A}_\beta^{\ *}(z,-\omega) = A_\beta^{\ *}(z,-\omega)e^{+i\beta(-\omega)z} = A_\beta^{\ *}(z,-\omega)e^{-i\beta(\omega)z}$$

We can therefore write:

$$(\text{B.18})\ \partial_z\tilde{A}_s(z,\omega) + i\beta(\omega)\tilde{A}_s(z,\omega) = -i\frac{\omega}{c}\frac{\chi(z)}{n(\omega)}\tilde{A}_i(z,\omega)*\tilde{A}_p(z,\omega)$$

The equations describing the rest of the pulses can be deduced in the same manner, yielding the following set of equations:

$$(\text{B.19})\ \partial_z\tilde{A}_s(z,\omega) + i\beta(\omega)\tilde{A}_s(z,\omega) = -i\frac{\omega}{c}\frac{\chi(z)}{n(\omega)}\tilde{A}_i(z,\omega)*\tilde{A}_p(z,\omega)$$

$$\partial_z\tilde{A}_p(z,\omega) + i\beta(\omega)\tilde{A}_p(z,\omega) = -i\frac{\omega}{c}\frac{\chi(z)}{n(\omega)}\tilde{A}_s(z,\omega)*\tilde{A}_i^{\ *}(z,-\omega)$$

$$\partial_z\tilde{A}_i(z,\omega) + i\beta(\omega)\tilde{A}_i(z,\omega) = -i\frac{\omega}{c}\frac{\chi(z)}{n(\omega)}\tilde{A}_s(z,\omega)*\tilde{A}_p^{\ *}(z,-\omega)$$

One can define:

$$(\text{B.20})\ e^{i\omega_\beta t}A_\beta(z,t) = \Im^{-1}\left(\tilde{A}_\beta(z,\omega)\right) = \int_{-\infty}^{+\infty}\frac{d\omega}{2\pi}\tilde{A}_\beta(z,\omega)e^{i\omega t} = \int_{-\infty}^{+\infty}\frac{d\omega}{2\pi}A_\beta(z,\omega)e^{-i\beta(\omega)z}e^{i\omega t}$$

Applying complex conjugate on the equation above:

$$e^{-i\omega_\beta t}A_\beta^{\ *}(z,t) = \int_{-\infty}^{+\infty}\frac{d\omega}{2\pi}A_\beta^{\ *}(z,\omega)e^{+i\beta(\omega)z}e^{-i\omega t}\Bigg|_{\omega'=-\omega} \Rightarrow$$

$$e^{-i\omega_\beta t}A_\beta^{\ *}(z,t) = \int_{+\infty}^{-\infty}\frac{-d\omega'}{2\pi}A_\beta^{\ *}(z,-\omega')e^{+i\beta(-\omega')z}e^{i\omega't} = \int_{+\infty}^{-\infty}\frac{d\omega'}{2\pi}A_\beta^{\ *}(z,-\omega')e^{-i\beta(\omega')z}e^{i\omega't} = \Im^{-1}\left(\tilde{A}_\beta^{\ *}(z,-\omega)\right)$$

$$(\text{B.21})\ e^{-i\omega_\beta t}A_\beta^{\ *}(z,t) = \Im^{-1}\left(\tilde{A}_\beta^{\ *}(z,-\omega)\right)$$

Define: (B.22) $C_\beta(z,\omega) = \int_{-\infty}^{+\infty} A_\beta(z,t)e^{-i\omega t}dt \Rightarrow$

one can obtain:

$$(B.23)\ \Im\left(e^{i\omega_\beta t}A_\beta(z,t)\right) = \int_{-\infty}^{+\infty} e^{i\omega_\beta t}A_\beta(z,t)e^{-i\omega t}dt = \int_{-\infty}^{+\infty} A_\beta(z,t)e^{-i\left(\omega-\omega_\beta\right)t}dt = C_\beta(z,\omega-\omega_\beta)$$

which implies:

$$(B.24)\ \tilde{A}_\beta(z,\omega) = C_\beta(z,\omega-\omega_\beta)$$

Let's look on the first equation in Eq. set (B.19):

$$\partial_z\tilde{A}_s(z,\omega) + i\beta(\omega)\tilde{A}_s(z,\omega) = -i\frac{\omega}{c}\frac{\chi(z)}{n(\omega)}\tilde{A}_i(z,\omega)*\tilde{A}_p(z,\omega)$$

Combine with Eq. (B.24):

$$(B.25)\ \partial_z C_s(z,\omega-\omega_s) + i\beta(\omega)C_s(z,\omega-\omega_s) = -i\frac{\omega}{c}\frac{\chi(z)}{n(\omega)}C_i(z,\omega-\omega_i)*C_p(z,\omega-\omega_p) \Rightarrow$$

$$\partial_z C_s(z,\omega) + i\beta(\omega+\omega_s)C_s(z,\omega) = -i\frac{\omega+\omega_s}{cn(\omega+\omega_s)}\chi(z)\left(C_i(z,\omega-\omega_i)*C_p(z,\omega-\omega_p)\right)_{\omega+\omega_s}$$

We simplify the equation using the following identity:

$$(B.26)\ \Im^{-1}\left(C(z,\omega-\omega_\beta)\right) = e^{i\omega_\beta t}C(z,t)$$

$$\Im^{-1}\left(C(z,\omega-\omega_\beta)\right) = \int_{-\infty}^{+\infty}\frac{d\omega}{2\pi}C(z,\omega-\omega_\beta)e^{i\omega t} = e^{i\omega_\beta t}\int_{-\infty}^{+\infty}\frac{d\omega}{2\pi}C(z,\omega-\omega_\beta)e^{i\left(\omega-\omega_\beta\right)t}\Bigg|_{\omega-\omega_\beta=\omega'}$$

$$= e^{i\omega_\beta t}\int_{-\infty}^{+\infty}\frac{d\omega'}{2\pi}C(z,\omega')e^{i\omega't} = e^{i\omega_\beta t}C(z,t)$$

87

Inverse transform Eq. (B.25):

(B.27) $\Im^{-1}\left(Left\ Side\right) = \partial_z \Im^{-1}C_s(z,\omega) + i\Im^{-1}\left(\beta(\omega+\omega_s)C_s(z,\omega)\right) \Rightarrow$

$\Im^{-1}\left(Left\ Side\right) = \partial_z C_s(z,t) + i\Im^{-1}\left(\beta(\omega+\omega_s)\Im C_s(z,t)\right)$

$\Im^{-1}\left(C_i(z,\omega-\omega_i) * C_p(z,\omega-\omega_p)\right)_{\omega+\omega_s}\Big|_{eq.B26} = e^{-i\omega_s t}\Im^{-1}\left(C_i(z,\omega-\omega_i) * C_p(z,\omega-\omega_p)\right)_{\omega} =$

$= e^{-i\omega_s t}\Im^{-1}C_i(z,\omega-\omega_i)\Im^{-1}C_p(z,\omega-\omega_p) =$

$= e^{-i\omega_s t}e^{i\omega_i t}e^{i\omega_p t}\Im^{-1}C_i(z,\omega)\Im^{-1}C_p(z,\omega)\Big|_{\omega_s=\omega_i+\omega_p} =$

$= \Im^{-1}C_i(z,\omega)\Im^{-1}C_p(z,\omega) = C_i(z,t)C_p(z,t)$

Eq. (B.27) in the time reads:

(B.28) $\dfrac{\partial C_s(z,t)}{\partial z} + i\Im^{-1}\left(\beta(\omega+\omega_s)\Im C_s(z,t)\right) = -i\chi(z)\Im^{-1}\left(\dfrac{\omega+\omega_s}{n(\omega+\omega_s)c}\Im\left(C_i(z,t)C_p(z,t)\right)\right)$

The same manipulation can be done one for the pump and idler pulses, yielding the above set of equations:

(B.29) $\dfrac{\partial C_s(z,t)}{\partial z} + i\Im^{-1}\left(\beta(\omega+\omega_s)\Im C_s(z,t)\right) = -i\chi(z)\Im^{-1}\left(\dfrac{\omega+\omega_s}{n(\omega+\omega_s)c}\Im\left(C_i(z,t)C_p(z,t)\right)\right)$

$\dfrac{\partial C_p(z,t)}{\partial z} + i\Im^{-1}\left(\beta(\omega+\omega_p)\Im C_p(z,t)\right) = -i\chi(z)\Im^{-1}\left(\dfrac{\omega+\omega_p}{n(\omega+\omega_p)c}\Im\left(C_s(z,t)C_i^*(z,t)\right)\right)$

$\dfrac{\partial C_i(z,t)}{\partial z} + i\Im^{-1}\left(\beta(\omega+\omega_i)\Im C_i(z,t)\right) = -i\chi(z)\Im^{-1}\left(\dfrac{\omega+\omega_i}{n(\omega+\omega_i)c}\Im\left(C_s(z,t)C_p^*(z,t)\right)\right)$

10.3 Appendix C- Flux energy equation: derivation and validation

10.3.1 The energy flux equation derivation
Start with Maxwell equation:

$$(C.1)\, \nabla \times \vec{E} = -\frac{\partial \vec{B}}{\partial t} = -\mu \frac{\partial \vec{H}}{\partial t}$$

$$(C.2)\, \nabla \times \vec{H} = \frac{\partial \vec{D}}{\partial t}$$

where D is given by $\vec{D} = \varepsilon_0 \vec{E} + \vec{P}_L + \vec{P}_{NL} = \varepsilon_0 \vec{E} + \varepsilon_0 \chi \vec{E} + \vec{P}_{NL} = \varepsilon_0 (1 + \chi) \vec{E} + \vec{P}_{NL} = \varepsilon \vec{E} + \vec{P}_{NL}$.

We continue with the calculation of the energy flux density given by:

$$(C.3)\, \vec{u}_e = \frac{1}{2}\left(\vec{E} \cdot \vec{D} + \vec{B} \cdot \vec{H} \right) = \frac{1}{2}\left(\vec{E} \cdot \left(\varepsilon \vec{E} + \vec{P}_{NL} \right) + \mu \vec{H} \cdot \vec{H} \right) = \frac{1}{2}\left(\varepsilon \vec{E} \cdot \vec{E} + \mu \vec{H} \cdot \vec{H} + \vec{P}_{NL} \cdot \vec{E} \right)$$

$$\frac{\partial u_e}{\partial t} = \frac{\partial}{\partial t}\left(\frac{1}{2}\left(\varepsilon \vec{E} \cdot \vec{E} + \mu \vec{H} \cdot \vec{H} + \vec{P}_{NL} \cdot \vec{E} \right) \right) = \varepsilon \frac{\partial \vec{E}}{\partial t} \cdot \vec{E} + \mu \frac{\partial \vec{H}}{\partial t} \cdot \vec{H} + \frac{1}{2} \frac{\partial \left(\vec{P}_{NL} \cdot \vec{E} \right)}{\partial t}$$

From Eq. (C.2) one deduces:

$$\nabla \times \vec{H} = \frac{\partial \left(\varepsilon \vec{E} + \vec{P}_{NL} \right)}{\partial t} = \varepsilon \frac{\partial \vec{E}}{\partial t} + \frac{\partial \vec{P}_{NL}}{\partial t} \Rightarrow$$

$$(C.4)\, \varepsilon \frac{\partial \vec{E}}{\partial t} = \nabla \times \vec{H} - \frac{\partial \vec{P}_{NL}}{\partial t}$$

From Eq. (C.1) one deduces:

$$(C.5)\, \mu \frac{\partial \vec{H}}{\partial t} = -\nabla \times \vec{E}$$

Incorporation of Eq. (C.4) and Eq. (C.5) into Eq. (C.3) yields the following:

$$(C.6)\, \frac{\partial u_e}{\partial t} = \left(\nabla \times \vec{H} - \frac{\partial \vec{P}_{NL}}{\partial t} \right) \cdot \vec{E} + \left(-\nabla \times \vec{E} \right) \cdot \vec{H} + \frac{1}{2} \frac{\partial \left(\vec{P}_{NL} \cdot \vec{E} \right)}{\partial t}$$

$$= \frac{1}{2} \frac{\partial \left(\vec{P}_{NL} \cdot \vec{E} \right)}{\partial t} - \vec{E} \cdot \frac{\partial \vec{P}_{NL}}{\partial t} + \vec{E} \cdot \nabla \times \vec{H} - \nabla \times \vec{E} \cdot \vec{H}$$

$$= \frac{1}{2} \frac{\partial \left(\vec{P}_{NL} \cdot \vec{E} \right)}{\partial t} - \vec{E} \cdot \frac{\partial \vec{P}_{NL}}{\partial t} - \nabla \cdot \left(\vec{E} \times \vec{H} \right) = -\nabla \cdot \vec{S} + \frac{1}{2} \frac{\partial \left(\vec{P}_{NL} \cdot \vec{E} \right)}{\partial t} - \vec{E} \cdot \frac{\partial \vec{P}_{NL}}{\partial t}$$

We substitute the nonlinear polarization term into the equations, assuming that the nonlinear polarization is in the direction of the electromagnetic field:

$$\vec{P}_{NL} = \varepsilon_0 \chi(z) \vec{E}^2(z,t) \hat{\vec{E}}$$

The terms $\vec{P}_{NL} \cdot \vec{E}$ and $\vec{E} \cdot \dfrac{\partial \vec{P}_{NL}}{\partial t}$ in Eq. (C.6) take the following form:

$$(C.7) \; \vec{P}_{NL} \cdot \vec{E} = \varepsilon_0 \chi(z) \vec{E}^3(z,t)$$

$$\vec{E} \cdot \frac{\partial \vec{P}_{NL}}{\partial t} = 2\varepsilon_0 \chi(z) \vec{E}^2(z,t) \frac{\partial E(z,t)}{\partial t}$$

Incorporation of Eq. (C.7) into Eq. (C.6) yields the following:

$$\frac{\partial u_e}{\partial t} = -\nabla \cdot \vec{S} + \frac{1}{2} \frac{\partial \left(\vec{P}_{NL} \cdot \vec{E} \right)}{\partial t} - \vec{E} \cdot \frac{\partial \vec{P}_{NL}}{\partial t} = -\nabla \cdot \vec{S} + \frac{1}{2} \frac{\partial \left(\varepsilon_0 \chi(z) \vec{E}^3(z,t) \right)}{\partial t} - 2\varepsilon_0 \chi(z) \vec{E}^2(z,t) \frac{\partial E(z,t)}{\partial t} \Rightarrow$$

$$\frac{\partial u_e}{\partial t} = -\nabla \cdot \vec{S} + \frac{3}{2} \varepsilon_0 \chi(z) \vec{E}^2(z,t) \frac{\partial E(z,t)}{\partial t} - 2\varepsilon_0 \chi(z) \vec{E}^2(z,t) \frac{\partial E(z,t)}{\partial t} \Rightarrow$$

$$(C.8) \; \frac{\partial u_e}{\partial t} = -\nabla \cdot \vec{S} - \frac{1}{2} \varepsilon_0 \chi(z) \vec{E}^2(z,t) \frac{\partial E(z,t)}{\partial t}$$

As the energy flow of the frequency generation process is in the z- direction, we are left only with the z-derivative of the poynting vector: $\nabla \cdot \vec{S} = \dfrac{\partial S(z,t)}{\partial z}$

$$(C.9) \; \frac{\partial u_e}{\partial t} + \frac{\partial S(z,t)}{\partial z} = -\frac{1}{2} \varepsilon_0 \chi(z) \vec{E}^2(z,t) \frac{\partial E(z,t)}{\partial t}$$

10.3.2 The energy conservation rule

Assume the electric field to be polarized along the $\hat{x}$ direction, and recall the electromagnetic field phasor defined in Eq. (B.8):

$$(C.10)\; E_x(z,t) = \int_{-\infty}^{+\infty} \frac{d\omega}{2\pi} \frac{1}{2}\left(A(z,\omega) + A^*(z,-\omega)\right)e^{-i\frac{\omega n(\omega)}{c}z}e^{i\omega t}$$

We need to calculate the pointing vector $\vec{S} = \vec{E}\times\vec{H}$. Using faraday law $\nabla\times\vec{E} = -\mu\dfrac{\partial\vec{H}}{\partial t}$ one obtain:

$$(C.11)\; \vec{H}(z,t) = -\frac{1}{\mu}\int\left(\nabla\times\vec{E}\right)dt = -\frac{1}{\mu}\int\left(0,\partial_z E_x,0\right)dt = -\frac{1}{\mu}\int\partial_z E_x dt\,\hat{y}$$

Substitute Eq. (C.10) into Eq. (C.11):

$$(C.12)\; H_y(z,t) = -\frac{1}{\mu}\int\partial_z E_x dt = -\frac{1}{\mu}\int\partial_z\left(\int_{-\infty}^{+\infty}\frac{d\omega}{2\pi}\frac{1}{2}\left(A(z,\omega)+A^*(z,-\omega)\right)e^{-i(\beta(\omega)z-\omega t)}\right)dt =$$

$$-\frac{1}{2\mu}\int\left(\int_{-\infty}^{+\infty}df\left(\partial_z A(z,\omega)+\partial_z A^*(z,-\omega)\right)e^{-i(\beta(\omega)z-\omega t)} - i\beta(\omega)\left(A(z,\omega)+A^*(z,-\omega)\right)e^{-i(\beta(\omega)z-\omega t)}\right)dt =$$

$$\frac{1}{2\mu}\int_{-\infty}^{+\infty}df\left(\frac{i}{\omega}\left(\partial_z A(z,\omega)+\partial_z A^*(z,-\omega)\right)+\frac{\beta(\omega)}{\omega}\left(A(z,\omega)+A^*(z,-\omega)\right)\right)e^{-i(\beta(\omega)z-\omega t)}$$

As pointed in section (3.5), the pointing vector $\vec{S} = \vec{E}\times\vec{H}$ is calculated without taking into account the nonlinear polarization contribution. The nonlinear contribution term induced by the derivatives $\partial_z A(z,\omega)$ and $\partial_z A^*(z,-\omega)$ is therefore dismissed. We are left with the following magnetic field:

$$(C.13)\; H_y(z,t) = \frac{1}{2\mu}\int_{-\infty}^{+\infty}df\frac{\beta(\omega)}{\omega}\left(A(z,\omega)+A^*(z,-\omega)\right)e^{-i(\beta(\omega)z-\omega t)}$$

The pointing vector is therefore given by:

$$\vec{S} = \vec{E}\times\vec{H} = E_x H_y\hat{z} = \underbrace{\int_{-\infty}^{+\infty}df\frac{1}{2}\left(A(z,\omega)+A^*(z,-\omega)\right)e^{-i(\beta(\omega)z-\omega t)}}_{E_x}\cdot\underbrace{\frac{1}{2\mu}\int_{-\infty}^{+\infty}df\frac{\beta(\omega)}{\omega}\left(A(z,\omega)+A^*(z,-\omega)\right)e^{-i(\beta(\omega)z-\omega t)}}_{H_y}$$

$$(C.14)\quad S_z = \frac{1}{4\mu}\int_{-\infty}^{+\infty}\int_{-\infty}^{+\infty}dfdf'e^{-i(\beta(\omega)+\beta(\omega'))z}e^{i(\omega+\omega')t}\left(A(z,\omega)+A^*(z,-\omega)\right)\cdot\frac{\beta(\omega')}{\omega'}\left(A(z,\omega')+A^*(z,-\omega')\right)$$

91

The units of S are $\dfrac{W}{m^2}$. In order to calculate the energy density of the electromagnetic field we integrate over time:

$$(C.15)\ E_d(z) = \int_{-\infty}^{+\infty} S_z(z,t)dt =$$

$$\frac{1}{4\mu}\int_{-\infty}^{+\infty}\int_{-\infty}^{+\infty}\int_{-\infty}^{+\infty} dfdf\,'e^{-i(\beta(\omega)+\beta(\omega'))z}e^{i(\omega+\omega')t}\left(A(z,\omega)+A^*(z,-\omega)\right)\cdot\frac{\beta(\omega')}{\omega'}\left(A(z,\omega')+A^*(z,-\omega')\right)dt$$

Recalling that $\dfrac{1}{2\pi}\displaystyle\int_{-\infty}^{+\infty} e^{i(\omega+\omega')t}dt = \delta(\omega+\omega')$, one obtains:

(C.16)

$$E_d(z) = \frac{1}{4\mu}\int_{-\infty}^{+\infty}\int_{-\infty}^{+\infty} d\omega\frac{d\omega'}{2\pi}\left(A(z,\omega)+A^*(z,-\omega)\right)e^{-i(\beta(\omega)+\beta(\omega'))z}\delta(\omega+\omega')\frac{\beta(\omega')}{\omega'}\left(A(z,\omega')+A^*(z,-\omega')\right)_{\omega'=-\omega}$$

$$E_d(z) = \frac{1}{4\mu}\int_{-\infty}^{+\infty}\frac{d\omega}{2\pi}\left(A(z,\omega)+A^*(z,-\omega)\right)e^{-i(\beta(\omega)+\beta(-\omega))z}\cdot\frac{-\beta(-\omega)}{\omega}\left(A(z,-\omega)+A^*(z,\omega)\right)$$

Recall that $\beta(\omega) = \dfrac{\omega n(|\omega|)}{c}$, hence $\dfrac{\beta(-\omega)}{\omega} = -\dfrac{\beta(\omega)}{\omega}$, so Eq. (C.16) reads:

$$(C.17)\ E_d(z) = \frac{1}{4\mu}\int_{-\infty}^{+\infty} df\left(A(z,\omega)+A^*(z,-\omega)\right)\cdot\frac{\beta(\omega)}{\omega}\left(A(z,-\omega)+A^*(z,\omega)\right)$$

$A(z,\omega)A^*(z,-\omega) = A(z,\omega)A(z,-\omega) = 0$ because $A(z,\omega)$ exist only for $\omega > 0$.

$$(C.18)\ E_d(z) = \frac{1}{4\mu}\int_{-\infty}^{+\infty} df\left(A(z,\omega)+A^*(z,-\omega)\right)\cdot\frac{\beta(\omega)}{\omega}\left(A(z,-\omega)+A^*(z,\omega)\right) = \int_{-\infty}^{+\infty} df\frac{\beta(\omega)}{4\omega\mu}\left(|A(z,\omega)|^2 + |A(z,-\omega)|^2\right)$$

$|A(z,-\omega)| = |A(z,\omega)|$, hence

$$(C.19)\ E_d(z) = \int_0^{+\infty} df\frac{\beta(\omega)}{4\omega\mu}2|A(z,\omega)|^2 = \int_0^{+\infty} df\frac{\beta(\omega)}{2\omega\mu}|A(z,\omega)|^2 = \int_0^{+\infty} df\frac{\omega n(\omega)}{2\omega\mu c}|A(z,\omega)|^2 = \int_0^{+\infty} df\frac{n(\omega)}{2\mu c}|A(z,\omega)|^2$$

$$\mu c = \mu\frac{1}{\sqrt{\mu\varepsilon_0}} = \sqrt{\frac{\mu}{\varepsilon_0}} = \eta_0\ ,\ \text{hence:}$$

$$(C.20)\ E_d^{A-C}(z) = \int_0^{+\infty} df\frac{n(\omega)}{2\eta_0}|A(z,\omega)|^2$$

The total electromagnetic flux is therefore given by:

$$(C.21) \int_{-\infty}^{+\infty} S_z(z,t)dt = \int_0^{+\infty} df \frac{n(\omega)}{2\eta_0} \left(\left|\tilde{A}_i(z,\omega)\right|^2 + \left|\tilde{A}_p(z,\omega)\right|^2 + \left|\tilde{A}_s(z,\omega)\right|^2 \right)$$

In the following it is demonstrated that the following energy term is conserved through the propagation:

$$E_d(z) = \int_0^{+\infty} df \frac{n(\omega)}{2\eta_0} \left(\left|\tilde{A}_i(z,\omega)\right|^2 + \left|\tilde{A}_p(z,\omega)\right|^2 + \left|\tilde{A}_s(z,\omega)\right|^2 \right)$$

In other words $\frac{dE_d(z)}{dz} = 0$.

$$(C.22) \frac{dE_d(z)}{dz} = \int_0^{+\infty} \frac{df}{2\mu c} \left(\frac{d\left|\tilde{A}_p(z,\omega)\right|^2}{dz} n(\omega) + \frac{d\left|\tilde{A}_s(z,\omega)\right|^2}{dz} n(\omega) + \frac{d\left|\tilde{A}_i(z,\omega)\right|^2}{dz} n(\omega) \right)$$

The equations describing the propagation are (Eq. set. (3.13)):

$$\partial_z \tilde{A}_s(z,\omega) + i\beta(\omega)\tilde{A}_s(z,\omega) = -i\frac{\omega}{c}\frac{\chi(z)}{n(\omega)}\tilde{A}_i(z,\omega) * \tilde{A}_p(z,\omega)$$

$$\partial_z \tilde{A}_p(z,\omega) + i\beta(\omega)\tilde{A}_p(z,\omega) = -i\frac{\omega}{c}\frac{\chi(z)}{n(\omega)}\tilde{A}_s(z,\omega) * \tilde{A}_i^*(z,-\omega)$$

$$\partial_z \tilde{A}_i(z,\omega) + i\beta(\omega)\tilde{A}_i(z,\omega) = -i\frac{\omega}{c}\frac{\chi(z)}{n(\omega)}\tilde{A}_s(z,\omega) * \tilde{A}_p^*(z,-\omega)$$

For ease we write from now on: $\tilde{A}_\beta(z,\omega) = \beta(z,\omega)$, hence:

$$(C.23)\, \partial_z S(z,\omega) + i\beta(\omega)S(z,\omega) = -i\frac{\omega}{c}\frac{\chi(z)}{n(\omega)}I(z,\omega) * P(z,\omega)$$

$$\partial_z P(z,\omega) + i\beta(\omega)P(z,\omega) = -i\frac{\omega}{c}\frac{\chi(z)}{n(\omega)}S(z,\omega) * I^*(z,-\omega)$$

$$\partial_z I(z,\omega) + i\beta(\omega)I(z,\omega) = -i\frac{\omega}{c}\frac{\chi(z)}{n(\omega)}S(z,\omega) * P^*(z,-\omega)$$

Start with the Pump:

(C.24)

$$\frac{d\left|P(z,\omega)\right|^2}{dz}n(\omega) = \frac{d\left(P(z,\omega)P^*(z,\omega)\right)}{dz}n(\omega) = \left[\frac{dP(z,\omega)}{dz}P^*(z,\omega) + \frac{dP^*(z,\omega)}{dz}P(z,\omega)\right]n(\omega) =$$

$$= \left[\begin{array}{l}\left(-i\dfrac{\omega}{c}\dfrac{\chi(z)}{n(\omega)}S(z,\omega)*I^*(z,-\omega) - i\beta(\omega)P(z,\omega)\right)P^*(z,\omega) + \\[2mm] \left(+i\dfrac{\omega}{c}\dfrac{\chi(z)}{n(\omega)}S^*(z,\omega)*I(z,-\omega) - i\beta(\omega)P^*(z,\omega)\right)P(z,\omega)\end{array}\right]n(\omega) =$$

$$= -i\frac{\omega}{c}\chi(z)\left(S(z,\omega)*I^*(z,-\omega)P^*(z,\omega) - S^*(z,\omega)*I(z,-\omega)P(z,\omega)\right)$$

By repeating the same procedure to both the signal and idler pulses one obtain:

$$(C.25)\quad \frac{dE_d(z)}{dz} = \frac{-i\chi(z)}{4\pi\mu c^2}\int_0^{+\infty}\omega\left(\begin{array}{l}I(z,\omega)*P(z,\omega)S^*(z,\omega) - I^*(z,\omega)*P^*(z,\omega)S(z,\omega) + \\ S(z,\omega)*I^*(z,-\omega)P^*(z,\omega) - S^*(z,\omega)*I(z,-\omega)P(z,\omega) + \\ S(z,\omega)*P^*(z,-\omega)I^*(z,\omega) - S^*(z,\omega)*P(z,-\omega)I(z,\omega)\end{array}\right)d\omega$$

All the signals written here exist only for $\omega > 0$ so the lower bound can be stretched:

$$(C.26)\quad \frac{dE_d(z)}{dz} = \frac{-i\chi(z)}{4\pi\mu c^2}\int_{-\infty}^{+\infty}\omega\left(\begin{array}{l}I(z,\omega)*P(z,\omega)S^*(z,\omega) - I^*(z,\omega)*P^*(z,\omega)S(z,\omega) + \\ S(z,\omega)*I^*(z,-\omega)P^*(z,\omega) - S^*(z,\omega)*I(z,-\omega)P(z,\omega) + \\ S(z,\omega)*P^*(z,-\omega)I^*(z,\omega) - S^*(z,\omega)*P(z,-\omega)I(z,\omega)\end{array}\right)d\omega$$

Define

$$(C.27)\quad \Xi = \int_{-\infty}^{+\infty}\omega\left(I(z,\omega)*P(z,\omega)S^*(z,\omega) - S^*(z,\omega)*I(z,-\omega)P(z,\omega) - S^*(z,\omega)*P(z,-\omega)I(z,\omega)\right)d\omega$$

Therefore Eq. (C.26) can be written as:

$$(C.28)\quad \frac{dE_d(z)}{dz} = \frac{-i\chi(z)}{4\pi\mu c^2}\left(\Xi - \Xi^*\right)$$

94

Let's start:

$$\text{(C.29)} \int\limits_{-\infty}^{+\infty} \omega I(z,\omega)*P(z,\omega)S^*(z,\omega)d\omega = \int\limits_{-\infty}^{+\infty}\int\limits_{-\infty}^{+\infty} \omega I(z,\omega')P(z,\omega-\omega')S^*(z,\omega)d\omega d\omega' \Bigg|_{\omega-\omega'=\omega''} =$$

$$= \int\limits_{-\infty}^{+\infty}\int\limits_{-\infty}^{+\infty} (\omega'+\omega'') I(z,\omega')P(z,\omega'')S^*(z,\omega''+\omega')d\omega d\omega' =$$

$$= \underbrace{\int\limits_{-\infty}^{+\infty}\int\limits_{-\infty}^{+\infty} \omega' I(z,\omega')P(z,\omega'')S^*(z,\omega''+\omega')d\omega d\omega'}_{A} + \underbrace{\int\limits_{-\infty}^{+\infty}\int\limits_{-\infty}^{+\infty} \omega'' I(z,\omega')P(z,\omega'')S^*(z,\omega''+\omega')d\omega d\omega'}_{B}$$

Continue with term A:

$$\text{(C.30)} \int\limits_{-\infty}^{+\infty}\int\limits_{-\infty}^{+\infty} \omega' I(z,\omega')P(z,\omega'')S^*(z,\omega''+\omega')d\omega d\omega' \Bigg|_{\omega=-\omega''} = \int\limits_{-\infty}^{+\infty}\int\limits_{-\infty}^{+\infty} \omega' I(z,\omega')P(z,-\omega)S^*(z,\omega'-\omega)d\omega d\omega' =$$

$$= \int\limits_{-\infty}^{+\infty} \omega' I(z,\omega') P(z,-\omega)*S^*(z,\omega)\Big|_{\omega=\omega'} d\omega' = \int\limits_{-\infty}^{+\infty} \omega I(z,\omega)P(z,-\omega)*S^*(z,\omega)d\omega$$

Term B:

$$\text{(C.31)} \int\limits_{-\infty}^{+\infty}\int\limits_{-\infty}^{+\infty} \omega'' I(z,\omega')P(z,\omega'')S^*(z,\omega''+\omega')d\omega d\omega' \Bigg|_{\omega=-\omega'} = \int\limits_{-\infty}^{+\infty}\int\limits_{-\infty}^{+\infty} \omega'' P(z,\omega'')I(z,-\omega)S^*(z,\omega''-\omega)d\omega d\omega' =$$

$$= \int\limits_{-\infty}^{+\infty} \omega'' P(z,\omega'') I(z,-\omega)*S^*(z,\omega)\Big|_{\omega=\omega''} d\omega'' = \int\limits_{-\infty}^{+\infty} \omega P(z,\omega)I(z,-\omega)*S^*(z,\omega)d\omega$$

Substituting Eq. (C.30) and Eq. (C.31) into Eq. (C.29) yields:

$$\text{(C.32)} \int\limits_{-\infty}^{+\infty} \omega I(z,\omega)*P(z,\omega)S^*(z,\omega)d\omega = \int\limits_{-\infty}^{+\infty} \omega I(z,\omega)P(z,-\omega)*S^*(z,\omega)d\omega + \int\limits_{-\infty}^{+\infty} \omega P(z,\omega)I(z,-\omega)*S^*(z,\omega)d\omega$$

$$= \int\limits_{-\infty}^{+\infty} \Big(\omega I(z,\omega)*P(z,\omega)S^*(z,\omega) - \omega I(z,\omega)P(z,-\omega)*S^*(z,\omega) - \omega P(z,\omega)I(z,-\omega)*S^*(z,\omega) \Big) d\omega = 0 \Rightarrow$$

$$\Xi = 0$$

In the following we proved that $\Xi = 0$, hence $\dfrac{dE_d(z)}{dz} = \dfrac{-i\chi(z)}{4\pi\mu c^2}\left(\Xi - \Xi^*\right) = 0.$

$$\text{(C.33)} \frac{dE_d(z)}{dz} = \int\limits_{0}^{+\infty} \frac{df}{2\mu c} \left(\frac{d\left|A_p(z,\omega)\right|^2}{dz} n(\omega) + \frac{d\left|A_s(z,\omega)\right|^2}{dz} n(\omega) + \frac{d\left|A_i(z,\omega)\right|^2}{dz} n(\omega) \right) = 0$$

10.4 Appendix D- DFG compression scheme optimization

10.4.1 DFG compression feasibility dependence with signal chirp

We recall Φ_{opt} defined in Eq. (7.6) $\Phi_{opt} = SLM_{compensation}\left(L_{opt}\right)$, where L_{opt} are the discrete set of silicone lengths for which the phase range needed to be compensated by the SLM, defined in Eq. (7.5) $SLM_{compensation} = \max\left(\sphericalangle Idler\ Phase\right)_{1.8\,\mu m < \lambda_i < 5.5\,\mu m} - \min\left(\sphericalangle Idler\ Phase\right)_{1.8\,\mu m < \lambda_i < 5.5\,\mu m}$ is minimal.

Numerical trial and error examinations show that good SLM compensation can be done whenever $\Phi_{opt} \leq 350[\text{Rad}]$, hence, we used Φ_{opt} as a measure to the compression feasibility and simulated it for various values of signal chirp and air lengths before and after the nonlinear crystal.

The results are presented in the following tables, with the highlighted colors defined below:

Φ_{opt} value[Rad]	Highlighted color
$\Phi_{opt} > 350[\text{Rad}]$	
$200[\text{Rad}] \leq \Phi_{opt} \leq 350[\text{Rad}]$	
$100[\text{Rad}] \leq \Phi_{opt} < 200[\text{Rad}]$	
$\Phi_{opt} < 100[\text{Rad}]$	

The greener the color is, the compensation scheme is better.

Observing the tables below several conclusions can be deduced:

- It is easier to compress the MIR pulse in the regime $C_s \in [-4 \cdot 10^{-27}\ \ 1 \cdot 10^{-27}][s^2]$.
- For a given air propagation lengths, the shorter the crystal the compensation is better (less phase to compensate).
- The transform limit case is not inferior in terms of compensation vs. other signal chirps.

Chirp 10^-25[s^2]	Lair	10[m]			Lair	8[m]			Lair	6[m]	
	-5	L_opt[mm]	Delta_SLM[rad]	Phi_opt[rad]	L_opt[mm]	Delta_SLM[rad]	Phi_opt[rad]	L_opt[mm]	Delta_SLM[rad]	Phi_opt[rad]
		17.56	431.7	456.1	19.15	413.1	431.5	16.43	493.6	485.5
L_air_before		21.88	337.6	369.7	23.47	338.8	333.6	20.75	361.8	387.1
3[m]		26.20	281.0	280.5	27.80	223.1	238.3	25.08	281.3	290.5
		30.52	179.4	187.3	32.12	121.5	148.8	29.40	207.2	203.7
		34.84	47.9	103.2	36.43	35.3	91.1	33.72	76.6	130.2
		39.15	29.2	102.9				38.03	33.7	78.6
	-4	L_opt[mm]	Delta_SLM[rad]	Phi_opt[rad]	L_opt[mm]	Delta_SLM[rad]	Phi_opt[rad]	L_opt[mm]	Delta_SLM[rad]	Phi_opt[rad]
		13.23	408.7	439.4	10.51	488.1	493.4	12.11	453.8	465.0
L_air_before		17.55	320.6	341.6	14.83	382.1	397.7	16.43	321.3	378.4
3[m]		21.87	213.2	246.2	19.15	273.2	311.9	20.74	244.2	287.0
		26.20	112.5	166.8	23.47	184.5	229.7	25.07	172.9	193.2
		30.51	52.8	97.5	27.79	113.7	143.6	29.39	72.6	107.6
		34.83	21.6	105.4	32.11	19.8	84.4	33.70	15.9	95.8
		39.15	123.6	188.7	36.43	17.2	128.0	38.03	24.5	158.3
	-3	L_opt[mm]	Delta_SLM[rad]	Phi_opt[rad]	L_opt[mm]	Delta_SLM[rad]	Phi_opt[rad]	L_opt[mm]	Delta_SLM[rad]	Phi_opt[rad]
		13.23	260.6	338.0	10.50	339.7	391.9	12.10	270.5	347.8
		17.54	183.1	241.9	14.82	219.0	294.6	16.42	212.4	254.3
L_air_before		21.86	94.1	150.6	19.14	142.8	200.5	20.74	126.0	174.2
3[m]		26.19	25.2	92.5	23.46	72.2	113.8	25.06	46.5	101.5
		30.51	16.9	123.0	27.78	19.4	77.5	29.38	29.8	98.9
		34.83	48.1	198.4	32.11	27.8	157.7	33.70	30.8	181.1
		39.15	81.8	295.2	36.42	118.2	243.9	38.02	118.1	267.5
	-2	L_opt[mm]	Delta_SLM[rad]	Phi_opt[rad]	L_opt[mm]	Delta_SLM[rad]	Phi_opt[rad]	L_opt[mm]	Delta_SLM[rad]	Phi_opt[rad]
		13.22	177.2	214.8	10.50	226.1	280.0	12.09	210.0	247.4
		17.54	102.9	138.1	14.81	161.9	195.4	16.41	130.6	155.4
L_air_before		21.85	25.9	75.2	19.13	86.8	107.5	20.73	45.3	93.6
3[m]		26.18	10.8	137.8	23.45	10.5	94.0	25.06	16.5	120.1
		30.50	67.2	222.1	27.78	9.7	160.7	29.38	54.7	194.0
		34.82	94.6	309.4	32.10	55.7	245.7	33.70	56.8	290.3
		39.14	341.9	397.9	36.42	226.9	340.6	38.02	217.3	388.6
	-1	L_opt[mm]	Delta_SLM[rad]	Phi_opt[rad]	L_opt[mm]	Delta_SLM[rad]	Phi_opt[rad]	L_opt[mm]	Delta_SLM[rad]	Phi_opt[rad]
		13.21	118.2	113.4	10.49	187.2	161.9	12.09	136.3	144.9
		17.52	27.2	86.5	14.80	101.5	101.0	16.40	48.5	75.3
L_air_before		21.85	28.5	148.5	19.12	11.1	108.5	20.72	28.3	131.1
3[m]		26.18	44.1	239.8	23.44	5.2	191.2	25.05	11.5	214.6
		30.50	81.4	337.0	27.77	43.1	277.8	29.37	57.4	301.5
		34.81	347.7	431.5	32.09	127.2	366.0	33.69	183.1	389.7
					36.41	341.8	455.1	38.01	391.9	486.4
	TL	L_opt[mm]	Delta_SLM[rad]	Phi_opt[rad]	L_opt[mm]	Delta_SLM[rad]	Phi_opt[rad]	L_opt[mm]	Delta_SLM[rad]	Phi_opt[rad]
		13.20	4.4	89.3	10.48	89.6	83.5	12.07	35.8	81.8
		17.52	29.1	169.8	14.80	10.0	111.2	16.40	17.2	143.9
L_air_before		21.84	37.4	255.3	19.12	13.1	193.0	20.72	19.1	234.8
3[m]		26.17	34.2	342.9	23.44	31.9	283.8	25.05	37.0	331.8
		30.49	251.8	433.9	27.77	114.1	382.5	29.36	164.8	423.1
					32.09	267.4	482.0			
	1	L_opt[mm]	Delta_SLM[rad]	Phi_opt[rad]	L_opt[mm]	Delta_SLM[rad]	Phi_opt[rad]	L_opt[mm]	Delta_SLM[rad]	Phi_opt[rad]
		13.20	25.3	185.2	10.47	3.9	139.5	12.07	17.6	162.3
		17.52	14.5	280.1	14.79	18.8	223.2	16.39	17.9	246.7
L_air_before 3[m]		21.83	83.4	375.3	19.11	43.4	310.4	20.71	39.5	334.1
		26.16	165.1	464.7	23.43	114.4	399.0	25.04	131.5	427.8
					27.76	218.0	488.3			
	2	L_opt[mm]	Delta_SLM[rad]	Phi_opt[rad]	L_opt[mm]	Delta_SLM[rad]	Phi_opt[rad]	L_opt[mm]	Delta_SLM[rad]	Phi_opt[rad]
		13.19	25.6	288.2	10.47	13.7	228.0	12.07	9.3	275.8
L_air_before 3[m]		17.51	52.5	376.1	14.79	14.9	325.1	16.38	57.8	367.4
		21.83	199.5	475.5	19.11	114.7	423.9	20.70	151.3	456.6
	3	L_opt[mm]	Delta_SLM[rad]	Phi_opt[rad]	L_opt[mm]	Delta_SLM[rad]	Phi_opt[rad]	L_opt[mm]	Delta_SLM[rad]	Phi_opt[rad]
		13.18	53.5	409.7	10.46	34.0	344.7	12.06	27.3	370.8
L_air_before 3[m]		17.50	200.7	499.1	14.78	53.1	433.3	16.38	199.2	470.3
	4	L_opt[mm]	Delta_SLM[rad]	Phi_opt[rad]	L_opt[mm]	Delta_SLM[rad]	Phi_opt[rad]	L_opt[mm]	Delta_SLM[rad]	Phi_opt[rad]
L_air_before 3[m]		0.00	0.0	0.0	10.46	86.8	466.2	12.05	136.2	491.0

Chirp 10^-25[s^2]	Lair 10[m]			Lair 8[m]			Lair 6[m]		
-5	L_opt[mm	Delta_SLM[rad]	Phi_opt[rad]	L_opt[mm	Delta_SLM[rad]	Phi_opt[ra	L_opt[mm	Delta_SLM[rad]	Phi_opt[rad]
	18.92	388.50	431.63	16.19	480.43	495.96	17.79	440.00	451.19
	23.23	298.08	343.67	20.51	377.17	397.35	22.11	282.73	353.38
	27.56	205.85	247.78	24.83	244.50	300.27	26.44	213.60	262.59
	31.88	125.78	157.07	29.16	177.15	206.68	30.76	130.01	183.01
	36.20	34.38	94.47	33.48	98.36	122.71	35.07	102.83	108.59
L_air_before 4[m]				37.79	66.94	70.99	39.39	65.50	92.01
-4	L_opt[mm	Delta_SLM[rad]	Phi_opt[rad]	L_opt[mm	Delta_SLM[rad]	Phi_opt[ra	L_opt[mm	Delta_SLM[rad]	Phi_opt[rad]
	14.59	373.00	404.83	11.87	458.37	460.45	13.47	410.76	440.56
	18.91	265.08	307.74	16.19	288.77	373.54	17.78	335.11	349.87
	23.23	170.82	223.89	20.51	244.11	288.92	22.10	221.45	253.61
	27.56	94.02	147.84	24.82	153.07	201.77	26.43	124.87	162.16
	31.87	36.41	77.04	29.15	70.08	114.72	30.75	43.27	95.49
	36.19	29.77	129.58	33.47	23.03	95.74	35.06	22.05	119.87
L_air_before 4[m]				37.79	67.30	152.55	39.39	151.04	189.15
	L_opt[mm	Delta_SLM[rad]	Phi_opt[rad]	L_opt[mm	Delta_SLM[rad]	Phi_opt[ra	L_opt[mm	Delta_SLM[rad]	Phi_opt[rad]
-3	10.27	362.28	399.77	11.86	357.18	357.06	13.46	311.30	315.44
	14.58	317.44	303.62	16.18	288.95	260.77	17.78	235.58	231.98
	18.90	234.48	208.81	20.50	174.48	168.83	22.10	133.89	154.83
	23.22	126.92	120.75	24.82	85.96	106.48	26.42	52.22	77.61
	27.54	32.25	82.53	29.14	72.69	100.11	30.74	29.61	122.63
	31.87	31.31	147.01	33.46	102.63	182.82	35.06	201.28	206.30
L_air_before 4[m]	36.19	155.48	234.02	37.78	334.22	269.60	39.38	523.53	293.26
	L_opt[mm	Delta_SLM[rad]	Phi_opt[rad]	L_opt[mm	Delta_SLM[rad]	Phi_opt[ra	L_opt[mm	Delta_SLM[rad]	Phi_opt[rad]
-2	10.26	325.95	275.07	11.85	314.69	256.04	13.45	258.59	213.96
	14.58	212.00	193.58	16.17	208.91	163.01	17.77	150.69	124.85
	18.89	133.97	114.40	20.49	92.96	86.53	22.08	70.36	79.75
	23.21	13.99	85.74	24.81	42.75	110.70	26.42	23.58	143.32
	27.54	23.42	162.11	29.14	23.76	185.31	30.74	103.99	229.63
	31.86	81.07	247.47	33.46	164.92	278.58	35.05	484.29	326.31
L_air_before 4[m]	36.18	459.09	335.13	37.78	619.50	377.19	39.37	997.20	415.27
-1	L_opt[mm	Delta_SLM[rad]	Phi_opt[rad]	L_opt[mm	Delta_SLM[rad]	Phi_opt[ra	L_opt[mm	Delta_SLM[rad]	Phi_opt[rad]
	10.25	263.17	169.58	11.85	202.68	138.64	13.44	185.64	118.49
	14.57	106.58	96.89	16.16	83.05	73.27	17.76	28.54	84.51
	18.88	9.79	109.53	20.48	12.21	132.21	22.08	49.38	155.03
	23.21	24.62	180.74	24.80	69.61	216.21	26.41	80.22	239.71
	27.54	138.48	275.83	29.13	163.71	303.36	30.73	216.39	327.03
L_air_before 4[m]	31.85	380.49	368.09	33.45	601.11	391.76	35.05	770.85	423.32
TL	L_opt[mm	Delta_SLM[rad]	Phi_opt[rad]	L_opt[mm	Delta_SLM[rad]	Phi_opt[ra	L_opt[mm	Delta_SLM[rad]	Phi_opt[rad]
	10.24	80.98	78.60	11.84	27.37	90.17	13.43	10.37	102.31
	14.56	4.83	112.12	16.16	16.44	134.55	17.76	23.02	176.20
	18.88	18.86	194.34	20.48	27.47	223.02	22.08	75.88	270.82
	23.20	31.24	280.51	24.80	132.98	320.33	26.40	154.16	359.77
L_air_before 4[m]	27.53	172.49	371.11	29.13	387.88	419.16	30.72	633.26	448.89
1	L_opt[mm	Delta_SLM[rad]	Phi_opt[rad]	L_opt[mm	Delta_SLM[rad]	Phi_opt[ra	L_opt[mm	Delta_SLM[rad]	Phi_opt[rad]
	10.24	80.98	78.60	11.84	27.37	90.17	13.43	10.37	102.31
	14.56	31.33	220.67	16.15	32.11	248.36	17.75	77.44	271.95
	18.87	95.40	312.30	20.47	96.79	335.97	22.07	164.46	365.22
L_air_before 4[m]	23.19	154.46	401.04	24.79	338.96	424.70	26.40	338.22	464.78
	L_opt[mm	Delta_SLM[rad]	Phi_opt[rad]	L_opt[mm	Delta_SLM[rad]	Phi_opt[ra	L_opt[mm	Delta_SLM[rad]	Phi_opt[rad]
2	10.23	14.48	226.95	11.83	31.07	264.22	13.42	13.92	304.57
	14.55	59.01	313.84	16.15	10.02	361.87	17.74	67.03	392.99
L_air_before 4[m]	18.87	136.37	412.80	20.46	192.72	458.68	22.06	274.50	482.28
3	L_opt[mm	Delta_SLM[rad]	Phi_opt[rad]	L_opt[mm	Delta_SLM[rad]	Phi_opt[ra	L_opt[mm	Delta_SLM[rad]	Phi_opt[rad]
L_air_before 4[m]	10.22	67.57	346.33	11.82	92.58	370.00	13.42	97.19	407.72

10.4.2 Signal conversion efficiency dependence with signal chirp, after SLM compensation

We display the conversion efficiency dependence with the signal chirp.

We define the following quantities:

- $\eta_E = \dfrac{E_{Idler}(z_f)}{E_{Signal}(z_i)}$ - the DFG conversion efficiency.

- $\sigma_\eta = std(\eta(\lambda))$ - A measure to the frequency conversion dependence with wavelength.

- τ_s is the signal duration (10%-90% knife edge definition) of the signal pulse (modulated by the SLM) in the beginning of the crystal.

The simulated quantities are exhibited for different values of signal chirp, and for a span of air lengths before and after the nonlinear crystal. The results are presented in the following tables, with the highlighted colors defined below:

$\eta_E = \dfrac{E_{Idler}(z_f)}{E_{Signal}(z_i)}[\%]$	Highlighted color
$25\% < \eta_E$	
$20\% \le \eta_E < 25\%$	
$15\% \le \eta_E < 20\%$	
$\eta_E < 15\%$	

Several conclusions can be deduced from the tables below:

- The longer the signal goes through the air, the efficiency deteriorates.
- For a given air propagation lengths, the shorter the crystal the efficiency is better.
- For a given air propagation lengths, the longer the crystal the better the conversion efficiency vs lambda: $std(\eta(\lambda))$ is lower.
- The transform limit case is not inferior in terms of efficiency vs. other signal chirps.
- $C_s \in [-2 \cdot 10^{-27} \ 1 \cdot 10^{-27}][s^2]$ is good range in terms of efficiency.

Chirp 10^-25[s^2]	Lair	10[m]			Lair	8[m]			Lair	6[m]		
-5	L_opt[mm]	Tau_s[ps]	Eta[%]	std(Eta)	L_opt[mm]	Tau_s[ps]	Eta[%]	std(Eta)	L_opt[mm]	Tau_s[ps]	Eta[%]	std(Eta)
	18.92	4.81	19%	0.23	16.19	6.20	20%	0.23	17.79	4.71	19%	0.23
	23.23	4.84	17%	0.22	20.51	4.75	18%	0.23	22.11	4.86	18%	0.22
	27.56	5.08	16%	0.22	24.83	4.95	17%	0.22	26.44	5.09	17%	0.22
	31.88	5.27	16%	0.21	29.16	5.17	16%	0.22	30.76	5.30	16%	0.22
	36.20	5.58	16%	0.22	33.48	5.41	16%	0.22	35.07	5.44	16%	0.22
L_air_before 4[m]					37.79	5.62	16%	0.22	39.39	5.78	16%	0.23
-4	L_opt[mm]	Tau_s[ps]	Eta[%]	std(Eta)	L_opt[mm]	Tau_s[ps]	Eta[%]	std(Eta)	L_opt[mm]	Tau_s[ps]	Eta[%]	std(Eta)
	14.59	3.72	20%	0.22	11.87	4.11	23%	0.24	13.47	4.15	21%	0.23
	18.91	3.82	18%	0.21	16.19	3.78	19%	0.22	17.78	3.74	18%	0.21
	23.23	4.06	16%	0.20	20.51	3.95	17%	0.21	22.10	3.91	16%	0.20
	27.56	4.31	16%	0.20	24.82	4.05	15%	0.20	26.43	4.16	16%	0.20
	31.87	4.46	15%	0.20	29.15	4.29	15%	0.20	30.75	4.46	15%	0.20
	36.19	4.92	16%	0.22	33.47	4.62	16%	0.21	35.06	4.71	15%	0.21
L_air_before 4[m]					37.79	5.17	16%	0.22	39.39	5.40	16%	0.22
	L_opt[mm]	Tau_s[ps]	Eta[%]	std(Eta)	L_opt[mm]	Tau_s[ps]	Eta[%]	std(Eta)	L_opt[mm]	Tau_s[ps]	Eta[%]	std(Eta)
-3	10.27	2.96	27%	0.26	11.86	2.84	22%	0.22	13.46	2.86	20%	0.21
	14.58	2.78	18%	0.20	16.18	2.85	17%	0.19	17.78	2.94	17%	0.19
	18.90	2.92	16%	0.18	20.50	3.03	16%	0.18	22.10	3.15	16%	0.18
	23.22	3.17	15%	0.18	24.82	3.32	15%	0.18	26.42	3.32	15%	0.17
	27.54	3.38	14%	0.17	29.14	3.66	15%	0.18	30.74	3.90	15%	0.19
	31.87	4.08	15%	0.20	33.46	4.36	15%	0.20	35.06	4.64	15%	0.20
L_air_before 4[m]	36.19	4.79	15%	0.20	37.78	5.05	15%	0.20	39.38	5.20	14%	0.20
	L_opt[mm]	Tau_s[ps]	Eta[%]	std(Eta)	L_opt[mm]	Tau_s[ps]	Eta[%]	std(Eta)	L_opt[mm]	Tau_s[ps]	Eta[%]	std(Eta)
-2	10.26	2.02	27%	0.25	11.85	1.92	22%	0.21	13.45	1.95	19%	0.19
	14.58	2.03	18%	0.18	16.17	1.96	16%	0.17	17.77	2.06	16%	0.16
	18.89	2.05	15%	0.16	20.49	2.18	15%	0.16	22.08	2.35	14%	0.15
	23.21	2.56	14%	0.16	24.81	2.84	15%	0.16	26.42	3.10	15%	0.17
	27.54	3.28	14%	0.17	29.14	3.56	14%	0.18	30.74	3.82	15%	0.18
	31.86	4.03	14%	0.18	33.46	4.26	14%	0.18	35.05	4.54	14%	0.18
L_air_before 4[m]	36.18	4.58	14%	0.18	37.78	4.74	13%	0.18	39.37	5.03	13%	0.18
-1	L_opt[mm]	Tau_s[ps]	Eta[%]	std(Eta)	L_opt[mm]	Tau_s[ps]	Eta[%]	std(Eta)	L_opt[mm]	Tau_s[ps]	Eta[%]	std(Eta)
	10.25	1.15	26%	0.23	11.85	1.16	21%	0.19	13.44	1.10	17%	0.16
	14.57	1.21	17%	0.15	16.16	1.36	15%	0.14	17.76	1.59	15%	0.14
	18.88	1.77	14%	0.14	20.48	2.03	14%	0.14	22.08	2.31	14%	0.15
	23.21	2.54	14%	0.16	24.80	2.81	14%	0.16	26.41	3.09	14%	0.16
	27.54	3.26	14%	0.16	29.13	3.52	13%	0.16	30.73	3.72	13%	0.16
L_air_before 4[m]	31.85	3.91	13%	0.16	33.45	4.11	13%	0.16	35.05	4.28	13%	0.16
TL	L_opt[mm]	Tau_s[ps]	Eta[%]	std(Eta)	L_opt[mm]	Tau_s[ps]	Eta[%]	std(Eta)	L_opt[mm]	Tau_s[ps]	Eta[%]	std(Eta)
	10.24	0.71	25%	0.23	11.84	0.85	20%	0.18	13.43	1.01	16%	0.14
	14.56	1.15	16%	0.14	16.16	1.36	15%	0.14	17.76	1.61	15%	0.15
	18.88	1.79	14%	0.14	20.48	2.06	14%	0.15	22.08	2.35	14%	0.15
	23.20	2.53	13%	0.15	24.80	2.78	13%	0.15	26.40	3.03	13%	0.15
L_air_before 4[m]	27.53	3.16	13%	0.15	29.13	3.39	12%	0.15	30.72	3.62	12%	0.15
1	L_opt[mm]	Tau_s[ps]	Eta[%]	std(Eta)	L_opt[mm]	Tau_s[ps]	Eta[%]	std(Eta)	L_opt[mm]	Tau_s[ps]	Eta[%]	std(Eta)
	10.24	1.13	25%	0.23	11.83	1.36	20%	0.18	13.43	1.51	16%	0.16
	14.56	1.57	16%	0.16	16.15	1.83	14%	0.15	17.75	1.99	14%	0.15
	18.87	2.18	13%	0.15	20.47	2.33	13%	0.15	22.07	2.50	13%	0.15
L_air_before 4[m]	23.19	2.66	12%	0.15	24.79	2.86	12%	0.15	26.40	3.04	12%	0.15
	L_opt[mm]	Tau_s[ps]	Eta[%]	std(Eta)	L_opt[mm]	Tau_s[ps]	Eta[%]	std(Eta)	L_opt[mm]	Tau_s[ps]	Eta[%]	std(Eta)
2	10.23	2.01	24%	0.23	11.83	2.15	19%	0.19	13.42	2.38	16%	0.17
	14.55	2.49	15%	0.16	16.15	2.65	14%	0.16	17.74	2.95	13%	0.16
L_air_before 4[m]	18.87	3.60	13%	0.16	20.46	3.55	12%	0.16	22.06	3.49	12%	0.16
3	L_opt[mm]	Tau_s[ps]	Eta[%]	std(Eta)	L_opt[mm]	Tau_s[ps]	Eta[%]	std(Eta)	L_opt[mm]	Tau_s[ps]	Eta[%]	std(Eta)
L_air_before 4[m]	10.22	2.91	22%	0.22	11.82	3.56	18%	0.19	13.42	4.96	15%	0.18

Efficient adiabatic frequency conversions for ultrashort pulses

Chirp 10^-25[s^2]	Lair	10[m]			Lair	8[m]			Lair	6[m]		
-5	L_opt[mm]	Tau_s[ps]	Eta[%]	std(Eta)	L_opt[mm]	Tau_s[ps]	Eta[%]	std(Eta)	L_opt[mm]	Tau_s[ps]	Eta[%]	std(Eta)
	17.56	6.02	28%	0.28	19.15	4.90	27%	0.28	16.43	6.41	28%	0.29
L_air_before 3[m]	21.88	4.92	27%	0.28	23.47	4.86	26%	0.27	20.75	4.74	27%	0.28
	26.20	4.96	25%	0.27	27.80	5.05	24%	0.27	25.08	4.97	25%	0.27
	30.52	5.18	24%	0.26	32.12	5.32	24%	0.27	29.40	5.23	25%	0.27
	34.84	5.46	24%	0.27	36.43	5.48	23%	0.27	33.72	5.46	24%	0.27
	39.15	5.70	23%	0.27	0.00	0.00	0%	0.00	38.03	5.68	23%	0.27
-4	L_opt[mm]	Tau_s[ps]	Eta[%]	std(Eta)	L_opt[mm]	Tau_s[ps]	Eta[%]	std(Eta)	L_opt[mm]	Tau_s[ps]	Eta[%]	std(Eta)
	13.23	4.76	30%	0.29	10.51	5.11	35%	0.32	12.11	5.25	31%	0.30
L_air_before 3[m]	17.55	3.73	27%	0.27	14.83	3.88	29%	0.28	16.43	3.76	28%	0.28
	21.87	3.94	26%	0.26	19.15	3.85	27%	0.27	20.74	3.80	25%	0.26
	26.20	4.22	25%	0.26	23.47	4.10	25%	0.26	25.07	4.07	24%	0.25
	30.51	4.38	23%	0.25	27.79	4.20	24%	0.25	29.39	4.35	24%	0.26
	34.83	4.71	23%	0.26	32.11	4.51	23%	0.26	33.70	4.54	23%	0.26
	39.15	5.44	22%	0.27	36.43	4.98	23%	0.27	38.03	5.23	23%	0.27
-3	L_opt[mm]	Tau_s[ps]	Eta[%]	std(Eta)	L_opt[mm]	Tau_s[ps]	Eta[%]	std(Eta)	L_opt[mm]	Tau_s[ps]	Eta[%]	std(Eta)
	13.23	2.89	30%	0.28	10.50	2.84	34%	0.31	12.10	2.84	31%	0.29
	17.54	2.83	26%	0.25	14.82	2.81	28%	0.27	16.42	2.84	27%	0.26
L_air_before 3[m]	21.86	3.06	25%	0.24	19.14	2.93	26%	0.25	20.74	3.07	26%	0.25
	26.19	3.38	24%	0.24	23.46	3.22	25%	0.24	25.06	3.22	23%	0.24
	30.51	3.88	23%	0.25	27.78	3.45	23%	0.24	29.38	3.69	23%	0.25
	34.83	4.62	23%	0.25	32.11	4.14	23%	0.25	33.70	4.41	23%	0.25
	39.15	5.20	21%	0.24	36.42	4.89	22%	0.25	38.02	5.08	22%	0.25
-2	L_opt[mm]	Tau_s[ps]	Eta[%]	std(Eta)	L_opt[mm]	Tau_s[ps]	Eta[%]	std(Eta)	L_opt[mm]	Tau_s[ps]	Eta[%]	std(Eta)
	13.22	1.98	30%	0.27	10.50	2.04	36%	0.31	12.09	1.93	32%	0.28
L_air_before 3[m]	17.54	2.11	26%	0.24	14.81	1.93	28%	0.25	16.41	1.99	27%	0.24
	21.85	2.33	24%	0.23	19.13	2.10	25%	0.23	20.73	2.23	25%	0.23
	26.18	3.06	23%	0.23	23.45	2.60	24%	0.23	25.06	2.88	24%	0.24
	30.50	3.83	22%	0.24	27.78	3.32	23%	0.24	29.38	3.64	23%	0.24
	34.82	4.45	21%	0.23	32.10	4.06	22%	0.23	33.70	4.29	21%	0.23
	39.14	5.02	20%	0.23	36.42	4.71	21%	0.23	38.02	4.82	20%	0.23
-1	L_opt[mm]	Tau_s[ps]	Eta[%]	std(Eta)	L_opt[mm]	Tau_s[ps]	Eta[%]	std(Eta)	L_opt[mm]	Tau_s[ps]	Eta[%]	std(Eta)
	13.21	1.13	28%	0.25	10.49	1.17	35%	0.30	12.09	1.19	31%	0.27
	17.52	1.56	24%	0.22	14.80	1.20	26%	0.23	16.40	1.39	25%	0.22
L_air_before 3[m]	21.85	2.28	24%	0.23	19.12	1.79	24%	0.22	20.72	2.08	24%	0.22
	26.18	3.07	23%	0.22	23.44	2.56	23%	0.22	25.05	2.84	23%	0.22
	30.50	3.73	21%	0.22	27.77	3.34	22%	0.22	29.37	3.58	21%	0.22
	34.81	4.40	20%	0.22	32.09	3.96	20%	0.21	33.69	4.14	20%	0.22
					36.41	4.55	19%	0.21	38.01	4.67	19%	0.21
TL	L_opt[mm]	Tau_s[ps]	Eta[%]	std(Eta)	L_opt[mm]	Tau_s[ps]	Eta[%]	std(Eta)	L_opt[mm]	Tau_s[ps]	Eta[%]	std(Eta)
	13.20	0.99	28%	0.23	10.48	0.74	34%	0.29	12.07	0.87	29%	0.25
L_air_before 3[m]	17.52	1.57	24%	0.22	14.80	1.18	26%	0.23	16.40	1.40	25%	0.22
	21.84	2.30	23%	0.21	19.12	1.82	24%	0.22	20.72	2.10	23%	0.22
	26.17	3.04	21%	0.21	23.44	2.58	22%	0.21	25.05	2.82	21%	0.21
	30.49	3.68	20%	0.21	27.77	3.25	20%	0.21	29.36	3.52	20%	0.21
					32.09	3.76	19%	0.20				
1	L_opt[mm]	Tau_s[ps]	Eta[%]	std(Eta)	L_opt[mm]	Tau_s[ps]	Eta[%]	std(Eta)	L_opt[mm]	Tau_s[ps]	Eta[%]	std(Eta)
	13.20	1.44	27%	0.24	10.47	1.24	34%	0.29	12.07	1.37	29%	0.25
L_air_before 3[m]	17.52	1.91	23%	0.22	14.79	1.68	25%	0.22	16.39	1.82	24%	0.22
	21.83	2.53	21%	0.21	19.11	2.20	22%	0.21	20.71	2.35	22%	0.21
	26.16	3.08	19%	0.20	23.43	2.67	20%	0.21	25.04	2.87	20%	0.20
					27.76	3.26	19%	0.20				
2	L_opt[mm]	Tau_s[ps]	Eta[%]	std(Eta)	L_opt[mm]	Tau_s[ps]	Eta[%]	std(Eta)	L_opt[mm]	Tau_s[ps]	Eta[%]	std(Eta)
	13.19	2.35	26%	0.23	10.47	2.04	33%	0.29	12.07	2.15	28%	0.25
L_air_before 3[m]	17.51	2.89	22%	0.21	14.79	2.50	24%	0.23	16.38	2.79	22%	0.22
	21.83	3.41	20%	0.21	19.11	3.56	21%	0.21	20.70	3.51	20%	0.21
3	L_opt[mm]	Tau_s[ps]	Eta[%]	std(Eta)	L_opt[mm]	Tau_s[ps]	Eta[%]	std(Eta)	L_opt[mm]	Tau_s[ps]	Eta[%]	std(Eta)
	13.18	3.34	24%	0.23	10.46	2.97	30%	0.28	12.06	3.12	26%	0.25
L_air_before 3[m]	17.50	4.74	20%	0.22	14.78	4.93	22%	0.23	16.38	4.80	21%	0.22
L_air_before 3[m]	L_opt[mm]	Tau_s[ps]	Eta[%]	std(Eta)	L_opt[mm]	Tau_s[ps]	Eta[%]	std(Eta)	L_opt[mm]	Tau_s[ps]	Eta[%]	std(Eta)
4					10.46	6.13	28%	0.28	12.05	6.11	24%	0.24

10.4.3 Transform limited examination

We examine the transform limited case thoroughly. As before, the simulated quantities are exhibited for different values of signal chirp, and for a span of air lengths before and after the nonlinear crystal. The results are presented in the following tables, with the highlighted colors defined below:

$\eta_E = \dfrac{E_{SHG}(z_f)}{E_{Pump}(z_i)}[\%]$	Highlighted color
$\eta_E > 45\%$	
$40\% < \eta_E \le 45\%$	
$30\% < \eta_E \le 40\%$	
$20\% < \eta_E \le 30\%$	
$10\% < \eta_E \le 20\%$	
$SLM_{compensation}$ value[Rad]	Highlighted color
$SLM_{compensation} > 350[\text{Rad}]$	
$200[\text{Rad}] \le SLM_{compensation} \le 350[\text{Rad}]$	
$100[\text{Rad}] \le SLM_{compensation} < 200[\text{Rad}]$	
$SLM_{compensation} < 100[\text{Rad}]$	
$\sigma_\eta = std(\eta(\lambda))[\%]$	Highlighted color
$\sigma_\eta > 25\%$	
$22\% < \sigma_\eta \le 25\%$	
$20\% < \sigma_\eta \le 22\%$	
$18\% < \sigma_\eta \le 20\%$	
$16\% < \eta_E \le 18\%$	
$\eta_E \le 16\%$	

Several conclusions can be deduced from the tables below:

- In terms of both conversion efficiency and compensation quality we wish the crystal length to be ~ 10mm
- The longer the signal goes through the air, conversion efficiency fluctuation is smaller $\sigma_\eta = std(\eta(\lambda))$.
- The following useful formula is deduced:

$$L_{crystal}^{n,m} \approx 7.76 + 4.31 \cdot n + 5.68\left(L_{air}^{before}[m] - 3\right)m - 0.795\left(L_{air}^{after}[m] - 6\right)[mm]$$

	Lair	10[m]			Lair	8[m]			Lair	6[m]		
	L_opt[mm]	Eta[%]	std(Eta)	Phi_opt[Rad]	L_opt[mm]	Eta[%]	std(Eta)	Phi_opt[Rad]	L_opt[mm]	Eta[%]	std(Eta)	Phi_opt[Rad]
3[m]	8.89	33%	0.29	99.21	6.16	28%	0.25	149.87	7.76	30%	0.27	116.65
	13.20	28%	0.24	90.91	10.48	35%	0.30	76.68	12.07	29%	0.25	78.56
	17.53	25%	0.22	159.59	14.80	26%	0.23	111.14	16.40	25%	0.22	138.40
	21.84	23%	0.21	256.19	19.12	24%	0.22	196.29	20.72	23%	0.21	233.76
	26.17	21%	0.21	341.27	23.44	22%	0.21	285.76	25.04	21%	0.21	315.49
	30.48	19%	0.21	440.21	27.77	20%	0.21	380.31	29.36	20%	0.21	417.21
3.25[m]	5.99	25%	0.23	145.89	7.58	28%	0.25	122.28	9.18	32%	0.28	95.19
	10.30	32%	0.28	85.30	11.90	27%	0.23	70.41	13.49	24%	0.21	95.95
	14.62	23%	0.20	116.41	16.22	22%	0.20	144.03	17.82	22%	0.20	172.28
	18.94	21%	0.20	194.11	20.54	21%	0.20	223.08	22.14	20%	0.20	253.97
	23.27	20%	0.19	282.80	24.87	19%	0.19	321.56	26.46	18%	0.19	352.63
	27.58	18%	0.19	375.53	29.18	18%	0.19	405.52	30.78	17%	0.19	441.07
3.5[m]	7.40	25%	0.23	123.11	9.00	29%	0.26	97.86	6.28	23%	0.21	148.33
	11.72	25%	0.22	79.34	13.32	22%	0.19	90.66	10.60	30%	0.26	75.72
	16.04	20%	0.18	134.49	17.64	19%	0.18	162.35	14.92	21%	0.18	113.73
	20.37	19%	0.18	225.66	21.96	18%	0.18	259.14	19.24	19%	0.18	197.37
	24.68	17%	0.18	311.46	26.28	17%	0.18	342.56	23.56	17%	0.18	288.77
	29.01	16%	0.18	410.87	30.60	16%	0.18	443.33	27.88	16%	0.18	381.60
	33.33	15%	0.17	496.58					32.20	15%	0.18	473.49
3.75[m]	8.82	25%	0.23	101.30	6.10	20%	0.19	144.05	7.70	22%	0.21	119.03
	13.14	19%	0.17	92.16	10.41	27%	0.24	83.87	12.01	22%	0.19	72.75
	17.46	17%	0.16	168.31	14.74	18%	0.16	119.08	16.34	18%	0.16	145.92
	21.79	16%	0.17	248.32	19.06	16%	0.16	196.99	20.66	16%	0.16	226.02
	26.10	14%	0.16	348.63	23.38	15%	0.16	283.99	24.98	15%	0.16	322.80
	30.43	14%	0.16	432.51	27.70	14%	0.16	378.62	29.30	14%	0.16	408.62
					32.02	14%	0.16	471.81				
4[m]	5.92	18%	0.17	155.17	7.52	19%	0.19	121.59	9.12	24%	0.23	96.54
	10.24	25%	0.22	80.46	11.84	20%	0.18	78.67	13.44	17%	0.15	90.44
	14.56	16%	0.14	109.93	16.16	15%	0.14	137.22	17.76	15%	0.14	165.14
	18.89	14%	0.15	188.82	20.48	14%	0.15	226.77	22.08	13%	0.15	262.15
	23.20	13%	0.15	284.77	24.80	13%	0.15	314.52	26.40	13%	0.15	344.35
	27.53	13%	0.15	373.01	29.12	12%	0.15	412.19	30.72	12%	0.15	446.46
	31.84	12%	0.15	469.54	33.44	12%	0.15	499.75				
4.25[m]	7.35	17%	0.17	120.72	8.94	20%	0.20	99.84	6.22	16%	0.15	142.53
	11.66	18%	0.16	69.28	13.26	14%	0.13	94.77	10.53	22%	0.20	82.44
	15.99	13%	0.13	138.75	17.58	12%	0.12	171.16	14.86	14%	0.13	119.70
	20.30	12%	0.14	222.02	21.90	12%	0.14	251.30	19.18	12%	0.13	199.88
	24.63	12%	0.14	314.21	26.22	11%	0.14	351.74	23.50	12%	0.14	285.21
	28.94	11%	0.14	404.65	30.54	11%	0.14	434.74	27.82	11%	0.14	381.72
									32.14	10%	0.14	473.15

While $\sigma_\eta = std(\eta(\lambda))$ gives some intuition about the conversion efficiency, it is more informative to visually observe the conversion efficiency curves. For demonstration, we plot the conversion efficiency curves for different crystals lengths and for different air propagation lengths: 3m and 4.25m.
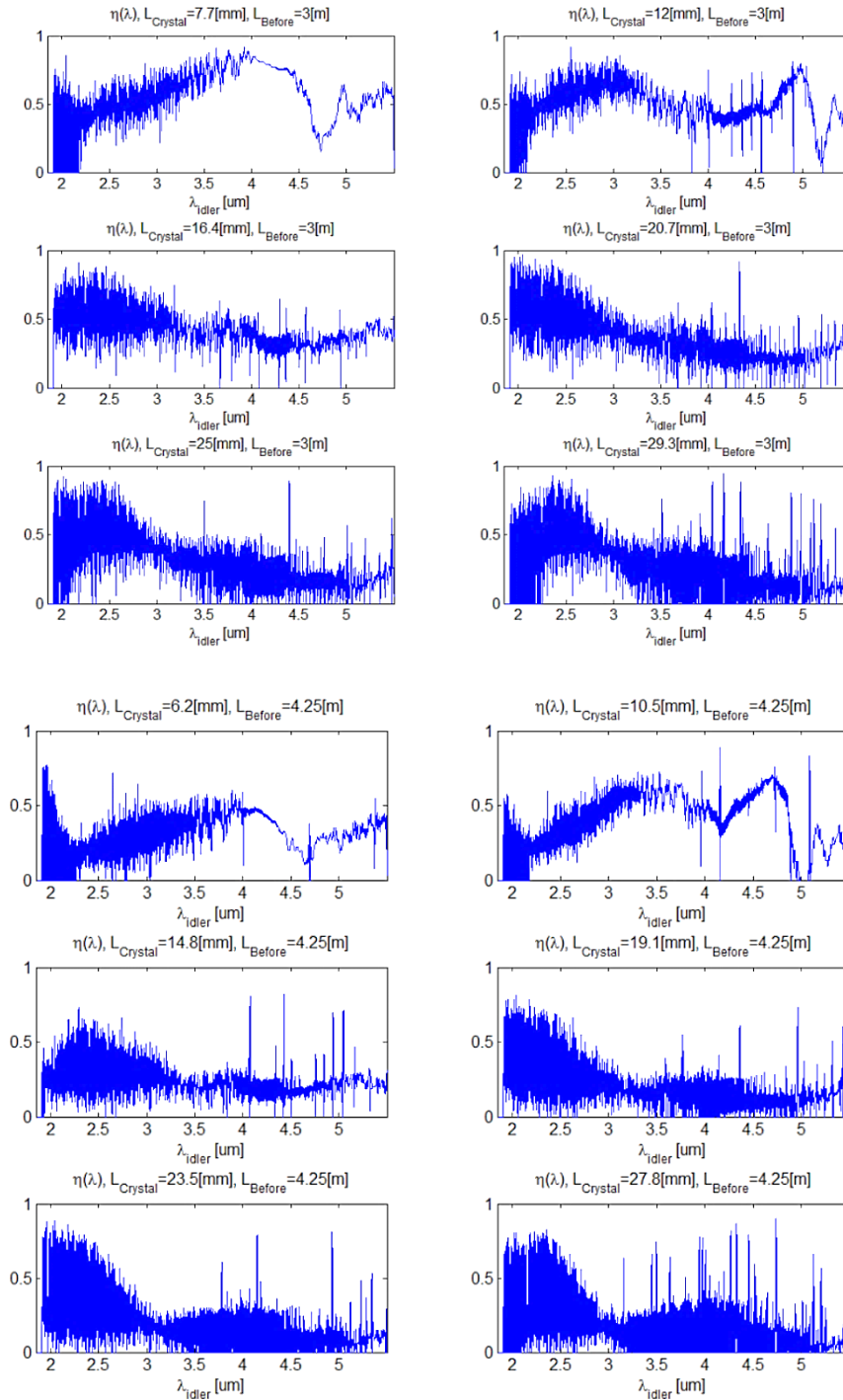
Figure 34. Conversion efficiency dependence with crystal length for different air propagation lengths.

We can visually deduce from the above what schemes are good in terms of conversion efficiency. We label good schemes with green (left columns):

	Lair L_opt[mm]	10[m] Eta[%]	Lair L_opt[mm]	8[m] Eta[%]	6[m] L_opt[mm]	Eta[%]
3[m]	8.89	33%	6.16	28%	7.76	30%
	13.20	28%	10.48	35%	12.07	29%
	17.53	25%	14.80	26%	16.40	25%
	21.84	23%	19.12	24%	20.72	23%
	26.17	21%	23.44	22%	25.04	21%
	30.48	19%	27.77	20%	29.36	20%
3.25[m]	5.99	25%	7.58	28%	9.18	32%
	10.30	32%	11.90	27%	13.49	24%
	14.62	23%	16.22	22%	17.82	22%
	18.94	21%	20.54	21%	22.14	20%
	23.27	20%	24.87	19%	26.46	18%
	27.58	18%	29.18	18%	30.78	17%
3.5[m]	7.40	25%	9.00	29%	6.28	23%
	11.72	25%	13.32	22%	10.60	30%
	16.04	20%	17.64	19%	14.92	21%
	20.37	19%	21.96	18%	19.24	19%
	24.68	17%	26.28	17%	23.56	17%
	29.01	16%	30.60	16%	27.88	16%
	33.33	15%			32.20	15%

	Lair L_opt[mm]	10[m] Eta[%]	Lair L_opt[mm]	8[m] Eta[%]	6[m] L_opt[mm]	Eta[%]
3.75[m]	8.82	25%	6.10	20%	7.70	22%
	13.14	19%	10.41	27%	12.01	22%
	17.46	17%	14.74	18%	16.34	18%
	21.79	16%	19.06	16%	20.66	16%
	26.10	14%	23.38	15%	24.98	15%
	30.43	14%	27.70	14%	29.30	14%
			32.02	14%		
4[m]	5.92	18%	7.52	19%	9.12	24%
	10.24	25%	11.84	20%	13.44	17%
	14.56	16%	16.16	15%	17.76	15%
	18.89	14%	20.48	14%	22.08	13%
	23.20	13%	24.80	13%	26.40	13%
	27.53	13%	29.12	12%	30.72	12%
	31.84	12%	33.44	12%		
4.25[m]	7.35	17%	8.94	20%	6.22	16%
	11.66	18%	13.26	14%	10.53	22%
	15.99	13%	17.58	12%	14.86	14%
	20.30	12%	21.90	12%	19.18	12%
	24.63	12%	26.22	11%	23.50	12%
	28.94	11%	30.54	11%	27.82	11%
					32.14	10%

10.5 Appendix E- Pulsed four wave mixing interactions derivation

We describe the time dependent evolution of Four Wave Mixing in dielectrical waveguides via third order susceptibility. Let's assume we are operating in a single mode waveguide.

$$(E.1)\ \vec{E}_t = \int_{-\infty}^{+\infty} \frac{d\omega}{2\pi} \frac{1}{2} \underbrace{\left(A(z,\omega) + A^*(z,-\omega) \right) \vec{E}_t(x,y,\omega) e^{-i\beta(z,\omega)z}}_{\bar{E}(z,\omega)} e^{i\omega t}$$

Let's write Maxwell Equations in the time domain:

$$(E.2)\ \nabla \times \vec{E} = -\frac{\partial \vec{B}}{\partial t} \qquad \Rightarrow \nabla \times \bar{E}(z,\omega) = -i\omega \bar{B} = -i\omega\mu\bar{H}$$

$$(E.3)\ \nabla \times \vec{H} = \varepsilon \frac{\partial \vec{E}}{\partial t} + \frac{\partial \vec{P}_{NL}}{\partial t} \Rightarrow \nabla \times \bar{H}(z,\omega) = i\omega\varepsilon\bar{E}(z,\omega) + i\omega\bar{P}_{NL}(z,\omega)$$

Let's write Eq. (E.2) and Eq. (E.3) for two fields labeled 1 and 2:

$$(E.4)\ \nabla \times \bar{E}_1(z,\omega) = -i\omega\mu\bar{H}_1$$
$$(E.5)\ \nabla \times \bar{H}_1(z,\omega) = i\omega\varepsilon\bar{E}_1(z,\omega) + i\omega\bar{P}_{NL,1}(z,\omega)$$
$$(E.6)\ \nabla \times \bar{E}_2(z,\omega) = -i\omega\mu\bar{H}_2$$
$$(E.7)\ \nabla \times \bar{H}_2(z,\omega) = i\omega\varepsilon\bar{E}_2(z,\omega) + i\omega\bar{P}_{NL,2}(z,\omega)$$

Using the following identity:

$$(E.8)\ \vec{\nabla} \cdot \left(\vec{a} \times \vec{b} \right) = \vec{b} \cdot \left(\vec{\nabla} \times \vec{a} \right) - \vec{a} \cdot \left(\vec{\nabla} \times \vec{b} \right)$$

It is easy to deduce:

$$(E.9)\ \vec{\nabla} \cdot \left(\bar{E}_1 \times \bar{H}_2^* + \bar{E}_2^* \times \bar{H}_1 \right) = i\omega \left(\bar{E}_1 \cdot \bar{P}^*_{NL,2} - \bar{E}_2^* \cdot \bar{P}_{NL,1} \right)$$

We can therefore write:

$$(E.10)\ \int \vec{\nabla} \cdot \left(\bar{E}_1 \times \bar{H}_2^* + \bar{E}_2^* \times \bar{H}_1 \right) dxdy = \int \partial_z \left(\bar{E}_{1t} \times \bar{H}_{2t}^* + \bar{E}_{2t}^* \times \bar{H}_{1t} \right)_z dxdy + \int \vec{\nabla}_t \left(\bar{E}_1 \times \bar{H}_2^* + \bar{E}_2^* \times \bar{H}_1 \right)_t dxdy =$$
$$= \int \partial_z \left(\bar{E}_{1t} \times \bar{H}_{2t}^* + \bar{E}_{2t}^* \times \bar{H}_{1t} \right)_z dxdy + \underbrace{\oint ds \left(\bar{E}_1 \times \bar{H}_2^* + \bar{E}_2^* \times \bar{H}_1 \right)_t \cdot \vec{n}}_{0} = \int \partial_z \left(\bar{E}_{1t} \times \bar{H}_{2t}^* + \bar{E}_{2t}^* \times \bar{H}_{1t} \right) dxdy$$

Let's assume that $\vec{E}_2$ is a waveguide mode. Hence, it solves Eq. (E.6) and Eq. (E.7) with $P_{NL,2}(z,\omega) = 0$. We'll therefore get (Eq. (E.9) together with Eq. (E.10)):

$$(E.11) \int \partial_z \left(\bar{E}_{1t} \times \bar{H}_{2t}^* + \bar{E}_{2t}^* \times \bar{H}_{1t} \right)_z dxdy = -i\omega \int \bar{E}_2^* \cdot \bar{P}_{NL,1} dxdy$$

Now, let's expand the electric field in terms of its eigenmodes, recalling that field 2 is an eigenmode:

$$(E.12)\ \bar{E}_{1t} = \sum_v A_v(z,\omega) e^{-i\beta_v(z,\omega)z} \bar{E}_{tv}(x,y)$$

$$\bar{H}_{1t} = \sum_v A_v(z,\omega) e^{-i\beta_v(z,\omega)z} \bar{H}_{tv}(x,y)$$

$$(E.13)\ \bar{E}_{2t} = A_\mu(z,\omega) e^{-i\beta_\mu(z,\omega)z} \bar{E}_{t\mu}(x,y)$$

$$\bar{H}_{2t} = A_\mu(z,\omega) e^{-i\beta_\mu(z,\omega)z} \bar{H}_{t\mu}(x,y)$$

Substitution Eq. (E.12),(E.13) into Eq. (E.11) and using the orthogonally relation, yields:

$$(E.14) \iint \bar{E}_{t\mu}^*(x,y) \times H_{tv}(x,y) dxdy = \frac{1}{2}\delta_{\mu v}$$

$$(E.15)\ \frac{dA_\mu(z,\omega)}{dz} = -i\omega \iint \bar{P}_{NL,1}(z,\omega) \cdot \left(\bar{E}_{t\mu}^* e^{i\beta(z,\omega)z} \right) dxdy$$

It's time to describe the nonlinear third order susceptibility phasor of a centrosymmetric homogenous material. It can be shown that the third order susceptibility phasor elements that contribute to the polarization in the x direction are:

$$(E.16)\ P_x : \chi_{xxxx} = \chi_3, \chi_{xxyy} = \chi_{xyyx} = \chi_{xyxy} = \frac{\chi_3}{3}$$

And to the polarization in the y direction:

$$(E.17)\ P_y : \chi_{yyyy} = \chi_3, \chi_{yyxx} = \chi_{yxxy} = \chi_{yxyx} = \frac{\chi_3}{3}$$

We can therefore write:

$$(E.18)\ P_x(t) = \varepsilon_0 \chi_3 E_x^{\ 3}(t) + \varepsilon_0 \frac{\chi_3}{3} \cdot 3E_x(t)E_y^{\ 2}(t) = \varepsilon_0 \chi_3 E_x(t)\left(E_x^{\ 2}(t) + E_y^{\ 2}(t) \right)$$

$$(E.19)\ P_y(t) = \varepsilon_0 \chi_3 E_y^{\ 3}(t) + \varepsilon_0 \frac{\chi_3}{3} \cdot 3E_y(t)E_x^{\ 2}(t) = \varepsilon_0 \chi_3 E_y(t)\left(E_x^{\ 2}(t) + E_y^{\ 2}(t) \right)$$

$$(E.20) \ \vec{P}(t) = \varepsilon_0 \chi_3 \left(\sum_{j \in x, y} E_j(t) E_j(t) \right) \vec{E}(t)$$

$$(E.21) \ P_k(t) = \varepsilon_0 \chi_3 \left(\sum_{j \in x, y} E_j(t) E_j(t) \right) E_k(t)$$

$$(E.22) \ P_k(\vec{r}, \omega) = \varepsilon_0 \chi_3 \sum_{j \in x, y} E_j(\vec{r}, \omega) * E_j(\vec{r}, \omega) * E_k(\vec{r}, \omega)$$

where k stands for the transverse indexes, x or y.

We wish to incorporate Eq. (E.22) into Eq. (E.15):

$$(E.23) \ \frac{dA_\mu(z, \omega)}{dz} = -i\omega \iint \overline{P}(\vec{r}, \omega) \cdot \left(\overline{E}_{t\mu}^* e^{i\beta(z,\omega)z} \right) dxdy = -i\omega e^{i\beta(z,\omega)z} \iint \sum_k P_k(\vec{r}, \omega) E_{t,k}^* dxdy$$

$$\frac{dA_\mu(z, \omega)}{dz} = -i\omega \varepsilon_0 \chi_3 e^{i\beta(z,\omega)z} \iint \sum_{k \in x, y} \sum_{j \in x, y} E_j(\vec{r}, \omega) * E_j(\vec{r}, \omega) * E_k(\vec{r}, \omega) E_k^*(\vec{r}, \omega) dxdy$$

We substitute the electric field phasor as defined in Eq. (E.1):

$$\overline{E}(z, \omega) = \frac{1}{2} \left(A(z, \omega) + A^*(z, -\omega) \right) \vec{E}_t(x, y, \omega) e^{-i\beta(z,\omega)z}$$

We assume that 4 pulses are inserted into our grating. We write the fields amplitude as superposition of pulses:

$$(E.24) \ A(z, \omega) = A_1(z, \omega) + A_2(z, \omega) + A_3(z, \omega) + A_4(z, \omega) = \sum_{\alpha=1,2,3,4} A_\alpha(z, \omega)$$

We assume that amplitude $A_\beta(z, \omega)$ is centered around ω_β, when the central frequencies obey $\omega_1 + \omega_2 = \omega_3 + \omega_4$. According to the definition (8.12), one deduces $\frac{dA_\delta(z, \omega)}{dz} = \frac{1}{2} \frac{dA_\delta(z, \omega)}{dz}$, where $\delta \in [1, 2, 3, 4]$.

The spectral field envelope centered around ω_δ dependence with the optical axis is determined by:

$$(E.25) \ \frac{1}{2} \frac{dA_\delta(z, \omega)}{dz} = -i\omega \varepsilon_0 \chi_3 e^{i\beta(z,\omega)z} \iint \sum_{k, j \in x, y} E_j(\vec{r}, \omega) * E_j(\vec{r}, \omega) * E_k(\vec{r}, \omega) E_k^*(\vec{r}, \omega) dxdy =$$

$$= -i\omega \varepsilon_0 \chi_3 \frac{1}{2^3} \iint dxdy \left(\sum_{k, j \in x, y} \sum_{\alpha, \beta, \gamma=1}^{4} \begin{pmatrix} E_j(\vec{r}, \omega) e^{-i\beta(z,\omega)z} \left(A_\alpha(z, \omega) + A_\alpha^*(z, -\omega) \right) * \\ E_j(\vec{r}, \omega) e^{-i\beta(z,\omega)z} \left(A_\beta(z, \omega) + A_\beta^*(z, -\omega) \right) * \\ E_k(\vec{r}, \omega) e^{-i\beta(z,\omega)z} \left(A_\gamma(z, \omega) + A_\gamma^*(z, -\omega) \right) \end{pmatrix} \cdot E_k(\vec{r}, \omega) e^{i\beta(z,\omega)z} \right)$$

In order to simplify the convolution integral, we assume that the electric field profile merely changes within the spectral envelope of the pulses. In order words:

$$(E.26) \quad E_j(\vec{r},\omega)e^{-i\beta(z,\omega)z}\left(A_\alpha(z,\omega)+A_\alpha{}^*(z,-\omega)\right) \approx E_j(\vec{r},\omega_\alpha)e^{-i\beta(z,\omega)z}\left(A_\alpha(z,\omega)+A_\alpha{}^*(z,-\omega)\right)$$

We denote $\vec{E}(\vec{r},\omega_\alpha)=\vec{E}_\alpha$. Under the following simplification, Eq. (E.25) considerably simplifies:

$$(E.27) \quad \frac{dA_\delta(z,\omega)}{dz} = -i\frac{\omega\varepsilon_0\chi_3 e^{i\beta(z,\omega)z}}{4}\iint dxdy \left(\begin{array}{l} \displaystyle\sum_{k,j\in x,y} E_j(\vec{r},\omega_\alpha)E_j(\vec{r},\omega_\beta)E_k(\vec{r},\omega_\gamma)E_k{}^*(\vec{r},\omega_\delta)\cdot \\ \displaystyle\sum_{\alpha,\beta,\gamma=1}^{4} \left(\begin{array}{l} e^{-i\beta(z,\omega)z}\left(A_\alpha(z,\omega)+A_\alpha{}^*(z,-\omega)\right)* \\ e^{-i\beta(z,\omega)z}\left(A_\beta(z,\omega)+A_\beta{}^*(z,-\omega)\right)* \\ e^{-i\beta(z,\omega)z}\left(A_\gamma(z,\omega)+A_\gamma{}^*(z,-\omega)\right) \end{array} \right) \end{array} \right)$$

$$(E.28) \quad \frac{dA_\delta(z,\omega)}{dz} = -i\frac{\omega\varepsilon_0\chi_3 e^{i\beta(z,\omega)z}}{4}\sum_{\alpha,\beta,\gamma=1}^{4}\left(\iint dxdy\,\vec{E}_\alpha\cdot\vec{E}_\beta\vec{E}_\gamma\cdot\vec{E}_\delta\right)\left(\begin{array}{l} e^{-i\beta(z,\omega)z}\left(A_\alpha(z,\omega)+A_\alpha{}^*(z,-\omega)\right)* \\ e^{-i\beta(z,\omega)z}\left(A_\beta(z,\omega)+A_\beta{}^*(z,-\omega)\right)* \\ e^{-i\beta(z,\omega)z}\left(A_\gamma(z,\omega)+A_\gamma{}^*(z,-\omega)\right) \end{array} \right)$$

We continue with writing the equations for $A_1(z,\omega)$. The frequency generation terms that contributes to $A_1(z,\omega)$ are the following:

Convolution term	Permutations	Physical meaning
$A_3(z,\omega) * A_4(z,\omega) * A_2^*(z,-\omega)$	$A_3(z,\omega) * A_4(z,\omega) * A_2^*(z,-\omega)$	Interaction term
	$A_3(z,\omega) * A_2^*(z,-\omega) * A_4(z,\omega)$	
	$A_4(z,\omega) * A_3(z,\omega) * A_2^*(z,-\omega)$	
	$A_4(z,\omega) * A_2^*(z,-\omega) * A_3(z,\omega)$	
	$A_2^*(z,-\omega) * A_3(z,\omega) * A_4(z,\omega)$	
	$A_2^*(z,-\omega) * A_4(z,\omega) * A_3(z,\omega)$	
$A_1(z,\omega) * A_1(z,\omega) * A_1^*(z,-\omega)$	$A_1(z,\omega) * A_1(z,\omega) * A_1^*(z,-\omega)$	SPM
	$A_1(z,\omega) * A_1^*(z,-\omega) * A_1(z,\omega)$	
	$A_1^*(z,-\omega) * A_1(z,\omega) * A_1(z,\omega)$	
$A_2(z,\omega) * A_2^*(z,-\omega) * A_1(z,\omega)$	$A_2(z,\omega) * A_2^*(z,-\omega) * A_1(z,\omega)$	XPM
	$A_2(z,\omega) * A_1(z,\omega) * A_2^*(z,-\omega)$	
	$A_2^*(z,-\omega) * A_2(z,\omega) * A_1(z,\omega)$	
	$A_2^*(z,-\omega) * A_1(z,\omega) * A_2(z,\omega)$	
	$A_1(z,\omega) * A_2^*(z,-\omega) * A_2(z,\omega)$	
	$A_1(z,\omega) * A_2(z,\omega) * A_2^*(z,-\omega)$	
$A_3(z,\omega) * A_3^*(z,-\omega) * A_1(z,\omega)$	$A_3(z,\omega) * A_3^*(z,-\omega) * A_1(z,\omega)$	XPM
	$A_3(z,\omega) * A_1(z,\omega) * A_3^*(z,-\omega)$	
	$A_3^*(z,-\omega) * A_3(z,\omega) * A_1(z,\omega)$	
	$A_3^*(z,-\omega) * A_1(z,\omega) * A_3(z,\omega)$	
	$A_1(z,\omega) * A_3^*(z,-\omega) * A_3(z,\omega)$	
	$A_1(z,\omega) * A_3(z,\omega) * A_3^*(z,-\omega)$	
$A_4(z,\omega) * A_4^*(z,-\omega) * A_1(z,\omega)$	$A_4(z,\omega) * A_4^*(z,-\omega) * A_1(z,\omega)$	XPM
	$A_4(z,\omega) * A_1(z,\omega) * A_4^*(z,-\omega)$	
	$A_4^*(z,-\omega) * A_4(z,\omega) * A_1(z,\omega)$	
	$A_4^*(z,-\omega) * A_1(z,\omega) * A_4(z,\omega)$	
	$A_1(z,\omega) * A_4^*(z,-\omega) * A_4(z,\omega)$	
	$A_1(z,\omega) * A_4(z,\omega) * A_4^*(z,-\omega)$	

The equations describing $A_1(z,\omega)$ are introduced:

(E.29)

$$\frac{dA_1(z,\omega)}{dz} = -i\frac{\omega\varepsilon_0\chi_3}{4}e^{i\beta(z,\omega)z}\left[\begin{array}{l} A_3(z,\omega)e^{-i\beta(z,\omega)z}*A_4(z,\omega)e^{-i\beta(z,\omega)z}*A_2^{*}(z,-\omega)e^{-i\beta(z,\omega)z}\iint dxdy\begin{pmatrix}2\vec{E}_3\cdot\vec{E}_4\vec{E}_2\cdot\vec{E}_1\\ +2\vec{E}_3\cdot\vec{E}_2\vec{E}_4\cdot\vec{E}_1\\ +2\vec{E}_4\cdot\vec{E}_2\vec{E}_3\cdot\vec{E}_1\end{pmatrix}\\[2em] A_1(z,\omega)e^{-i\beta(z,\omega)z}*A_1^{*}(z,-\omega)e^{-i\beta(z,\omega)z}*A_1(z,\omega)e^{-i\beta(z,\omega)z}\iint dxdy\left(3\left|\vec{E}_1\right|^4\right)\\[2em] A_2(z,\omega)e^{-i\beta(z,\omega)z}*A_2^{*}(z,-\omega)e^{-i\beta(z,\omega)z}*A_1(z,\omega)e^{-i\beta(z,\omega)z}\iint dxdy\begin{pmatrix}2\left|\vec{E}_2\right|^2\left|\vec{E}_1\right|^2\\ +4\left|\vec{E}_2\cdot\vec{E}_1\right|^2\end{pmatrix}\\[2em] A_3(z,\omega)e^{-i\beta(z,\omega)z}*A_3^{*}(z,-\omega)e^{-i\beta(z,\omega)z}*A_1(z,\omega)e^{-i\beta(z,\omega)z}\iint dxdy\begin{pmatrix}2\left|\vec{E}_3\right|^2\left|\vec{E}_1\right|^2\\ +4\left|\vec{E}_3\cdot\vec{E}_1\right|^2\end{pmatrix}\\[2em] A_4(z,\omega)e^{-i\beta(z,\omega)z}*A_4^{*}(z,-\omega)e^{-i\beta(z,\omega)z}*A_1(z,\omega)e^{-i\beta(z,\omega)z}\iint dxdy\begin{pmatrix}2\left|\vec{E}_4\right|^2\left|\vec{E}_1\right|^2\\ +4\left|\vec{E}_4\cdot\vec{E}_1\right|^2\end{pmatrix}\end{array}\right]$$

The equations describing $A_2(z,\omega)$ are deduced by replacing 1→2, 2→1.

(E.30)

$$\frac{dA_2(z,\omega)}{dz} = -i\frac{\omega\varepsilon_0\chi_3}{4}e^{i\beta(z,\omega)z}\left[\begin{array}{l} A_3(z,\omega)e^{-i\beta(z,\omega)z}*A_4(z,\omega)e^{-i\beta(z,\omega)z}*A_1^{*}(z,-\omega)e^{-i\beta(z,\omega)z}\iint dxdy\begin{pmatrix}2\vec{E}_3\cdot\vec{E}_4\vec{E}_2\cdot\vec{E}_1\\ +2\vec{E}_3\cdot\vec{E}_1\vec{E}_4\cdot\vec{E}_2\\ +2\vec{E}_4\cdot\vec{E}_1\vec{E}_3\cdot\vec{E}_2\end{pmatrix}\\[2em] A_2(z,\omega)e^{-i\beta(z,\omega)z}*A_2^{*}(z,-\omega)e^{-i\beta(z,\omega)z}*A_2(z,\omega)e^{-i\beta(z,\omega)z}\iint dxdy\left(3\left|\vec{E}_2\right|^4\right)\\[2em] A_1(z,\omega)e^{-i\beta(z,\omega)z}*A_1^{*}(z,-\omega)e^{-i\beta(z,\omega)z}*A_2(z,\omega)e^{-i\beta(z,\omega)z}\iint dxdy\begin{pmatrix}2\left|\vec{E}_2\right|^2\left|\vec{E}_1\right|^2\\ +4\left|\vec{E}_2\cdot\vec{E}_1\right|^2\end{pmatrix}\\[2em] A_3(z,\omega)e^{-i\beta(z,\omega)z}*A_3^{*}(z,-\omega)e^{-i\beta(z,\omega)z}*A_2(z,\omega)e^{-i\beta(z,\omega)z}\iint dxdy\begin{pmatrix}2\left|\vec{E}_3\right|^2\left|\vec{E}_2\right|^2\\ +4\left|\vec{E}_3\cdot\vec{E}_2\right|^2\end{pmatrix}\\[2em] A_4(z,\omega)e^{-i\beta(z,\omega)z}*A_4^{*}(z,-\omega)e^{-i\beta(z,\omega)z}*A_2(z,\omega)e^{-i\beta(z,\omega)z}\iint dxdy\begin{pmatrix}2\left|\vec{E}_4\right|^2\left|\vec{E}_2\right|^2\\ +4\left|\vec{E}_4\cdot\vec{E}_2\right|^2\end{pmatrix}\end{array}\right]$$

The equations describing $A_3(z,\omega)$ are deduced from the equations describing the spectral amplitude of $A_1(z,\omega)$ by replacing 1→3, 2→4, 3→1, 4→2:

(E.31)

$$
\frac{dA_3(z,\omega)}{dz} = -i\frac{\omega\varepsilon_0\chi_3\, e^{i\beta(z,\omega)z}}{4}
\begin{bmatrix}
A_1(z,\omega)e^{-i\beta(z,\omega)z} * A_2(z,\omega)e^{-i\beta(z,\omega)z} * A_4^{*}(z,-\omega)e^{-i\beta(z,\omega)z}\iint dxdy \begin{pmatrix} 2\vec{E}_1\cdot\vec{E}_2\vec{E}_4\cdot\vec{E}_3 \\ +2\vec{E}_1\cdot\vec{E}_4\vec{E}_2\cdot\vec{E}_3 \\ +2\vec{E}_2\cdot\vec{E}_4\vec{E}_1\cdot\vec{E}_3 \end{pmatrix} \\[2em]
A_3(z,\omega)e^{-i\beta(z,\omega)z} * A_3^{*}(z,-\omega)e^{-i\beta(z,\omega)z} * A_3(z,\omega)e^{-i\beta(z,\omega)z}\iint dxdy \left(3\left|\vec{E}_3\right|^4\right) \\[2em]
A_4(z,\omega)e^{-i\beta(z,\omega)z} * A_4^{*}(z,-\omega)e^{-i\beta(z,\omega)z} * A_3(z,\omega)e^{-i\beta(z,\omega)z}\iint dxdy \begin{pmatrix} 2\left|\vec{E}_4\right|^2\left|\vec{E}_3\right|^2 \\ +4\left|\vec{E}_4\cdot\vec{E}_3\right|^2 \end{pmatrix} \\[2em]
A_1(z,\omega)e^{-i\beta(z,\omega)z} * A_1^{*}(z,-\omega)e^{-i\beta(z,\omega)z} * A_3(z,\omega)e^{-i\beta(z,\omega)z}\iint dxdy \begin{pmatrix} 2\left|\vec{E}_1\right|^2\left|\vec{E}_3\right|^2 \\ +4\left|\vec{E}_1\cdot\vec{E}_3\right|^2 \end{pmatrix} \\[2em]
A_2(z,\omega)e^{-i\beta(z,\omega)z} * A_2^{*}(z,-\omega)e^{-i\beta(z,\omega)z} * A_3(z,\omega)e^{-i\beta(z,\omega)z}\iint dxdy \begin{pmatrix} 2\left|\vec{E}_2\right|^2\left|\vec{E}_3\right|^2 \\ +4\left|\vec{E}_2\cdot\vec{E}_3\right|^2 \end{pmatrix}
\end{bmatrix}
$$

The equations describing $A_4(z,\omega)$ are deduced from the equations describing the spectral amplitude of $A_3(z,\omega)$ by replacing 3→4, 4→3.

(E.32)

$$
\frac{dA_4(z,\omega)}{dz} = -i\frac{\omega\varepsilon_0\chi_3\, e^{i\beta(z,\omega)z}}{4}
\begin{bmatrix}
A_1(z,\omega)e^{-i\beta(z,\omega)z} * A_2(z,\omega)e^{-i\beta(z,\omega)z} * A_3^{*}(z,-\omega)e^{-i\beta(z,\omega)z}\iint dxdy \begin{pmatrix} 2\vec{E}_1\cdot\vec{E}_2\vec{E}_3\cdot\vec{E}_4 \\ +2\vec{E}_1\cdot\vec{E}_3\vec{E}_2\cdot\vec{E}_4 \\ +2\vec{E}_2\cdot\vec{E}_3\vec{E}_1\cdot\vec{E}_4 \end{pmatrix} \\[2em]
A_4(z,\omega)e^{-i\beta(z,\omega)z} * A_4^{*}(z,-\omega)e^{-i\beta(z,\omega)z} * A_4(z,\omega)e^{-i\beta(z,\omega)z}\iint dxdy \left(3\left|\vec{E}_4\right|^4\right) \\[2em]
A_3(z,\omega)e^{-i\beta(z,\omega)z} * A_3^{*}(z,-\omega)e^{-i\beta(z,\omega)z} * A_4(z,\omega)e^{-i\beta(z,\omega)z}\iint dxdy \begin{pmatrix} 2\left|\vec{E}_4\right|^2\left|\vec{E}_3\right|^2 \\ +4\left|\vec{E}_4\cdot\vec{E}_3\right|^2 \end{pmatrix} \\[2em]
A_1(z,\omega)e^{-i\beta(z,\omega)z} * A_1^{*}(z,-\omega)e^{-i\beta(z,\omega)z} * A_4(z,\omega)e^{-i\beta(z,\omega)z}\iint dxdy \begin{pmatrix} 2\left|\vec{E}_1\right|^2\left|\vec{E}_4\right|^2 \\ +4\left|\vec{E}_1\cdot\vec{E}_4\right|^2 \end{pmatrix} \\[2em]
A_2(z,\omega)e^{-i\beta(z,\omega)z} * A_2^{*}(z,-\omega)e^{-i\beta(z,\omega)z} * A_4(z,\omega)e^{-i\beta(z,\omega)z}\iint dxdy \begin{pmatrix} 2\left|\vec{E}_2\right|^2\left|\vec{E}_4\right|^2 \\ +4\left|\vec{E}_2\cdot\vec{E}_4\right|^2 \end{pmatrix}
\end{bmatrix}
$$

We define the following integrals:

$$(E.33)\ \gamma_{Int} = \frac{1}{2}\iint dxdy\left(\vec{E}_3\cdot\vec{E}_4\vec{E}_2\cdot\vec{E}_1 + \vec{E}_3\cdot\vec{E}_2\vec{E}_4\cdot\vec{E}_1 + \vec{E}_4\cdot\vec{E}_2\vec{E}_3\cdot\vec{E}_1\right)$$

$$(E.34)\ \mu_{i,j} = \mu_{j,i} = \frac{1}{2}\iint dxdy\left(\left|\vec{E}_i\right|^2\left|\vec{E}_j\right|^2 + 2\left|\vec{E}_i\cdot\vec{E}_j\right|^2\right)$$

The equations deduced are the following:

(E.35)

$$\frac{dA_1(z,\omega)}{dz} = -i\omega\varepsilon_0\chi_3\,e^{i\beta(z,\omega)z}\begin{bmatrix}\gamma_{Int}A_3(z,\omega)e^{-i\beta(z,\omega)z}*A_4(z,\omega)e^{-i\beta(z,\omega)z}*A_2^{\,*}(z,-\omega)e^{-i\beta(z,\omega)z}\ +\\[4pt]\dfrac{\mu_{1,1}}{2}A_1(z,\omega)e^{-i\beta(z,\omega)z}*A_1^{\,*}(z,-\omega)e^{-i\beta(z,\omega)z}*A_1(z,\omega)e^{-i\beta(z,\omega)z}\ +\\[4pt]\mu_{1,2}A_2(z,\omega)e^{-i\beta(z,\omega)z}*A_2^{\,*}(z,-\omega)e^{-i\beta(z,\omega)z}*A_1(z,\omega)e^{-i\beta(z,\omega)z}\ +\\[4pt]\mu_{1,3}A_3(z,\omega)e^{-i\beta(z,\omega)z}*A_3^{\,*}(z,-\omega)e^{-i\beta(z,\omega)z}*A_1(z,\omega)e^{-i\beta(z,\omega)z}\ +\\[4pt]\mu_{1,4}A_4(z,\omega)e^{-i\beta(z,\omega)z}*A_4^{\,*}(z,-\omega)e^{-i\beta(z,\omega)z}*A_1(z,\omega)e^{-i\beta(z,\omega)z}\end{bmatrix}$$

(E.36)

$$\frac{dA_2(z,\omega)}{dz} = -i\omega\varepsilon_0\chi_3\,e^{i\beta(z,\omega)z}\begin{bmatrix}\gamma_{Int}A_3(z,\omega)e^{-i\beta(z,\omega)z}*A_4(z,\omega)e^{-i\beta(z,\omega)z}*A_1^{\,*}(z,-\omega)e^{-i\beta(z,\omega)z}\ +\\[4pt]\dfrac{\mu_{2,2}}{2}A_2(z,\omega)e^{-i\beta(z,\omega)z}*A_2^{\,*}(z,-\omega)e^{-i\beta(z,\omega)z}*A_2(z,\omega)e^{-i\beta(z,\omega)z}\ +\\[4pt]\mu_{1,2}A_1(z,\omega)e^{-i\beta(z,\omega)z}*A_1^{\,*}(z,-\omega)e^{-i\beta(z,\omega)z}*A_2(z,\omega)e^{-i\beta(z,\omega)z}\ +\\[4pt]\mu_{2,3}A_3(z,\omega)e^{-i\beta(z,\omega)z}*A_3^{\,*}(z,-\omega)e^{-i\beta(z,\omega)z}*A_2(z,\omega)e^{-i\beta(z,\omega)z}\ +\\[4pt]\mu_{2,4}A_4(z,\omega)e^{-i\beta(z,\omega)z}*A_4^{\,*}(z,-\omega)e^{-i\beta(z,\omega)z}*A_2(z,\omega)e^{-i\beta(z,\omega)z}\end{bmatrix}$$

(E.37)

$$\frac{dA_3(z,\omega)}{dz} = -i\omega\varepsilon_0\chi_3\,e^{i\beta(z,\omega)z}\begin{bmatrix}\gamma_{Int}A_1(z,\omega)e^{-i\beta(z,\omega)z}*A_2(z,\omega)e^{-i\beta(z,\omega)z}*A_4^{\,*}(z,-\omega)e^{-i\beta(z,\omega)z}\ +\\[4pt]\dfrac{\mu_{3,3}}{2}A_3(z,\omega)e^{-i\beta(z,\omega)z}*A_3^{\,*}(z,-\omega)e^{-i\beta(z,\omega)z}*A_3(z,\omega)e^{-i\beta(z,\omega)z}\ +\\[4pt]\mu_{3,4}A_4(z,\omega)e^{-i\beta(z,\omega)z}*A_4^{\,*}(z,-\omega)e^{-i\beta(z,\omega)z}*A_3(z,\omega)e^{-i\beta(z,\omega)z}\ +\\[4pt]\mu_{1,3}A_1(z,\omega)e^{-i\beta(z,\omega)z}*A_1^{\,*}(z,-\omega)e^{-i\beta(z,\omega)z}*A_3(z,\omega)e^{-i\beta(z,\omega)z}\ +\\[4pt]\mu_{2,3}A_2(z,\omega)e^{-i\beta(z,\omega)z}*A_2^{\,*}(z,-\omega)e^{-i\beta(z,\omega)z}*A_3(z,\omega)e^{-i\beta(z,\omega)z}\end{bmatrix}$$

(E.38)

$$\frac{dA_4(z,\omega)}{dz} = -i\omega\varepsilon_0\chi_3\,e^{i\beta(z,\omega)z}\begin{bmatrix}\gamma_{Int}A_1(z,\omega)e^{-i\beta(z,\omega)z}*A_2(z,\omega)e^{-i\beta(z,\omega)z}*A_3^{*}(z,-\omega)e^{-i\beta(z,\omega)z} & + \\[2mm] \dfrac{\mu_{4,4}}{2}A_4(z,\omega)e^{-i\beta(z,\omega)z}*A_4^{*}(z,-\omega)e^{-i\beta(z,\omega)z}*A_4(z,\omega)e^{-i\beta(z,\omega)z} & + \\[2mm] \mu_{3,4}A_3(z,\omega)e^{-i\beta(z,\omega)z}*A_3^{*}(z,-\omega)e^{-i\beta(z,\omega)z}*A_4(z,\omega)e^{-i\beta(z,\omega)z} & + \\[2mm] \mu_{1,4}A_1(z,\omega)e^{-i\beta(z,\omega)z}*A_1^{*}(z,-\omega)e^{-i\beta(z,\omega)z}*A_4(z,\omega)e^{-i\beta(z,\omega)z} & + \\[2mm] \mu_{2,4}A_2(z,\omega)e^{-i\beta(z,\omega)z}*A_2^{*}(z,-\omega)e^{-i\beta(z,\omega)z}*A_4(z,\omega)e^{-i\beta(z,\omega)z} & \end{bmatrix}$$

Define

$$(E.39)\; C_\beta(z,\omega-\omega_\beta) = B_\beta(z,\omega) = A_\beta(z,\omega)e^{-i\beta(\omega,z)}$$

We continue with rewriting the equations for $B_1(z,\omega)$

$$\frac{dA_1(z,\omega)}{dz} = \frac{d\left(B_1(z,\omega)e^{+i\beta(z,\omega)z}\right)}{dz} = \frac{dB_1(z,\omega)}{dz}e^{+i\beta(z,\omega)z} + i\partial_z\left(\beta(\omega,z)z\right)B_1(z,\omega)e^{+i\beta(z,\omega)z} \Rightarrow$$

$$\frac{dA_1(z,\omega)}{dz} = \frac{dB_1(z,\omega)}{dz}e^{+i\beta(z,\omega)z} + i\beta(\omega,z)B_1(z,\omega)e^{+i\beta(z,\omega)z} + i\left(\partial_z\beta(\omega,z)\right)\left(z-z_{in}\right)B_1(z,\omega)e^{+i\beta(z,\omega)z}$$

$$\frac{dB_1(z,\omega)}{dz}e^{+i\beta(z,\omega)z} + i\beta(\omega,z)B_1(z,\omega)e^{+i\beta(z,\omega)z} + i\left(\partial_z\beta(\omega,z)\right)\left(z-z_{in}\right)B_1(z,\omega)e^{+i\beta(z,\omega)z} =$$

$$-i\omega\varepsilon_0\chi_3\,e^{i\beta(z,\omega)z}\begin{bmatrix}\gamma_{Int}B_3(z,\omega)*B_4(z,\omega)*B_2^{*}(z,-\omega)+\dfrac{\mu_{1,1}}{2}B_1(z,\omega)*B_1^{*}(z,-\omega)*B_1(z,\omega)+ \\[2mm] \mu_{1,2}B_2(z,\omega)*B_2^{*}(z,-\omega)*B_1(z,\omega)+\mu_{1,3}B_3(z,\omega)*B_3^{*}(z,-\omega)*B_1(z,\omega)+ \\[2mm] \mu_{1,4}B_4(z,\omega)*B_4^{*}(z,-\omega)*B_1(z,\omega) \end{bmatrix} \Rightarrow$$

Hence:

(E.40)

$$\frac{dB_1(z,\omega)}{dz} = -i\beta(\omega,z)B_1(z,\omega) - i\left(\partial_z\beta(\omega,z)\right)\left(z-z_{in}\right)B_1(z,\omega)$$

$$-i\omega\varepsilon_0\chi_3\,e^{i\beta(z,\omega)z}\begin{bmatrix}\gamma_{Int}B_3(z,\omega)*B_4(z,\omega)*B_2^{*}(z,-\omega)+\dfrac{\mu_{1,1}}{2}B_1(z,\omega)*B_1^{*}(z,-\omega)*B_1(z,\omega)+ \\[2mm] \mu_{1,2}B_2(z,\omega)*B_2^{*}(z,-\omega)*B_1(z,\omega)+\mu_{1,3}B_3(z,\omega)*B_3^{*}(z,-\omega)*B_1(z,\omega)+ \\[2mm] \mu_{1,4}B_4(z,\omega)*B_4^{*}(z,-\omega)*B_1(z,\omega) \end{bmatrix}$$

Using the same mechanism presented in Eq. sets (B.23) − (B.27), the equation in the time domain reads:

(E.41)

$$\frac{dC_1(z,t)}{dz} = -i\mathfrak{F}^{-1}\left(\beta(\omega+\omega_1,z)C_1(z,\omega+\omega_1) - i\left(\partial_z\beta(\omega+\omega_1,z)\right)(z-z_{in})C_1(z,\omega+\omega_1)\right)$$

$$-i\varepsilon_0\chi_3\mathfrak{F}^{-1}(\omega+\omega_1)\mathfrak{I}\left(\begin{array}{c}\gamma_{Int}C_3(z,t)C_4(z,t)C_2^*(z,t)\\\left(\mu_{1,2}|C_2(z,t)|^2 + \mu_{1,3}|C_3(z,t)|^2 + \mu_{1,4}|C_4(z,t)|^2 + \frac{\mu_{1,1}}{2}|C_1(z,t)|^2\right)C_1(z,t)\end{array}\right)$$

In the same manner we deduce:

(E.42)

$$\frac{dC_2(z,t)}{dz} = -i\mathfrak{F}^{-1}\left(\beta(\omega+\omega_2,z)C_2(z,\omega+\omega_2) - i\left(\partial_z\beta(\omega+\omega_2,z)\right)(z-z_{in})C_2(z,\omega+\omega_2)\right)$$

$$-i\varepsilon_0\chi_3\mathfrak{F}^{-1}(\omega+\omega_2)\mathfrak{I}\left(\begin{array}{c}\gamma_{Int}C_3(z,t)C_4(z,t)C_1^*(z,t)\\\left(\mu_{1,2}|C_1(z,t)|^2 + \mu_{2,3}|C_3(z,t)|^2 + \mu_{2,4}|C_4(z,t)|^2 + \frac{\mu_{2,2}}{2}|C_2(z,t)|^2\right)C_2(z,t)\end{array}\right)$$

(E.43)

$$\frac{dC_3(z,t)}{dz} = -i\mathfrak{F}^{-1}\left(\beta(\omega+\omega_3,z)C_3(z,\omega+\omega_3) - i\left(\partial_z\beta(\omega+\omega_3,z)\right)(z-z_{in})C_3(z,\omega+\omega_3)\right)$$

$$-i\varepsilon_0\chi_3\mathfrak{F}^{-1}(\omega+\omega_3)\mathfrak{I}\left(\begin{array}{c}\gamma_{Int}C_1(z,t)C_2(z,t)C_4^*(z,t)\\\left(\mu_{1,3}|C_1(z,t)|^2 + \mu_{2,3}|C_2(z,t)|^2 + \mu_{3,4}|C_4(z,t)|^2 + \frac{\mu_{3,3}}{2}|C_3(z,t)|^2\right)C_3(z,t)\end{array}\right)$$

(E.44)

$$\frac{dC_4(z,t)}{dz} = -i\mathfrak{F}^{-1}\left(\beta(\omega+\omega_4,z)C_4(z,\omega+\omega_4) - i\left(\partial_z\beta(\omega+\omega_4,z)\right)(z-z_{in})C_4(z,\omega+\omega_4)\right)$$

$$-i\varepsilon_0\chi_3\mathfrak{F}^{-1}(\omega+\omega_4)\mathfrak{I}\left(\begin{array}{c}\gamma_{Int}C_1(z,t)C_2(z,t)C_3^*(z,t)\\\left(\mu_{1,4}|C_1(z,t)|^2 + \mu_{2,4}|C_2(z,t)|^2 + \mu_{3,4}|C_3(z,t)|^2 + \frac{\mu_{4,4}}{2}|C_4(z,t)|^2\right)C_4(z,t)\end{array}\right)$$

with $\gamma_{Int} = \frac{1}{2}\iint dxdy\left(\vec{E}_3\cdot\vec{E}_4\vec{E}_2\cdot\vec{E}_1 + \vec{E}_3\cdot\vec{E}_2\vec{E}_4\cdot\vec{E}_1 + \vec{E}_4\cdot\vec{E}_2\vec{E}_3\cdot\vec{E}_1\right)$

and $\mu_{i,j} = \mu_{j,i} = \frac{1}{2}\iint dxdy\left(|\vec{E}_i|^2|\vec{E}_j|^2 + 2|\vec{E}_i\cdot\vec{E}_j|^2\right)$.

11. List of Figures

12. Bibliography

[1]   e. P. a. H. A. E. a. P. C. e. a. W. G. Franken, "Generation of optical harmonics," *Physical Review Letters,* vol. 7, p. 118, 1961.

[2]   M. a. P. V. V. a. P. R. V. Fiebig, "Second-harmonic generation as a tool for studying electronic and magnetic structures of crystals," *JOSA B,* vol. 22, pp. 96-118, 2005.

[3]   R. M. a. H. D. A. Corn, "Optical second harmonic generation as a probe of surface chemistry," *Chemical reviews,* vol. 94, pp. 107-125, 1994.

[4]   F. a. D. W. Helmchen, "Deep tissue two-photon microscopy," *Nature methods,* vol. 2, pp. 932-940, 2005.

[5]   P. J. a. L. L. M. Campagnola, "Second-harmonic imaging microscopy for visualizing biomolecular arrays in cells, tissues and organisms," *Nature biotechnology,* vol. 21, no. 11, p. 1356, 2003.

[6]   H. a. B. B. D. a. A. A. a. S. Y. Suchowski, "Broadband nonlinear frequency conversion," *Optics and Photonics News,* vol. 21, no. 10, pp. 36-41, 2010.

[7]   D. S. a. F. M. M. Hum, "Quasi-phasematching," *Comptes Rendus Physique,* vol. 8, no. 2, pp. 180-198, 2007.

[8]   T. a. N. H. Suhara, "Theoretical analysis of waveguide second-harmonic generation phase matched with uniform and chirped gratings," *IEEE Journal of Quantum Electronics,* vol. 26, no. 7, pp. 1265-1276, 1990.

[9]   M. a. G. A. a. H. D. a. C. M. a. F. M. Arbore, "Engineerable compression of ultrashort pulses by use of second-harmonic generation in chirped-period-poled lithium niobate," *Optics Letters,* vol. 22, no. 17, pp. 1341-1343, 1997.

[10] Y. L. a. N. Y.-C. a. J. C. a. Y. T. J. a. K. D.-K. a. L. J. Lee, "Broadening of the second-harmonic phase-matching bandwidth in a temperature-gradient-controlled periodically poled Ti: LiNbO 3 channel waveguide," *Optics express,* vol. 11, no. 22, pp. 2813-2819, 2003.

[11] K. a. Z. J. a. G. N. a. R. G. Regelskis, "Efficient second-harmonic generation of a broadband radiation by control of the temperature distribution along a nonlinear crystal," *Optics express,* vol. 20, no. 27, pp. 28544-28556, 2012.

[12] M. a. H. R. a. K. P. a. L. P. a. R. E. Baudrier-Raybaut, "Random quasi-phase-matching in bulk polycrystalline isotropic nonlinear materials," *Nature,* vol. 432, no. 7015, p. 374, 2004.

[13] H. a. P. G. a. A. A. Suchowski, "Adiabatic processes in frequency conversion," *Laser & Photonics Reviews,* vol. 8, no. 3, pp. 333-367, 2014.

[14] H. a. O. D. a. A. A. a. S. Y. Suchowski, "Geometrical representation of sum frequency generation and adiabatic frequency conversion," *Physical Review A,* vol. 78, no. 6, 2008.

[15] N. Baranova, "Adiabatic transition of the pump into second optical harmonic," *JETP LETTERS C/C OF PIS'MA V ZHURNAL EKSPERIMENTAL'NOI TEORETICHESKOI FIZIKI,* vol. 57, p. 790.

[16] H. a. P. V. a. O. D. a. A. A. a. S. Y. Suchowski, "Robust adiabatic sum frequency conversion," *Optics express,* vol. 17, no. 15, pp. 12731-12740, 2009.

[17] C. a. F. M. Phillips, "Efficiency and phase of optical parametric amplification in chirped quasi-phase-matched gratings," *Optics letters,* vol. 35, no. 18, pp. 3093-3095, 2010.

[18] C. a. L. C. a. C. D. a. L. Y. a. G. L. a. F. M. Phillips, "Apodization of chirped quasi-phasematching devices," *JOSA B,* vol. 30, no. 6, pp. 1551-1568, 2013.

[19] C. a. P. C. a. G. L. a. F. M. a. K. U. Heese, "Ultrabroadband, highly flexible amplifier for ultrashort midinfrared laser pulses based on aperiodically poled Mg: LiNbO 3," *Optics letters,* vol. 35, no. 14, pp. 2340-2342, 2010.

[20] C. a. P. C. a. G. L. a. F. M. a. K. U. Heese, "Role of apodization in optical parametric amplifiers based on aperiodic quasi-phasematching gratings," *Optics express,* vol. 20, no. 16, pp. 18066-18071, 2012.

[21] C. a. P. C. a. M. B. a. G. L. a. F. M. a. K. U. Heese, "75 MW few-cycle mid-infrared pulses from a collinear apodized APPLN-based OPCPA," *Optics express,* vol. 20, no. 24, pp. 26888-26894, 2012.

[22] O. a. C. L. a. C. M. a. V. F. a. M. R. Yaakobi, "Complete energy conversion by autoresonant three-wave mixing in nonuniform media," *Optics express,* vol. 21, no. 2, pp. 1623-1632, 2013.

[23] H. a. K. P. R. a. H. S.-W. a. K. F. X. a. M. J. Suchowski, "Octave-spanning coherent mid-IR generation via adiabatic difference frequency conversion," *Optics express,* vol. 21, no. 23, pp. 28892-28901, 2013.

[24] P. a. S. H. a. L. H. a. F. N. a. H. K.-H. a. K. F. X. a. M. J. Krogen, "Generation and multi-octave shaping of mid-infrared intense single-cycle pulses," *Nature Photonics,* vol. 11, no. 4, pp. 222-226, 2017.

[25] G. a. A. A. Porat, "Efficient, broadband, and robust frequency conversion by fully nonlinear adiabatic three-wave mixing," *JOSA B,* vol. 30, no. 5, pp. 1342-1351, 2013.

[26] A. a. M. G. a. P. G. a. A. A. Leshem, "Adiabatic second-harmonic generation," *Optics letters,* vol. 41, no. 6, pp. 1229-1232, 2016.

[27] P. R. Krogen, "A novel few-cycle optical source in the mid-infrared," Massachusetts Institute of Technology, 2014.

[28] R. W. Boyd, Nonlinear optics, Academic press, 2003.

[29] F. Bloch, "Nuclear induction," *Physical review,* vol. 70, no. 7-9, p. 460, 1946.

[30] R. P. a. V. J. F. L. a. H. R. W. Feynman, "Geometrical representation of the Schrodinger equation for solving maser problems," *Journal of Applied Physics,* vol. 28, no. 1, pp. 49-52, 1957.

[31] C. Y. a. H. T. a. D. P. a. S. A. a. H. J. a. H. R. a. H. T. a. P. N. a. K. T. J. Wang, "Mid-infrared optical frequency combs at 2.5 μm based on crystalline microresonators," *Nature communications,* vol. 4, p. 1345, 2013.

[32] Y. a. X. J. a. O. H. a. P. C. Ding, "Mode-selective wavelength conversion based on four-wave mixing in a multimode silicon waveguide," *Optics express,* no. 22, pp. 127-135, 2014.

[33] S. a. S. C. a. L. R. a. W. H. G. a. O. K. a. K. S. a. K. I. a. P. K. Diez, "Four-wave mixing in semiconductor optical amplifiers for frequency conversion and fast optical switching," *IEEE Journal of selected topics in Quantum Electronics,* vol. 3, no. 5, pp. 1131-1145, 1997.

[34] A. a. M. F. a. M. M. Melloni, "Four-wave mixing and wavelength conversion in coupled-resonator optical waveguides," *JOSA B,* vol. 25, no. 12, pp. C87-C97, 2008.

[35] S. a. C. A. H. L. a. L. R. a. H. J. D. a. K. J. C. a. W. W. J. a. R. P. S. J. Coen, "Supercontinuum generation by stimulated Raman scattering and parametric four-wave mixing in photonic crystal fibers," *Optical Society of America,* vol. 19, no. 4, pp. 753-764, 2002.

[36] J. M. C. a. M. S. a. W. J. a. Z. S. a. M. E. a. A. N. a. R. S. Boggio, "Optical frequency comb generated by four-wave mixing in highly nonlinear fibers," 2009.

Efficient adiabatic frequency conversions for ultrashort pulses

By

Asaf Dahan

Submitted to the department of Condensed Matter physics, School of Physics & Astronomy,

in partial fulfillment of the requirements for the degree of Master of Science in Physics

Abstract

Sensing ultrafast phenomena's demands ultrafast sources in diverse spectral regimes. Such inherently broadband source can among others be generated using frequency conversion of an ultrafast pulse. In this thesis, we developed a framework for nonlinear optical generation of ultrashort pulses through adiabatic frequency conversions evolution, incorporating both numerical evaluations and experimental validations. These include generalization of the frequency conversion process to the ultrashort regime, developing the numerical simulation for the nonlinear processes, and obtaining a robust general scheme for the design of adiabatic varying phase mismatch crystals also applicable to high-order QPM techniques. With the latter we design and investigate a novel SHG crystal with unmatched robustness under both environmental conditions and characteristics of the incoming pulse, demonstrate pulse shaping using spectral phase manipulations done before the nonlinear crystal, and obtain a design of an efficient robust optical scheme for a DFG pulse compression, with the incorporation of two photon absorption, a parasitic effect that has been lacking in all previous research on adiabatic frequency conversion, and which was found to be of great importance. Finally, we present the concept of adiabatic Four Wave Mixing frequency conversion. We present a general propagation equation for four-wave mixing derived from Maxwell's equations, capturing the full frequency and time domain nonlinear pulse propagation effects for wave-guided interactions. Last, we present that the obtained equations can be simplified to reveal the SU(2) symmetry in FWM, which leads to an analogy with rapid adiabatic passage in other two-level atomic systems.

Tel Aviv University
Raymond & Beverly Sackler
Faculty of Exact Sciences

Efficient adiabatic frequency conversions for ultrashort

pulses

In partial fulfillment to the requirements for the degree of

Master of Science at Tel Aviv University

School of Physics & Astronomy,

Department of Condensed Matter Physics

By

Asaf Dahan

March 2018

Under the supervision of Dr. Haim Suchowski